ABSTRACT

Title of Document: **CHARACTERIZATION OF RADIATION DAMAGE TO A NOVEL PHOTONIC CRYSTAL SENSOR**

Slavica Grdanovska,
Doctor of Philosophy, 2015

Co-Directed By: Professor, Robert M. Briber, Materials Science and Engineering and
Professor, Timothy W. Koeth, Institute for Research in Electronics and Applied Physics

New methods of nuclear fuel and cladding characterization must be developed and implemented to enhance the safety and reliability of nuclear power plants. One class of such advanced methods is aimed at the characterization of fuel performance by performing minimally intrusive in-core, real time measurements on nuclear fuel on the nanometer scale.

Nuclear power plants depend on instrumentation and control systems for monitoring, control and protection. Traditionally, methods for fuel characterization under irradiation are performed using a “cook and look” method. These methods are very expensive and labor-intensive since they require removal, inspection and return of irradiated samples for each measurement. Such fuel cladding inspection methods

investigate oxide layer thickness, wear, dimensional changes, ovality, nuclear fuel growth and nuclear fuel defect identification. These methods are also not suitable for all commercial nuclear power applications as they are not always available to the operator when needed. Additionally, such techniques often provide limited data and may exacerbate the phenomena being investigated.

This thesis investigates a novel, nanostructured sensor based on a photonic crystal design that is implemented in a nuclear reactor environment. The aim of this work is to produce an in-situ radiation-tolerant sensor capable of measuring the deformation of a nuclear material during nuclear reactor operations.

The sensor was fabricated on the surface of nuclear reactor materials (specifically, steel and zirconium based alloys). Charged-particle and mixed-field irradiations were both performed on a newly-developed “pelletron” beamline at Idaho State University's Research and Innovation in Science and Engineering (RISE) complex and at the University of Maryland's 250 kW Training Reactor (MUTR). The sensors were irradiated to 6 different fluences (ranging from 1 to 100 dpa), followed by intensive characterization using focused ion beam (FIB), transmission electron microscopy (TEM) and scanning electron microscopy (SEM) to investigate the physical deformation and microstructural changes between different fluence levels, to provide high-resolution information regarding the material performance. Computer modeling (SRIM/TRIM) was employed to simulate damage to the sensor as well as to provide significant information concerning the penetration depth of the ions into the material.

CHARACTERIZATION OF RADIATION DAMAGE TO A NOVEL PHOTONIC CRYSTAL SENSOR

By

Slavica Grdanovska

Dissertation submitted to the Faculty of the Graduate School of the
University of Maryland, College Park, in partial fulfillment
of the requirements for the degree of
Doctor of Philosophy
2015

Advisory Committee:

Professor Robert M. Briber, Chair

Professor Timothy W. Koeth,

Professor Eric Burgett

Professor Lourdes Salamanca-Riba

Professor Alice Mignerey, Dean's Representative

Dedication

To my mom and my uncle, Elena Adzievska and Kuzman Adzievski

Acknowledgements

The completion of this dissertation would not have been possible without the collaboration, help, hard work and patience of a number of people from the University of Maryland and Idaho State University. I would like to pay my gratitude to all of them.

First of all, I must thank my advisor, Dr. Timothy Koeth for accepting me as his student; his guidance, constant support and friendship were the key factors in achieving my goal. Thanks to all of my committee members for taking the time to read my thesis, to Vince Adams for trusting me to operate a nuclear reactor, to Radiation Safety Office for helping me ship radioactive samples and to Jason Osheroff for breaking his tools to perform precise milling of my samples.

Thank you to Team Burgett! Words cannot express my gratitude to Dr. Eric Burgett. Thank you for providing me with the opportunity to perform my experiments at your amazing facility. My special thanks go to Todd Gansauge, Scott McBeath and Austin Tam, for all those long hours spent in the pelletron and microscopy lab. Thanks to Dr. Christopher McGrath for the wise hints and for his help to make a progress in my simulations. Thank you Malwina Chaczko for tea- and walk-time, a true escape from the dark times of the RISE world.

I would like to thank my groupmates and good friends – Chanel Tissot and Travis Dietz – for reading chapters of my thesis when no one would. Chanel, thank you for being there through it all – the good, the bad, the ups and the downs.

Finally I would like to thank my family and friends for their unconditional love, understanding and support. I could not have completed this work without their constant encouragement to achieve and the huge sacrifices that they made.

Table of Contents

List of Tables

List of Figures

List of Abbreviations

AGR	Advanced Gas Reactor
AISI	American Iron and Steel Institute
ASTM	American Society for Testing and Materials
ATR	Advanced Test Reactor
BCA	Binary Collisions Approximation
BCC	Body-Centered Cubic
BWR	Boiling Water Reactor
CCD	Charge-Coupled Device
DGNAA	Delayed Gamma-ray Neutron Activation Analysis
DOE	Department of Energy
EBSD	Electron Backscatter Diffraction
ESEM	Environmental Scanning Electron Microscope
FBG	Fiber Bragg Grating
FC	Faraday cup
FCC	Face-Centered Cubic
FDTD	Finite Difference Time Domain
FEG	Field Emission Gun
FFT	Fast Fourier transform
FIB	Focused Ion Beam
FRAPTRAN	Fuel Rod Analysis Program Transient
HCP	Hexagonal Close Packed
HFIR	High Flux Isotope Reactor
HPGe	High Purity Germanium Detector
HTGR	High Temperature Gas Reactor
I&C	Instrumentation and Control
INL	Idaho National Laboratory
ISU	Idaho State University
LIBS	Laser-Induced Breakdown Spectroscopy

LMFBR	Liquid Metal Fast Breeder Reactor
LMIS	Liquid Metal Ion Source
LWR	Light Water Reactor
MIT	Massachusetts Institute of Technology
MPB	MIT Photonic-Bands
MUTR	Maryland University Training Reactor
NAA	Neutron Activation Analysis
NEC	National Electrostatic Corp.
NRC	Nuclear Regulatory Commission
ORNL	Oak Ridge National Laboratory
PGNAA	Prompt Gamma-ray Neutron Activation Analysis
PHWR	Pressurized Heavy Water Reactor
PNNL	Pacific Northwest National Laboratory
PWR	Pressurized Water Reactor
RISE	Research and Innovation in Science and Engineering
SADP	Selected Area Diffraction Pattern
SEM/EDS	Scanning Electron Microscopy with Energy-Dispersive X-ray Spectroscopy
SRIM	Stopping and Range of Ions in Matter
TEM	Transmission Electron Microscopy
TRIGA	Training, Research, Isotopes, General Atomic
TRIM	Transport of Ions in Matter
UMD	University of Maryland

1 Introduction

1.1 Current Reactor Materials Characterization and Monitoring Technologies

Maintaining integrity of the fuel rods and fuel assemblies in a nuclear reactor plays a very important role in the nuclear industry, preventing release of radioactive materials from the fuel to the coolant. This can be achieved with core structural materials that retain their mechanical properties and integrity. Significant necessities for in-core materials utilized as a part of nuclear reactors are as follows:

- The material must exhibit dimensional consistency under irradiation, whether under stress (irradiation creep or relaxation) or without stress (swelling).
- The mechanical properties of every single auxiliary material (rigidity, malleability, creep resistance, crack strength, flexibility) must remain satisfactory after ageing.
- The materials must maintain their properties in corrosive environments (reactor coolant).

Recently, new and improved radiation resistant materials have been developed to support higher burnups, withstand harsher irradiation environments and higher temperatures. Throughout this development, when selecting structural materials for a reactor core, radiation resistance is the most important consideration. In conjunction, fuel cladding material is the most critical when it comes to fuel integrity and longevity since this component is exposed to extreme temperatures, pressures and neutron and gamma dose rates.

The instrumentation and control (I&C) systems of a nuclear reactor play a vital role in safe and efficient plant operation. They are implemented in the design and construction of nuclear power plants to provide pertinent systems information during both normal and accident scenarios. The instrumentation and control systems are fundamentally an extra pair of eyes and ears for the operator. In many cases they provide automatic control of the plant and its auxiliary systems, which, in conjunction with a reactor operator's monitoring, leads to safer and more efficient operation. I&C systems can also protect the plant from operator errors through the use of interlocks and scram channels. In short, the main purpose of I&C systems is to preserve the integrity of safety barriers under normal, transient and accident conditions.

The operational limits of a nuclear reactor are established through safety-related parameters such as the operational temperature ranges of fuel and cladding, the void reactivity effect and reactivity margins, to ensure that the reactor is safely operated at all times. This control and monitoring equipment utilizes various detectors and sensors that provide protection against unacceptable excursions beyond safe conditions in the reactor and its auxiliary systems.

Within the general area of developing instrumentation that will enhance the safety and reliability of nuclear power plants, new methods of nuclear fuel and cladding characterization must be developed and implemented. One such class of new methods is aimed at the characterization of fuel performance by performing in-situ, real time measurements on nuclear fuel on the nanometer scale. Nuclear power plants depend on instrumentation and control systems for monitoring, control and protection. Traditionally, methods for fuel characterization under irradiation are performed using a "cook and look"

method. These methods require the removal, inspection and return of irradiated samples for each measurement which makes them very expensive, labor-intensive and possibly a radiation safety hazard. Such fuel cladding inspection methods investigate oxide layer thickness, wear, dimensional changes, nuclear fuel growth and nuclear fuel defect identification. These methods are not suitable for all commercial nuclear power applications as they are not always available to the operator when needed. Additionally, such techniques often provide limited data and may exacerbate the phenomena being investigated.

Emphasis in current research and development has been placed on discovering how to stabilize displaced atoms, vacancies, and lattice distortions. This is the key to improving radiation resistance in materials. For instance, introducing new grain boundaries can capture migrating radiation defects or vacancy sinks in a material.

A metric of the effect of radiation dose on a material is the number of times an atom is displaced from its normal lattice site by atomic collision processes. This is quantified as displacements per atom (dpa) [1], [2]. Fuel cladding materials and their behavior under irradiation has been studied for more than 50 years, where core structural materials are subject to temperatures up to 400°C and damages up to 20 dpa [3]. In a typical light water reactor (LWR) fuel cladding, at a burnup of 30 GWd/tU (gigawatt-days per metric ton of Uranium), each atom is displaced from its site in the crystal lattice an average of 20 times (or 20 dpa) [4]. The dpa is roughly proportional to the burnup level, where for instance in the same reactor, 60 GWd/tU would correspond to 40 dpa [5].

1.2 Methods to Enhance Monitoring of Radiation Damage in Materials

In 2011, the Office of Nuclear Energy in the Department of Energy (DOE-NE) put forth a new proposal in fuel research and development (R&D) that highlights an approach that relies on first principle models to develop enhanced fuel designs that offer substantial improvements over current fuels [6]. This approach was initiated through a research program aimed at developing I&C systems composed of novel sensors that are capable of measuring high fidelity, real-time data that is crucial for characterizing the performance of new fuels during irradiation. These sensors are designed to have unprecedented accuracy and resolution for obtaining the data needed to characterize three-dimensional changes in fuel microstructure during irradiation. These new in-situ technologies (referred to as "in-pile" or "in-core") were primarily introduced for test irradiations at the Advanced Test Reactor (ATR) at the Idaho National Laboratory (INL) and the High Flux Isotope Reactor (HFIR) at the Oak Ridge National Laboratory (ORNL) [7], [8]. Table 1-1 (Page 5) shows a list of in-pile test sensors available at ATR and HFIR that can provide real-time sensor data during irradiation [7].

Currently, there are various, tested candidate technologies that could increase the reliability of data obtained throughout irradiation of core materials/components such as nuclear fuel and cladding materials. Such technologies described in [7], include fiber optic sensors, ultrasonic transducers, laser ultrasound, borescope, laser-induced breakdown spectroscopy (LIBS) and electrical conductivity measurements. These are instrumentation techniques initially identified by the INL researchers that could be improved to allow for in-core, real-time measurements of radiation effects on materials

and other key parameters. A comparison of the candidate technologies with their advantages and limitations is presented in Table 1-2 (Page 6) [7].

Table 1-1: Summary of various in-pile test sensors deployed at or currently being investigated for use in ATR and HFIR [2].

Parameter	Sensor	Operating Conditions	Accuracy
Temperature	Melt Wires	100-1200 ˚C	2-3 ˚C
	SiC monitors	100-800 ˚C	2%
	Thermocouples (N, K)	100-1000 ˚C	2%
	Thermocouples (HTIR-TCs)	100-1800 ˚C	2%
	Thermocouples (C, D, R, and S)	100-2000 ˚C	2%
	Ultrasonic Thermometers	1300-3000 ˚C	2%
Thermal Conductivity	Multiple Thermocouple	100-3000 ˚C, depending on thermocouple type	2-8%
	Hot Wire Needle Probe	100-3000 ˚C, depending on materials selected	2%
Density/Geometry Changes	Length - LVDT	up to 500 ˚C	1-10 µm
	Diameter - Diameter Gauge	up to 500 ˚C	1-10 µm
Crack Initiation/Growth	DCPD Method	350 ˚C	~20 %
Young's Modulus	Loaded Creep Specimen	up to 500 ˚C	~10 %
Fission Gas/Pressure	Sampling	Numerous isotopes	unknown
	Pressure Gauge	220-1020 psi	2.9-7.3 psi
Thermal Flux	Flux Wires/Foils	Material dependent	~10 %
	SPNDs	Dependent on emitter	~1-10 %
	Fission Chambers	Dependent on fissile deposit	~1-10 %
Fast Flux	Flux Wires/Foils	Material dependent	~1-10 %
	Fission Chambers	Dependent on fissile deposit	~1-10 %

Table 1-2: Candidate Instrumentation Technologies Comparison [2].

<table>
<tr><th>Technology</th><th>Possible Parameter</th><th>Test Conditions</th><th>Advantages</th><th>Disadvantages</th></tr>
<tr><td rowspan="6">Fiber Optics</td><td>Temperature</td><td rowspan="6">Inert Gas (possibly liquid metal for some application with appropriate coatings)</td><td rowspan="5">Small diameter, non-contact, distributed sensor</td><td rowspan="2">Fiber darkening may affect accuracy and longevity</td></tr>
<tr><td>Pressure</td></tr>
<tr><td>Strain</td><td rowspan="4">Indirect measurement based on fiber properties</td></tr>
<tr><td>Elastic Properties</td></tr>
<tr><td>Crack Initiation/Growth</td></tr>
<tr><td>Thermal Conductivity</td><td colspan="2">unknown</td></tr>
<tr><td rowspan="8">Ultrasonics</td><td rowspan="2">Temperature</td><td rowspan="8">Inert Gas and Liquid Metal</td><td rowspan="2">Small diameter, distributed sensor</td><td>Demonstrated up to 3000 ˚C</td></tr>
<tr><td>Accuracy dependent on sample material</td></tr>
<tr><td>Length</td><td rowspan="7">Non-intrusive sensor</td><td rowspan="7">Higher accuracy possible with magnetostrictive or piezoelectric transducers</td></tr>
<tr><td>Diameter</td></tr>
<tr><td>Crack Initiation/Growth</td></tr>
<tr><td>Young's Modulus</td></tr>
<tr><td>Porosity</td></tr>
<tr><td>Grain Size</td></tr>
<tr><td rowspan="2">Laser Ultrasound</td><td>Porosity</td><td rowspan="7">Inert Gas</td><td rowspan="2">Non-contact sensor</td><td rowspan="4">Fiber darkening may affect accuracy and longevity</td></tr>
<tr><td>Mechanical Properties</td></tr>
<tr><td rowspan="2">Borescope</td><td>Crack Initiation/Growth</td><td rowspan="2">Small diameter, non-contact with visual image</td></tr>
<tr><td>Porosity</td></tr>
<tr><td rowspan="2">Laser-induced Breakdown Spectroscopy</td><td>Elemental Composition</td><td rowspan="2">Non-contact sensor</td><td rowspan="2">Fiber darkening may affect signal/noise ratio</td></tr>
<tr><td>Microstructural Changes</td></tr>
<tr><td rowspan="2">Electrical Conductivity</td><td>Crack Initiation/Growth</td><td rowspan="2">Non-intrusive sensor</td><td rowspan="2">Tests needed to quantify validity</td></tr>
<tr><td>Porosity</td></tr>
</table>

Recently, several research institutes affiliated with nuclear materials laboratories and test reactors have increased efforts to provide new in-pile sensors to support irradiation testing of core materials [1], [7], [6], [8]. These institutes have made significant progress in developing simulation codes to help understand the performance of nuclear fuel, however; none have developed sensor technologies that could yield the data required to allow real-time observation of changes in fuel microstructure and properties during irradiation [9].

As an example, the U.S. Nuclear Regulatory Commission (NRC) uses codes to evaluate nuclear fuel behavior under various reactor-operating conditions. FRAPTRAN (Fuel Rod Analysis Program Transient) is a nuclear fuel performance code developed by the Pacific Northwest National Laboratory (PNNL) for calculating transient fuel behavior at high burnup (up to 62 GWd/tU) [10]. The code consists of several models that are able to perform various calculations which are based on finite difference techniques (Table 1-3).

Table 1-3: Various calculation models included in the Fuel Rod Analysis Program Transient (FRAPTRAN) code and their capabilities in relation to important nuclear parameters.

FRAPTRAN Code Model	Calculations and Capabilities
Heat Conduction	Heat transfer calculation from the fuel to the cladding and the cladding to the coolant.
Oxidation	Calculation of degree of cladding embrittlement and the amount of heat generation by cladding oxidation.
Mechanical Response	Calculation of the stress caused by the mechanical interaction of the fuel and cladding and by fission gas pressure inside the fuel rod.

Despite the fact that various simulation codes exist to support the assessment of nuclear fuel behavior, there is currently no physical test to benchmark the results of the code with actual fuel conditions. For this reason, none of the facilities have been able to create a monitoring technique that could be implemented in the commercial nuclear fleet.

1.3 Objective (Thesis Statement)

This thesis investigates a novel nanostructured sensor based on a photonic crystal design that is implemented in a nuclear reactor environment. The goal is to produce an in-situ radiation-tolerant sensor capable of measuring the deformation of a nuclear material during nuclear reactor operations.

The sensor was fabricated on the surface of multiple nuclear reactor materials (specifically, steel and zirconium based alloys), tested using a charged particle accelerator and characterized with focused ion beam (FIB), transmission electron microscopy (TEM), and scanning electron microscopy with energy-dispersive X-ray spectroscopy (SEM/EDS) to provide highly precise information regarding the material performance. The accelerated testing shows that the sensor can be used in nuclear reactors to provide real-time measurements of changes throughout irradiation. The use of a charged particle accelerator as a tool for implementing irradiation damage has demonstrated very promising results because of the prompt damage rates and absence of induced radioactivity. The results of this work show that the nanostructured sensors remain physically intact even after delivering a total fluence that can be compared to the total fluence received in commercial power plant accident scenarios. This demonstrates that, in the future, such nanostructured sensors can be used as a part of a monitoring

system, together with an optical system, to precisely measure real-time, in-core fuel behavior. Ultimately, this type of monitoring system can provide measurements with exceptional accuracy (nanometer scale) and can provide an alternative to the use of the conventional and more obtrusive "cook and look" methods.

1.4 Dissertation Outline

This thesis will begin with an overview of nuclear fuel and cladding since they are the critical components of a nuclear reactor, as well as the materials of interest in this work. The fundamentals of radiation damage and radiation effects and the description of a nuclear reactor environment will then be discussed in order to prepare the reader for the fuel and cladding behavior and changes throughout irradiation. This will include a description of the fundamentals of the interaction of ionizing radiation with matter and the basic effects of radiation damage, such as point defects, dislocations and grain boundaries.

The next portion of this thesis (Chapter 3 and Chapter 4) will provide an introduction to photonic crystals and photonic theory, followed by a description of the photonic crystal sensors (*LightGauge* sensors) utilized in this work and their substrate materials.

Chapter 5 is composed of the description of the facilities and equipment used to induce damage in the *LightGauge* sensors, the experimental design and setup and the optimization of the experimental conditions. Emphasis is placed on characterization of the samples post-irradiation and analysis of the experimental results, including the results

of irradiation-induced swelling, grain size change and interplanar spacing change – all due to radiation defects. Finally, in Chapter 6, the observations obtained through characterization with FIB, SEM and TEM will be presented.

2 Background

2.1 Nuclear Fuel and Cladding

The most essential component of a nuclear reactor is its fuel. Nuclear fuels for conventional light water reactors are composed of fissile isotopes. The composition of these fuels typically includes fissile material (both fresh ^{235}U, and ^{239}Pu created from neutron capture on ^{238}U) that accounts both for the criticality of the reactor and the fission products that are the result of the release of fission energy (i.e. powering the reactor). This fissile material is located inside the cladding[*]; typically in the form of fuel "pellets" stacked one on top of another throughout the height of the cladding. When fissioned, these heavy isotopes produce fission fragments as well as the prompt and delayed neutrons that sustain the nuclear chain reaction [11]–[13]. The nuclear chain reaction consists of series of fissions (splitting of atomic nuclei), each instigated by a neutron produced in a preceding fission. For instance, an average of 2.5 neutrons are released by the fission of each ^{235}U nucleus that absorbs a low-energy neutron. Fuel performance is determined by the behavior of the fuel over long periods of operation and is heavily influenced by the effects of radiation-induced damage. This damage involves physical and chemical processes that occur in fuel materials during reactor operation. These processes are discussed in detail in section 2.3.

[*] Cladding is the most outer layer of the fuel rods; a barrier between the coolant and the fuel [11].

Over time, nuclear engineers have developed many different designs of a nuclear reactor. For example, current reactors have been constructed with solid fuels and liquid fuels, thick reflectors and no reflectors, forced cooling circuits and natural convection heat-removal systems, and so on. Table 2-1 summarizes the basic components for common reactor types such as fuel, cladding, moderator and coolant materials [11], [14]. In the case of conventional reactors, pressurized water reactor (PWR) boiling water reactor (BWR), the most common fuel material is uranium dioxide (UO_2) and the most common cladding material is Zircaloy (a zirconium alloy containing trace amounts of iron, tin and chromium).

Table 2-1: Comparison of basic reactor characteristics between different types of reactors.

Reactor Characteristic				
Reactor Type	**Fuel**	**Cladding**	**Coolant**	**Moderator**
PWR (Pressurized Water Reactor)	UO_2	Zircaloy-4	H_2O	H_2O
BWR (Boiling Water Reactor)	UO_2	Zircaloy-2	H_2O	H_2O
PHWR (Pressurized Heavy Water Reactor)	UO_2	Zircaloy-4	D_2O	D_2O
HTGR (High Temperature Gas Reactor)	UC	Graphite	Helium	Graphite
AGR (Advanced Gas Reactor)	UO_2	Stainless Steel	Carbon Dioxide	Graphite
LMFBR (Fast Breeder Reactor)	PuO_2/ UO_2	Stainless Steel	Liquid Sodium	-

Table 2-1 demonstrates that there are different types of fuel and cladding used in different reactors. Typically, metals and alloys (uranium, plutonium and thorium)

combined with ceramics (oxides and carbides) have been utilized in reactor cores. Frequently considered an ideal fuel is uranium carbide (UC), utilized in high temperature gas reactors, due to its absence of phase change until its melting point (2350 °C [15]), excellent irradiation stability and thermal conductivity, yet its high fabrication cost and high swelling rate limit its use in reactors [16]. Plutonium dioxide (PuO_2) is type of fuel used in many mixed oxide and fast reactors. Its advantages include allowing reactors to operate at a reduced uranium enrichment due to the high fission cross section of PuO_2 [17].

Uranium dioxide (UO_2), however, is by far the most commonly used fuel material in the nuclear industry today due to its use in the two most abundant reactor designs, the PWR and BWR. The properties of uranium dioxide are exploited and controlled through a careful pressing and sintering process. Despite its low thermal conductivity, the resulting ceramic UO_2 fuel is highly effective at containing fission products and minimizing cracking, is chemically compatible with the cladding, has high neutron utilization, a high melting point, an exceptional radiation stability and a high corrosion resistance in water [18].

The complex fabrication process that creates uranium dioxide powder includes mining and milling of uranium to produce “yellowcake”, (triuranium octoxide, U_3O_8), followed by refining and conversion of yellowcake to uranium hexafluoride (UF_6), and enrichment of uranium hexafluoride to increase the concentration of ^{235}U and finally the processing of uranium hexafluoride to produce powdered UO_2.

Before the powdered UO_2 can be utilized in a nuclear reactor, it must first be fabricated into cylindrical fuel "pellets" approximately 1 cm in length and 0.8 cm in diameter. Weighing only 10 grams, each pellet contains as much energy as a metric ton of coal [19]. For conventional light water reactors, UO_2 powder is ground and then compressed during heating at 1600 ˚C [20] to sinter the powder into hundreds of thousands of identical, cylindrical fuel pellets. Each pellet features a concave "dimple" region at the top and bottom to allow for vertical swelling of the fuel pellet during irradiation (Figure 2-1). The pellets are sintered in a high-temperature furnace to increase the density of the pellets and to eliminate the presence of interstitial oxygen. Excess oxygen causes corrosion and causes the UO_2 material to become sub-stoichiometric. The ceramic nature of the pellets enables them to withstand very high temperatures (up to 1400 ˚C [21]) while maintaining their shape. Ultimately, the ceramic fuel pellet is the first barrier against the release of fission gases.

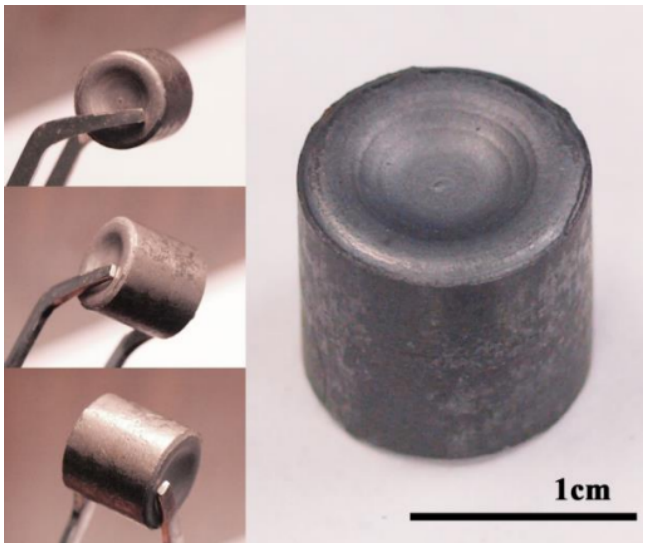

Figure 2-1: Near-net-shape UO_2 fuel pellet; representation of the concave "dimple" region [22].

The fuel pellets must be first contained in cladding to be used as a nuclear fuel. Cladding is the outermost layer of a nuclear fuel rod that serves as a barrier between the fuel and the reactor coolant [11], [23]. The most common cladding materials are zirconium alloys, stainless steel, silicon carbide and aluminum [24].

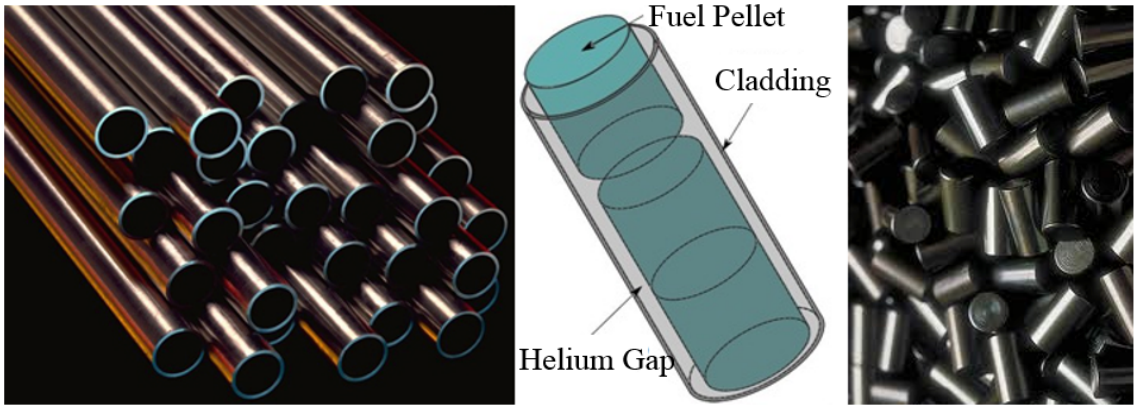

Figure 2-2: Zircaloy cladding tubes (right), simplified schematic of a fuel element, comprised of three components: fuel pellets, enclosed in a protective cladding, separated by a small gap that is filled with helium gas (middle) and completed UO_2 fuel pellets (left) [25], [26].

The left photo in Figure 2-2 shows Zircaloy cladding tubes [25]. The primary function of the cladding is to contain the fuel and the fission products. In most reactors the cladding consists of a cylindrical tube that is capped on both ends. The cladding does not come into contact with the fuel pellets; rather, the pellets are stacked and held in compression by springs at the top and bottom of the cladding. The space around the springs, and between the fuel pellet stack and the cladding, is filled with pressurized helium gas; the schematic in Figure 2-2 (middle) shows the main three components of a fuel element.

The cladding is vital to the safety and performance of the nuclear reactor and serves the following purposes:

- To isolate the UO_2 pellets from the core environment
- To transfer heat from the UO_2 pellets to the reactor coolant (for the purposes of power generation and to protect the pellet from overheating)
- To contain fission gases and other irradiation products produced by the fuel
- To act as the first barrier towards spread of radioactivity to the environment

The composition, size and shape of the fuel cladding are dependent upon the needs of the reactor. Characteristics of an ideal cladding include:

- Favorable mechanical properties: high ductility, hardness and tensile strength
- Desirable physical properties: high corrosion resistance [11], high melting temperature (to withstand accident conditions) and high thermal conductivity (to minimize thermal stresses arising from temperature differences) [27]
- Satisfactory nuclear properties: low absorption cross-section[†] of thermal neutrons (to prevent the absorption of fission and thermalized neutrons by the cladding)

Throughout reactor transients and accidents, the cladding may experience deterioration caused by a temperature increase, oxidation embrittlement [29], [30], or mechanical interaction with the fuel caused by stress [31]–[35]. These events may lead to

---

[†] Cross-section is the probability that a certain nuclear reaction will take place in an effective size of the nucleus for that reaction. For example, the absorption thermal cross-section, the probability that a neutron will be absorbed by the nucleus, of zirconium is 0.18 b [28].

cracking or rupture of the cladding, causing the release of fission products into the coolant. Such events have been observed at the Three Mile Island [36] and Fukushima accidents [37].

The completed structure (Figure 2-2, middle, Page 14), composed of the fuel pellets and the cladding, is called a "fuel element". Conventional light water reactors typically possess thousands of fuel elements, arranged into assemblies. For example, the core of a Westinghouse PWR may have over 50,000 fuel elements [38].

2.2 Reactor Environment

The environment of the core of a light water reactor is a combination of high temperatures, high neutron and gamma fluxes, mechanical stresses and chemical reactions. All of these factors combined can induce changes in the microstructure of the fuel and cladding that are very difficult to predict in a systematic fashion [30], [39]. These changes in microstructure lead to a decrease in mechanical performance of the fuel and cladding which can lead to a decrease in the safety of the reactor.

When considering the impact of these conditions on the integrity of the fuel and cladding, perhaps the most significant consideration of the reactor environment should be placed on the flux of neutrons and gamma rays [40]. The neutron flux in a reactor varies both in the spectral distribution of its energy as well as in the ratios of fast and thermal neutrons. The gamma flux also depends on the energy spectrum of the core but to a smaller degree than the neutron flux. The gamma flux has a greater dependence on the fission rate and the burnup, i.e. the number of fission fragments present. The spectral

intensity of the neutron-gamma fluxes are correlated with the type of reactor, location in that reactor, and also the amount and type of shielding if applied. Studies of irradiated fuel and cladding have attributed changes in the microstructure as well as decreases in tensile strength and ductility, increases in corrosion rates to in-core neutron and gamma irradiation [41]–[43].

2.3 Radiation Damage and Radiation Effects

It is well known that irradiation with neutrons and heavy charged particles (alpha particles, protons, fission products etc.) produces significant damage on materials [15], [44]–[47]. Various experimental studies on irradiation-induced effects have been performed such as, comparison of tensile behavior of different types of steel, reported in [48], misorientation of grain boundary in stainless steel [49], microstructure and microchemistry of stainless steel [50], properties of zirconium alloys [51], comparison of radiation damage in silicon, [52] etc.

Radiation-induced damage in reactor materials is typically quantified by reporting the displacement per atom (dpa) observed in the irradiated material. Dpa is a calculated measure of radiation damage that reflects not only the dose and the type of irradiation but also includes some measure of the material response to the irradiation. Since lattice atoms have a very small binding energy of about 10 to 60 eV [15], they can easily get be displaced from their lattice position by an impacting particle. The atoms that are knocked off by an incoming high-energy particle are called “primary knock-on atoms (pka)” or “knock-ons”. With a large number of knock-ons and movements from original lattice positions, a large number of displacements occur in the lattice.

Dpa is not an exact measurement for the lattice defects because usually the primary atom that received the kinetic energy through its interaction with the high-energy particle imparts energy to the neighboring atoms as well, producing a cascade of collisions where a lot of cascaded defects get recovered. For typical nuclear reactor applications, the actual damage in the irradiated materials correlates with the dpa.

2.3.1 Interaction of Ionizing Radiation with Matter

Radiation damage results when the interaction between radiation and a material causes an unwanted change to the structure or properties of that material. Different types of radiation and their mechanisms of interaction with matter, as well as the understanding of the properties of the materials, help in comprehending the impacts of radiation. Radiation effects on materials, with an emphasis of ionizing radiation effects, are briefly discussed in this section.

When radiation with sufficient energy interacts with matter, it can remove a tightly bound electron from an atom, which results in an ionized or charged atom; this type of radiation is defined as ionizing radiation [53]. There are different types of ionizing radiation such as:

- Charged particle radiation, which includes alpha particles, protons, electrons and ions.
- Electromagnetic radiation such as the higher frequency ultraviolet radiation, x-rays and gamma rays
- Neutral radiation, such as neutrons

The interaction of charged particles (alpha, beta and protons) with matter is different from that of the neutral radiations (neutrons and gamma). Charged particles ionize atoms through interaction with the electrons of their atoms and are classified as directly ionizing whereas gamma rays and neutrons can produce a charged particle that can then ionize other atoms within the material (Figure 2-3) and are classified as indirectly ionizing. This distinction is important because the strength of the interaction limits the penetrability of charged particles, which limits damage to the material surface, while photons and neutrons are able to penetrate deeper and cause a more uniform effect. For instance, at an energy of 1 MeV, the range in air is on the order of 10^4 cm for photons, 10^2 cm for neutrons and electrons and 10^0 for protons. [54], [55].

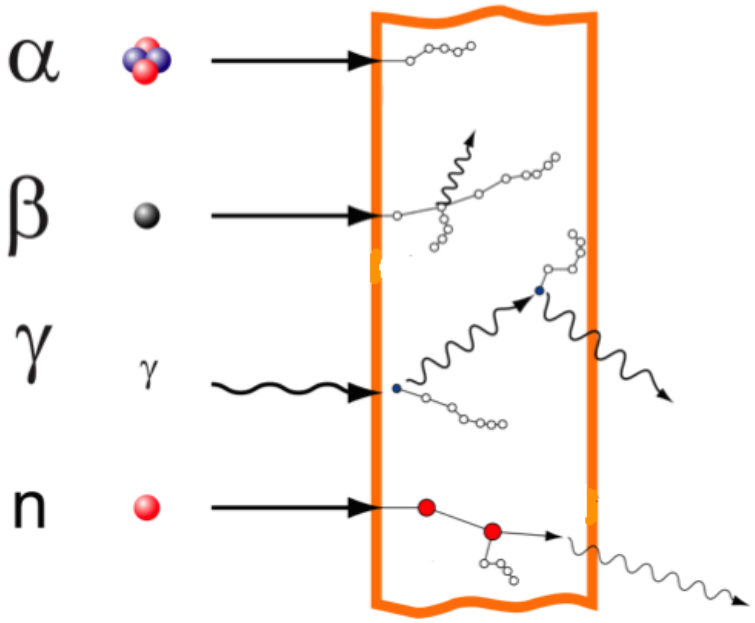

Figure 2-3: Types of ionizing radiation and their interaction with matter; the paths of particles such as those of alphas, betas (electrons), and neutrons are represented by straight lines while wavy lines represent gamma rays. The unfilled circles represent where the ionization occurs. [56]

2.3.1.1 Heavy Charged Particles

Heavy charged particles are defined "heavy" because of their mass is hundreds of times greater than that of the electron. They can be both positively and negatively charged particles, which excite the electrons of target nuclei and with each excitation, lose a small fraction of their energy. They travel in quite straight paths except at the very end of their travel when they have lost practically all their kinetic energy as a result of large number of collisions; as the distance traveled increases, the energy of the ions decreases. The collision of heavy charged particles with bound electrons is inelastic, where a fraction of the kinetic energy is lost [57], [58], to overcome the binding energy of the target electron. An example of a collision of a heavy charged particle with a bound electron is illustrated in Figure 2-4, in which the fraction of kinetic energy lost in each collision can be represented as (Equation 2-1):

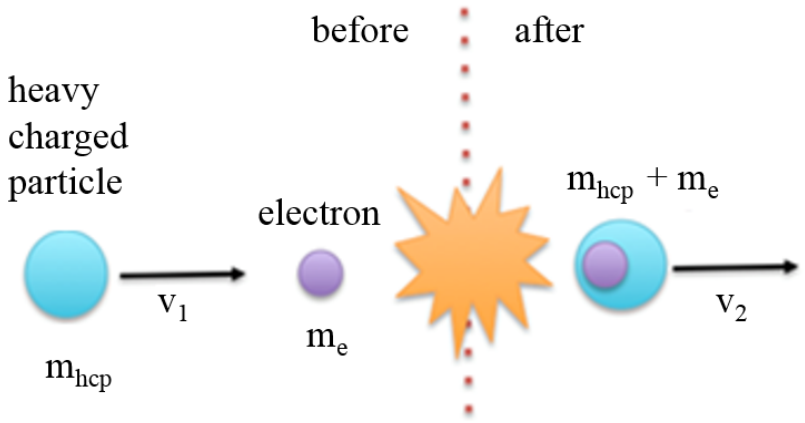

Figure 2-4: Representation of a single collision energy loss when heavy charged particle interacts with a bound electron.

Equation 2-1

$$\frac{\left(KE_i - KE_f\right)}{KE_i} = \frac{m_e}{m_{hcp} - m_e}$$

Where:

KE_i initial kinetic energy
KE_f final kinetic energy
m_{hcp} mass of the heavy charged particle
m_e mass of the electron

The energy loss of the charged particles as a function of penetration depth is represented by the Bragg curve. A typical Bragg curve for protons is depicted in Figure 2-5. The peak in relative stopping power that occurs right before the particle comes to a rest is called the Bragg Peak. As the particle loses kinetic energy, the cross section for interaction increases. This means that there is an increase in particle interaction that results in an increased stopping power before the particle comes to rest. This is of high importance since the specific depth where the proton will deposit most of its energy is where the most damage to the material will occur. The relative stopping power behavior as described by the Bragg curve is very useful in particle therapy for cancer treatment, allowing doctors concentrate the stopping power, and therefore the energy deposition of the particle, at the cancer cells while minimizing damage to the surrounding cells [59], [60].

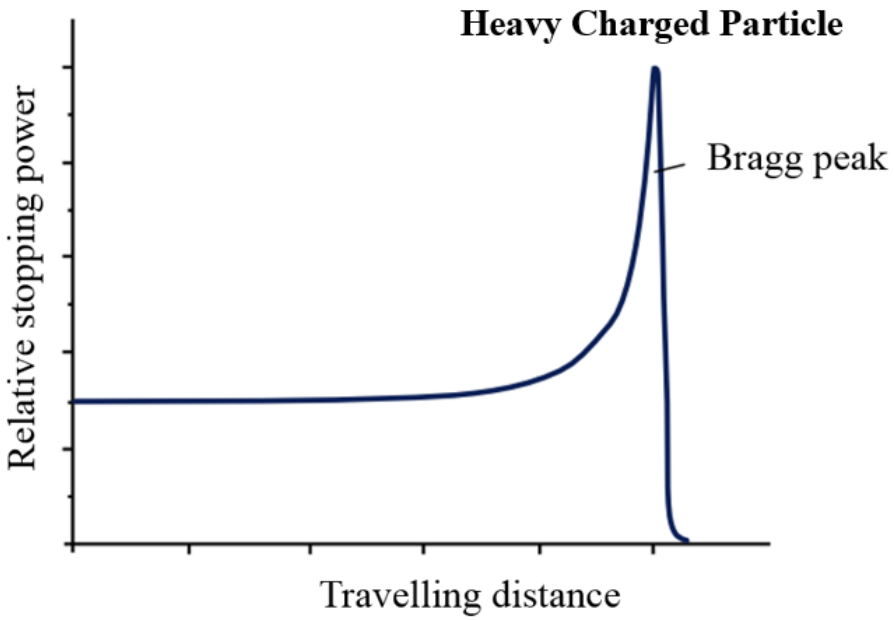

Figure 2-5: Bragg curve for protons in relative stopping power; the plot shows the sharp deposition of energy known as the Bragg peak.

2.3.1.2 Light Charged Particles

Light charged particles, such as beta particles or electrons, lose energy while travelling through matter in a manner similar to heavy charged particles, primarily interacting with matter through the Coulomb force. The difference in the mass of light and heavy charged particles however makes a difference in the energy losses between the two types. Light charged particles, specifically electrons, experience Bremsstrahlung radiation (German: “braking radiation”), which is an electromagnetic radiation emitted by a charged particle deceleration when passing through matter in electric fields of atomic

nuclei; and elastic scattering interactions, associated with the travelling path of the particle being deflected [53], [61], [62].

2.3.1.3 Neutral Radiations

Neutral radiations such as neutrons and photons are indirectly ionizing, as they do not carry any charge. Neutron radiation consists of free neutrons, such as those emitted from nuclear fission while gamma radiation is a type of electromagnetic radiation consisting of a high-energy photon that is emitted from an unstable nucleus (unlike x-ray radiation which originates from transitions of atomic electrons) [11], [61]. For the purposes of this dissertation, the only ionizing photons that will be considered are gamma rays.

A high-energy photon may interact with matter through one of three mechanisms: the photoelectric effect, pair production and Compton scatter. The probability of each of the mechanisms is dependent upon the energy of the radiation and the atomic number of the target nucleus.

a. *The photoelectric effect* predominates when a low energy gamma ray ($E < 0.3$ MeV [63]) interacts with an orbital electron of an atom. The kinetic energy of the photon is sufficient to remove an electron from its orbital shell, sending the atom into an excited state. The formation of this excited state is always followed as by a secondary emission since the atom cannot stay in an excited state indefinitely [62]. The photon interaction with an orbital electron is illustrated in Figure 2-6.

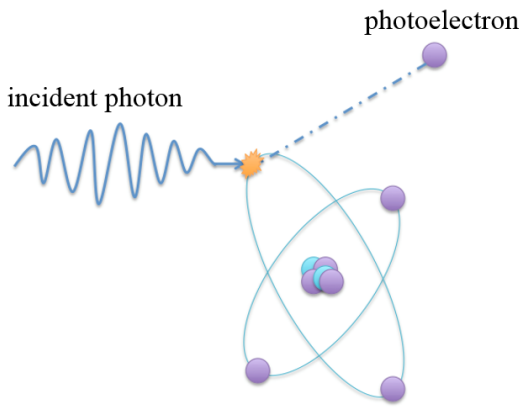

Figure 2-6: Gamma interaction by photoelectric effect.

b. *Compton scattering* is the interaction between a gamma ray of intermediate energy (0.3 MeV < E < 1.5 MeV [63]) and an individual electron of the target nucleus (the binding energy between the electron and its atom is much smaller than the energy of the gamma ray) [11]. Contrasting the photoelectric effect, in this process the gamma ray preserves a portion of its original energy and transfers at least enough to eject the electron from its orbit while the rest of it is deflected at an angle (incoherent scattering) [64]. The Compton scattering is illustrated in Figure 2-7.

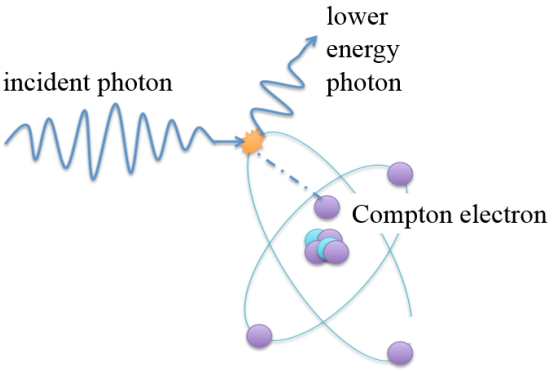

Figure 2-7: Gamma interaction by Compton scattering.

c. *Pair production* occurs when a photon with an energy of at least 1.022 MeV [63] is absorbed in a high-Z material, resulting in the formation of an electron-positron pair. The 1.022 MeV energy is equivalent to the rest mass of the electron and positron. The pair is very short-lived leading to conversion of these two particles into two gamma photons with energy of 0.511 MeV each. A schematic of pair production can be depicted in Figure 2-8.

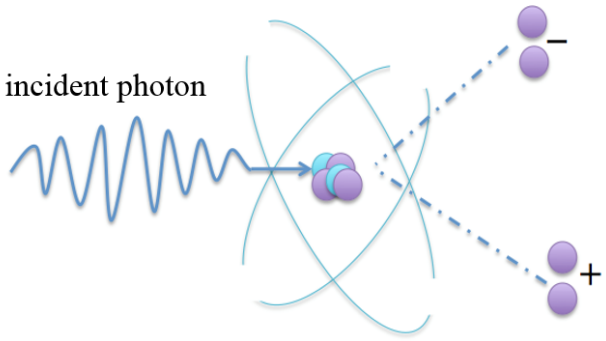

Figure 2-8: Gamma interaction by pair production.

In contrast to electrons, gammas and heavy charged particles, neutrons interact weakly with matter, not interacting through the Coulomb force and therefore only interacting with atomic nuclei [11]. Depending on their origin and distance of travel, neutrons can have energies ranging from less than an electron volt (eV)[‡] to several megaelectron volts (MeV). The terminology associated with each energy regime a neutron can inhabit is presented in Table 2-2 (The values in the table were obtained from multiple sources [11], [65], [66]).

---

‡ Electron volt is defined as the kinetic energy increase of an electron as it passes through a potential of one volt. Radiation energy is often expressed in units of keV (10^3 eV) and MeV (10^6 eV)

Table 2-2: Neutron energy regimes.

Energy Regime	Energy Range (eV)
Thermal Neutron	< 0.5 eV
Epithermal Neutron	0.5 eV – 50 eV
Fast Neutron	> 50 x 10^3 eV
Cold Neutron	< 1 x 10^6 eV
Medium Energy Neutron	> 1 x 10^6 eV
High Energy Neutron	>10 x 10^6 eV

There are many different interactions of neutrons with matter and the probability of the interactions is strongly dependent on the neutron energy. The dominant interactions of neutrons with matter are illustrated in Figure 2-9 (Page 29) and are listed in detail below:

a. Scattering – Neutrons may collide with nuclei and undergo either elastic or inelastic scattering.

- Elastic scattering is the most probable interaction between a fast neutron and low-Z materials and occurs when a neutron transfers its kinetic energy to the target nucleus without exciting the nucleus [11].

- Inelastic scattering occurs when the neutron transfers some of its kinetic energy to the target nucleus, by which the target becomes excited and the excitation energy is emitted as a gamma ray [11].

b. Absorption – When a target nucleus absorbs a neutron, a wide range of nuclear reactions occur, including nuclear fission (this is more favorable at thermal energies).

- Radiative capture (also named neutron (n)-gamma (γ) reaction) occurs when a neutron is absorbed by the target nucleus which then becomes excited and reaches stability by emission of electromagnetic energy in a form of gamma ray.

- Transmutation occurs when the target nucleus absorbs a neutron that results in an ejection of a charged particle such as a proton or an alpha particle and conversion of one nuclei into another nuclei which is also known as impurity production.

- Nuclear fission reaction occurs when a fissile nucleus such as ^{233}U, ^{235}U, ^{239}Pu, or ^{241}Pu splits into smaller nuclei (fission fragments). As the fission fragments are ejected, an average of 2.5 neutrons are emitted [15] and an average total energy of 214 MeV is released [11].

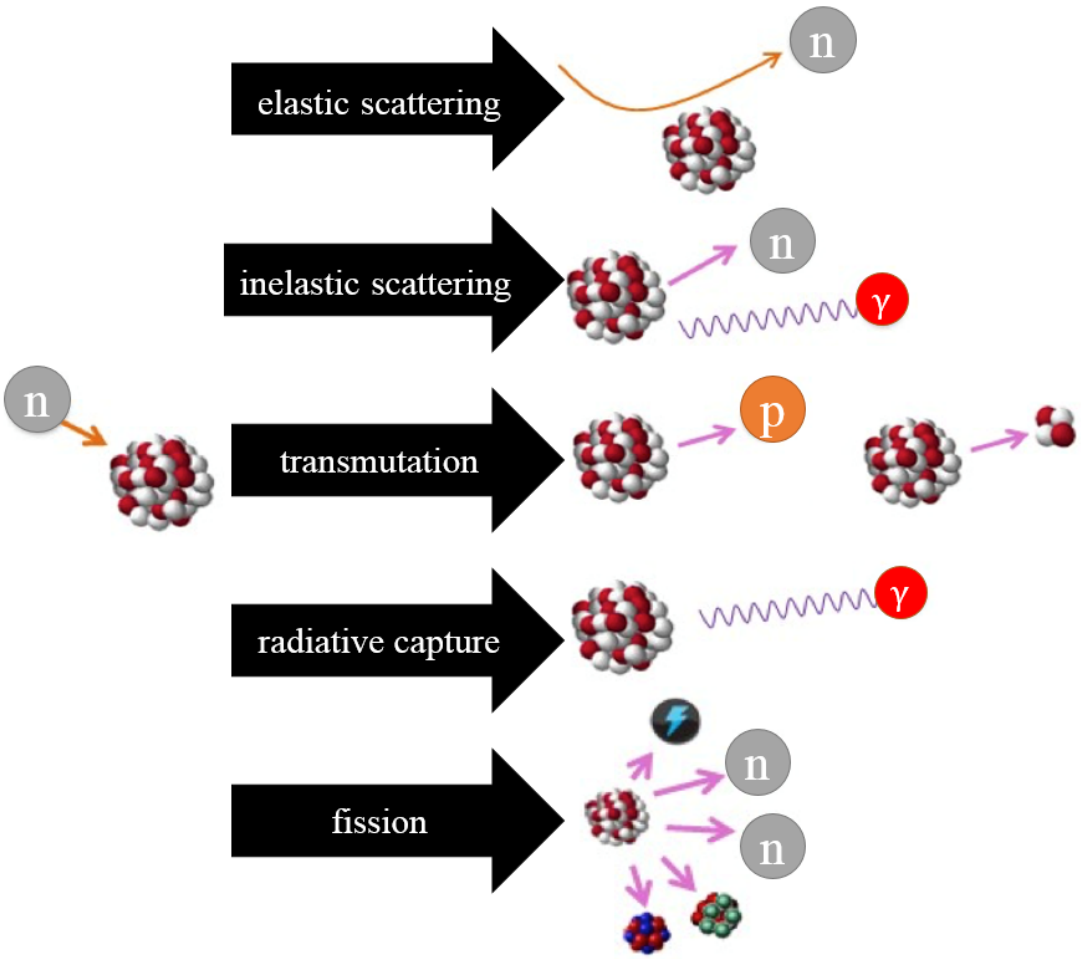

Figure 2-9: Interactions of neutrons with matter where "n" represents a neutron, "p" represents a proton and "γ" represents a gamma ray [67].

2.3.2 Basic Effects of Radiation Damage

The interaction of radiation with materials can instigate useful changes as well as degradation. Radiation effects in materials include structural defects and changes in composition, microstructure and physical/chemical properties.

Radiation-induced changes relevant to this dissertation include atom displacements, dislocations and changes in grain boundaries in fuel cladding materials. These materials are polycrystalline which means they are composed of many single crystals; wherein a crystal is a structure with repeating arrangement of its atoms [68]. Hence, the following sections will focus on defects in crystalline structures (such as metals) produced by radiation. These lattice defects can be categorized into three groups based on their dimension and are presented in Table 2-3.

Table 2-3: Lattice defects in metal crystals [40].

Point defects (changes in atomic positions)	**Line defects (one-dimensional)**	**Planar defects (two-dimensional)**	**Volume defects (three-dimensional)**
Interstitials	Dislocations	Grain boundaries	Cavities
Vacancies	Strings of point defects		Precipitates
Impurities			Cracks

2.3.2.1 Point Defects

Point defects are irregularities in a crystal in regards to the atomic positions, and appear in the form of interstitials, vacancies and impurity atoms. An interstitial atom is an additional atom in a crystal structure that is closely packed into a void between normal lattice sites, while a vacancy is vacant lattice site [68]. Displacement of lattice atoms occurs when the energy transferred to a lattice atom is larger than the energy binding the atom in its lattice site, which causes the atom to be displaced from its lattice position. If the atom that is displaced has enough kinetic energy, it may interact with other lattice atoms to create additional displacements before it comes to rest. Eventually, this atom can become an interstitial atom in the lattice, and the original lattice site becomes a vacancy (Figure 2-10). This atom could also fill in another vacancy already present in the lattice or migrate to the surface of the crystal.

Impurities are common defects in most metals. Impurities are defined as atoms other than the host atoms (Figure 2-10). They are grouped into substitutional impurities, impurity atoms that replace the host atom in the lattice (usually a similar chemical composition and same size as the host atom), and interstitial impurities, impurity atoms that fill the voids around the host atoms (typically smaller size atoms than the host atoms) [68]. Interstitial impurities are commonly present in steels, in which the lattice structure consists of iron atoms with carbon atoms included as interstitial impurities.

A neighboring pair of defects composed of a vacancy and a single interstitial is called a Frenkel pair [68]. Less than 1% of the initially-produced point defects remain long enough to produce observable radiation effects [69]. The others disappear through

thermal processes (such as annealing [70]) that allow the original lattice structure to be restored, however some displaced atoms can initiate secondary displacements and these atoms are usually the reason for defect production. Interstitial atoms and vacancies can diffuse through the lattice; however, the interstitial atoms are more mobile and when they come into contact with other type of defects, such as one- or two-dimensional defects (discussed in the following sections), they are eventually removed from the lattice [70]. Point defects will often diffuse through the lattice until they are either incorporated into one- or two-dimensional defects or until they annihilate each other.

Despite the fact that interstitials and vacancies are constantly removed from their lattice positions, in an operating nuclear reactor environment steady-state populations of interstitials and vacancies exist as these defects are constantly created and annihilated. Rather than distributing evenly, interstitial atoms and vacancies are inclined to aggregate together into clusters. Clusters form one-dimensional defects known as dislocations [71].

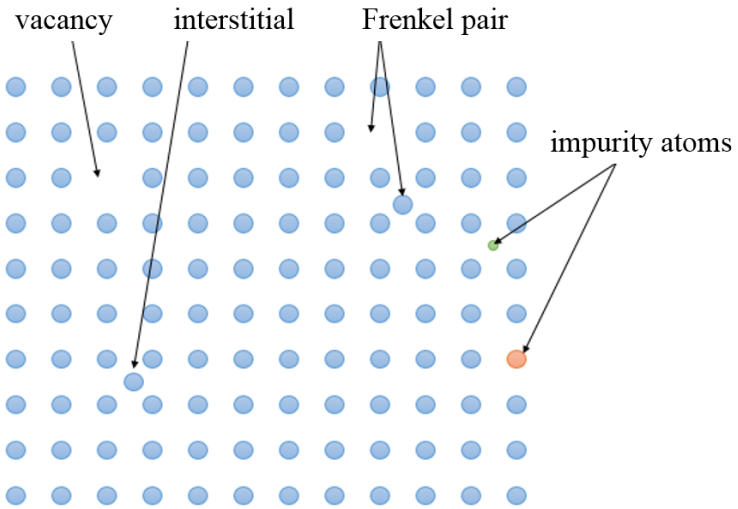

Figure 2-10: Point defects in crystal lattice; schematic representation of vacancy, interstitial, Frenkel pair and impurity atoms.

2.3.2.2 Dislocations

One-dimensional defects represented by the misalignment of some atoms in a lattice line are known as “dislocations” or “linear defects”. Dislocations are generated as a result of stress and are the most significant factors that contribute to strain hardening, a mechanism commonly used to measure the extent of deformation in metals such as nuclear fuel cladding [72].

There are four types of one-dimensional dislocations: edge, screw, mixed and partial dislocations. The edge dislocation is illustrated in Figure 2-11 (Page 34) in which the dislocation appears as an extra half-plane of atoms in the lattice. This is known as a linear defect because the defective points are organized along a single line which is called the “dislocation line”. This is presented along the horizontal center line in Figure 2-11, where the atoms in the top part of the crystal are squeezed together and the ones below the dislocation line are pulled apart [68], [73], [74], [75]. The dislocation line is perpendicular to its Burgers vector and is most visible there due to the strain produced by the dislocation.

A screw dislocation, demonstrated in Figure 2-12 (Page 34), is a type of dislocation that occurs if, for instance, the top or bottom part of the crystal (along the dislocation line) is shifted left or right by one atomic position in the lattice, and is often caused by shear stresses [68], [76]. This results in a line of dislocation which is parallel to the Burgers vector [77], as seen in Figure 2-12; the dislocation line extends from point A to point D and it is parallel to the direction B - C. Mixed dislocations are the ones in which the dislocation line and Burgers vector are not perpendicular nor parallel; mixed

dislocations are composed of both edge and screw dislocations. In order to ease the movement through a crystal lattice dislocations can decompose into partial dislocations.

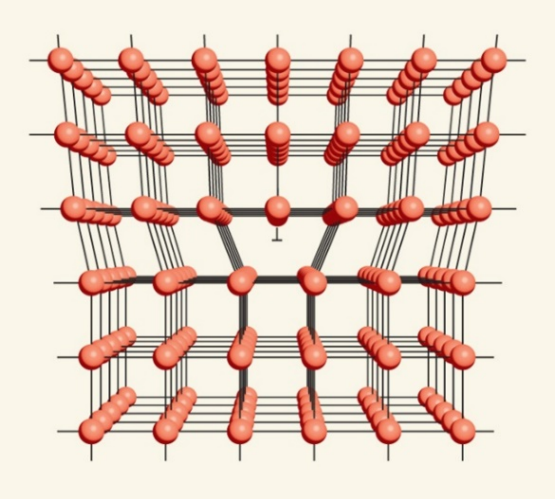

Figure 2-11: The orientation of atoms around an edge dislocation (represented by the symbol ⊥) in a cubic crystal [74], [78].

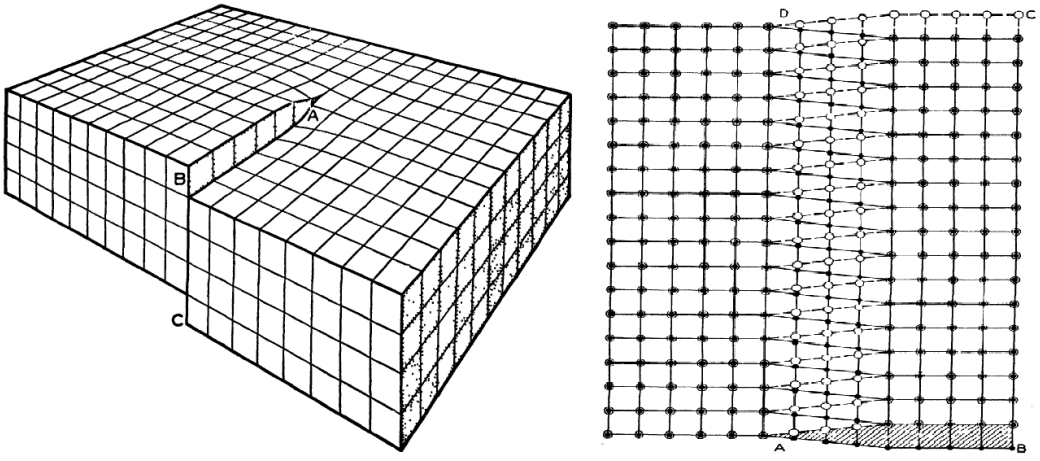

Figure 2-12: Arrangement of atoms around a screw dislocation. The dislocation line extends from point A to point D in the schematic to the right. The atom positions above the dislocation line are represented by hollow circles while below the dislocation line are filled circles [76].

2.3.2.3 Grain Boundaries

Grain boundaries are two-dimensional defects that appear when regions of different crystalline orientation begin to grow separately and then meet. Figure 2-13 shows that the arrangement of atoms in each lattice is identical but the crystallographic orientations of the grains are altered. The separation regions of two grain with different crystallographic orientations are known as "grain boundaries" [75], [68].

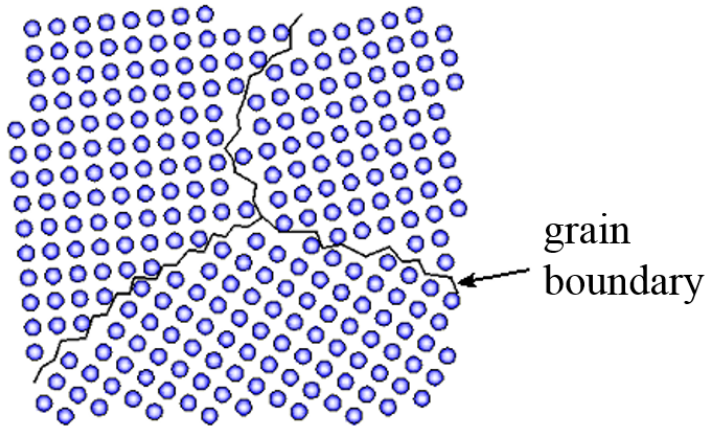

Figure 2-13: Simple schematic of grain boundaries in which the blue circles represent individual atoms and the black lines represent grain boundaries [79].

All of the above mentioned defects are general features of crystalline solids, however; formation of more defects upon exposure to radiation negatively alters the mechanical, electrical and thermal properties of the material of interest which leads to potential loss of the material's integrity. Therefore, identification and analysis of the defects of materials is very important in order to prevent future failure of certain systems, in this case nuclear reactor components.

2.3.3 Macroscopic Effects of Radiation Damage

Irradiation with energetic particles (such as protons, neutrons and fission fragments) may cause microstructural changes in crystalline materials. When these particles interact with the atoms of the target material, any resulting energy transfer may remove an atom from its lattice position.

In a typical nuclear reactor environment (where the average energy of a neutron is 2 MeV and the threshold energy to displace an atom from its lattice position is just 20 to 40 eV), the interactions of a single neutron may cause the displacement of approximately 5×10^4 atoms from their lattice positions [80]. Subsequently, the successful return of these displaced atoms to existing vacancies may occur in approximately nine of out ten interactions [80], while the remaining interactions result in the incorrect rearrangements of these atoms which may adversely affect the mechanical properties of the material. These changes may also result in radiation embrittlement of materials, which is the loss of ductility caused by an increase in the ultimate tensile strength of the materials. Radiation embrittlement is mostly applicable to reactor pressure vessels made out of steel alloys [81], [82].

Another important phenomenon experienced by nuclear reactor materials undergoing vacancy formation is volumetric swelling. Volumetric swelling is most relevant to reactor fuel elements and it is one of the most disastrous effects of radiation damage. The origin of volumetric swelling is the growth of dislocation loops followed by the expansion of voids.

Voids and bubbles are two types of vacancy clusters also known as three-dimensional defects in metal crystals [40]. Bubbles are pressurized vacancies (such as those produced by alpha particles) while voids do not depend on internal pressure [44]. A high density of bubbles and voids results in increased rates of crack formation in the material [83].

Temperature impacts the mechanical properties of the metals and alloys that construct the reactor core. Light water reactors operate at ranges from 280 ˚C to 320 ˚C [11], [38]. When exposed to elevated temperature for a long period of time, the components may suffer a loss of fracture toughness that can lead to brittle failure [84].

Uranium dioxide has a low thermal conductivity (Figure 2-14, page 38), which can instigate stress-induced cracking due to differential thermal expansion between different regions in the material, i.e. since nuclear fission results in heat generation within the pellet, the low thermal conductivity of UO_2 typically results in a radial temperature gradient across the pellet. Generally, the temperature of the center of the pellet is higher than the temperature on the outside of the pellet [85]. In the case of nuclear fuel (in which temperatures of 1400 °C [21] are reached during operation), the hot center expands more rapidly than the cooler outer regions located the edge of the pellet [86]. This results in mainly radial cracks following the grain boundaries due to the circumferential stresses. The resulting fuel pellets include pie-shaped “wedge” cracks [35].

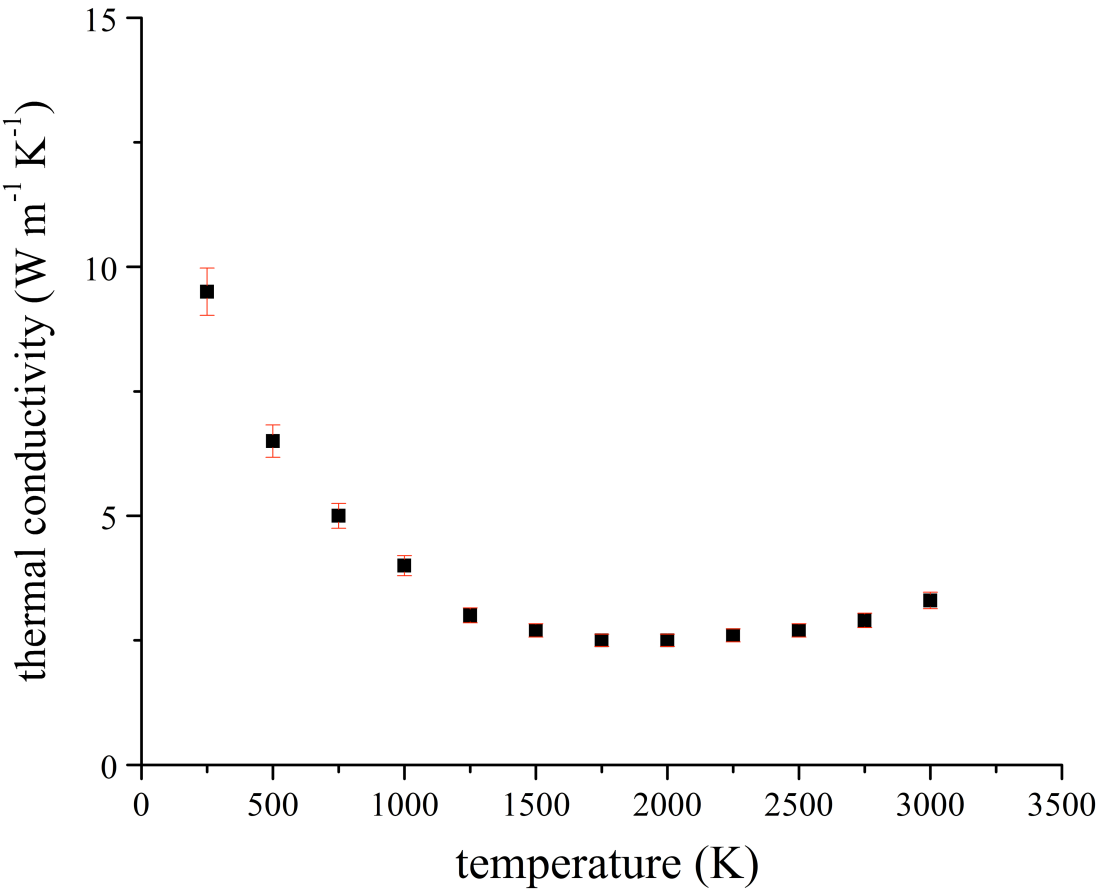

Figure 2-14: The thermal conductivity of UO_2 as a function of temperature [87].

Concurrently, the high temperatures at the center of the pellet cause increased internal strain and compression resulting in densification of the pellet that produces a central void down the length of the pellet [88]. Densification is an occurrence that is the opposite of swelling, causing the increase of the density percentage of UO_2 and the removal of small pores in the pellet. This results into pellet shrinkage and relocation of the pellet fragments towards the cladding which causes pellet-cladding interaction [89]. The extent of densification is roughly proportional to operation time [88].

2.3.4 Fuel and Cladding Behavior and Changes Throughout Irradiation

During irradiation, nuclear reactor fuel elements are exposed to internal stresses that may cause mechanical changes in elasticity and plasticity. These stresses can also induce relocation, swelling, densification and creep (both thermal- and radiation-induced) of the fuel pellet and cladding as well as surface interactions between the pellet, cladding, and coolant. They are typically caused by high concentrations of fission products[§] and extreme thermal gradients [17].

During normal reactor operation, solid and gaseous fission products are produced within fuel pellets. Fission products, if retained in the fuel, are the main cause for swelling in the fuel material and can result in contact between the pellet and cladding [35].

As the reactor power level is increased or decreased in the reactor, the temperature in the core will undergo substantial changes. The thermal stresses caused by the pellet's radial temperature gradient can cause pellet macro-cracking [90]. With the associated release of strain energy, the cracked pellet segments migrate toward the cladding. This process is called fuel relocation or "restructuring" [91]. During irradiation, continuous outward movement of the pellet segments can occur.

At mid-life exposures (typically 3 years [92]), the combined effects of pellet relocation, fuel irradiation swelling and cladding creep-down may result in closure of the

---

[§] The nuclei (fission fragments) formed by the fission of heavy elements, plus the nuclide formed by the radioactive decay of the original fission fragments.

pellet-cladding gap (see schematic of fuel element in Figure 2-2, Page 15). At this point, a reduction in the fuel pellet expansion (such as that caused by a power decrease) can result in partial gap opening. Additional fuel expansion due to progressive fuel swelling (or as a result of a power increase) can cause radial pellet cracks to (partially) close. This increases the effective pellet stiffness and may cause deformation of the cladding [90].

Fission gas atoms, generated by fission, migrate primarily to the grain boundaries of the fuel and cladding. These atoms can move easily along the grain boundaries if there are no sites for gas trapping such as intergranular pores in the material. If trapped, the gas atoms produce bubbles of fission gas on the grain boundaries. The release of fission gas from the fuel may occur if the pressure of the gas bubble exceeds the hydrostatic stress due to plenum gas pressure and/or pellet-cladding mechanical interaction [35]. In this case, the escaped fission gases may exert high pressure on the cladding and cause expansion of the radial gaps. With an increase in fuel temperature, additional fission gas release is expected, which leads to loss of fuel integrity.

3 Photonic Crystals

As described in section 2.3.2 of chapter 2, a crystal is a three-dimensional periodic arrangement of atoms and molecules, whose pattern (known as the crystal lattice, three-dimensional array of points that matches that atom positions) is characterized by repetitive arrangement of the atoms and molecules in material [68]. The distinctive arrangement of the atoms and molecules in a crystal defines a crystal structure [93].

The main interest in using photonic crystals stems from their ability to control the optical properties of a material. Because photonic crystals can be designed to perfectly reflect light, (or to manipulate light to propagate in controlled directions or confine their behavior within specified volumes) they are of enormous benefit to applications involving characterization of material behavior [94], [95]. This can be achieved, for example, by modifying the spatial distribution of the dielectric function [95], [96].

The understanding of photonic crystals, their properties and applications has rapidly advanced within the last quarter century [97], [98]. Photonic crystal structures have been used in a wide range of applications such as lasers, dielectric wave-guide structures and photo-detectors. [99], [100], [101]. In a nuclear reactor, patterning a photonic crystal onto fuel or cladding allows for non-destructive interrogation of, for instance, strain by focusing light onto the photonic crystal and analyzing the returned optical signal. This mechanism is described in section 3.3 of this chapter.

Photonic crystals are periodic, dielectric[**] and metallic materials with structures that affect the motion of photons in a similar way to how semiconductors affect the motion of electrons [94], [102]. The properties of the crystal depend on its composition, geometry and the motion of photons through the lattice. Depending upon their wavelength, photons propagate through the crystal forming a periodic potential in the crystal [102]. Ideally, electromagnetic waves can travel through a periodic potential without scattering, but defects and impurities of the crystal disrupt this free motion [94].

Photonic crystals can be described as one-, two- or three-dimensional structures, depending on the direction of variation of the dielectric function in the photonic crystal [103]. This means that in a one-dimensional photonic crystal the dielectric function varies in one direction while it retains homogeneity in the remaining two dimensions. A two-dimensional photonic crystal exhibits periodicity in two dimensions along with homogeneity in the third dimension and finally a three-dimensional photonic crystal exhibits variation of the dielectric function in all three dimensions. Each of these classifications will be discussed in details in section 3.2.

Manipulation of the repeating pattern on a photonic crystal can be used to produce a structure with a specific band gap [94]. In a photonic crystal, a band gap is represented by the forbidden range of photon frequencies over which photons cannot be transmitted through the material. For instance, a complete band gap means there is no motion of photons allowed in any direction. Controlling these patterns is the most important

---

[**] The optical (such as absorption) and electrical (such as polarization) properties are described by the *dielectric* function of a material.

technique in engineering photonic crystals for the purpose of modulating the propagation of light through the crystal.

3.1 Natural Photonic Crystal Structures

Nature has been producing photonic crystal nanostructures long before scientists grasped the concept of fabricating photonic crystals to manipulate light. Photonic crystals can be found in jewel beetles, butterfly wings, peacock feathers, opals and more. Natural photonic crystals, in species containing them, are one of the primary sources responsible for bright color besides pigmentation [104].

Morpho-type butterflies are found in South America and possess a brilliant blue color. Rather than pigmentation, the color is due to the presence of one-dimensional nanometer-scale photonic crystal structures on the wings. This is due to the different refractive indices[††] in the alternate layers of wing scales [104], [105], [106]. The multilayer lamellar structure features distinct grooves on the wing surface. Figure 3-1 (Page 44) shows a) the Morpho butterfly and b) a scanning electron microscope (SEM) image of the multilayer one-dimensional photonic crystals that are responsible for the blue appearance.

[††] Refractive index or index of refraction is a dimensionless number that measures the refraction of light when passing from one medium into another.

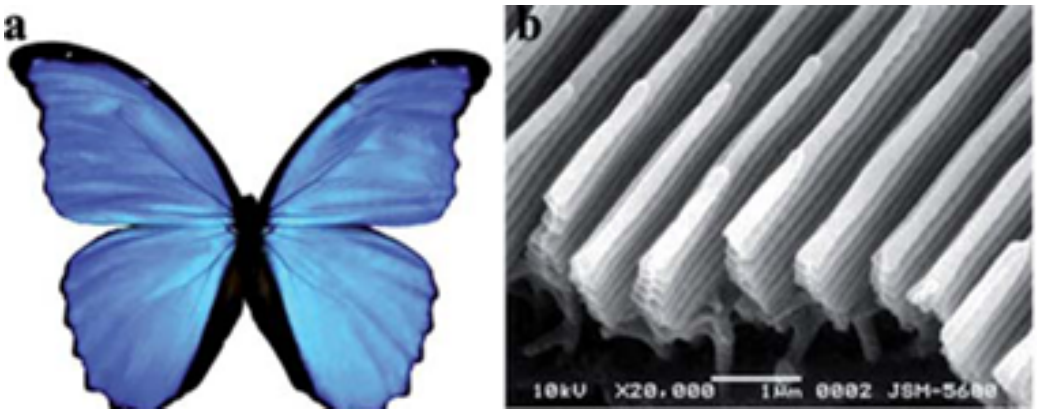

Figure 3-1: a) Morpho butterfly photograph, a naturally occurring one-dimensional photonic crystal; b) A scanning electron microscope image of a multilayer photonic crystal specific to the Morpho butterfly; [107]

The feather of a peacock is an example of a naturally occurring two-dimensional photonic crystal structure. Like the wings of the Morpho butterfly, the colors in the feather do not come from pigmentation but rather from the refraction of light from the photonic crystal surface. The only color that a peacock feather possesses through pigmentation alone is brown.

The scanning electron microscope images in Figure 3-2 b and c show two types of photonic crystals present in a peacock feather that are responsible for the various colors produced by the feather. Various parts of the feathers have arrays of tiny holes neatly arranged in a square pattern. This causes the light to refract off the surface in such a way as to produce the perception of color in the human eye; which colors one sees depends upon the angle of reflection. In the case of Figure 3-2, the two-dimensional photonic crystal structures shown are known to produce a green color upon the angle of reflection [107], [108].

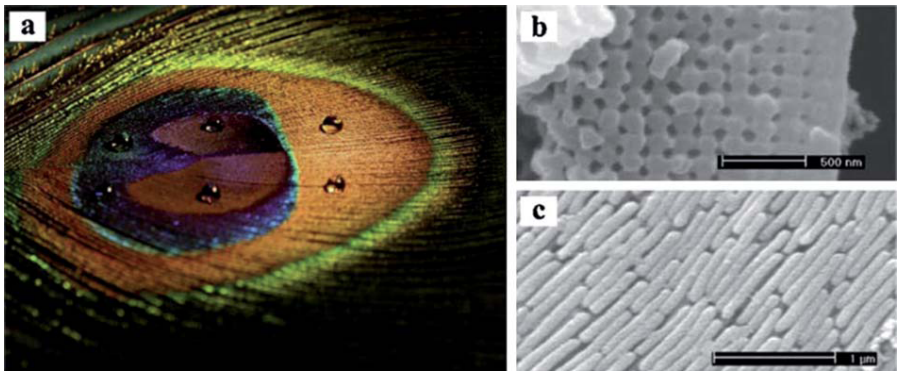

Figure 3-2: (a) Photograph of the eye of a peacock feather, a naturally occurring two-dimensional photonic crystal; Scanning electron microscope images of barbule structures, (b) Transverse cross-section of the green barbule on a peacock feather; (c) Longitudinal cross-section of the green barbule on a peacock feather; [108]

Opal is a mineral featuring a three-dimensional photonic crystal (Figure 3-3). Opal is composed of random chains of tightly packed micrometer-sized silica spheres which differ in size, concentration and arrangement. All of these properties of the opal are accountable for the flow of light and subsequent iridescent color on the opal's surface.

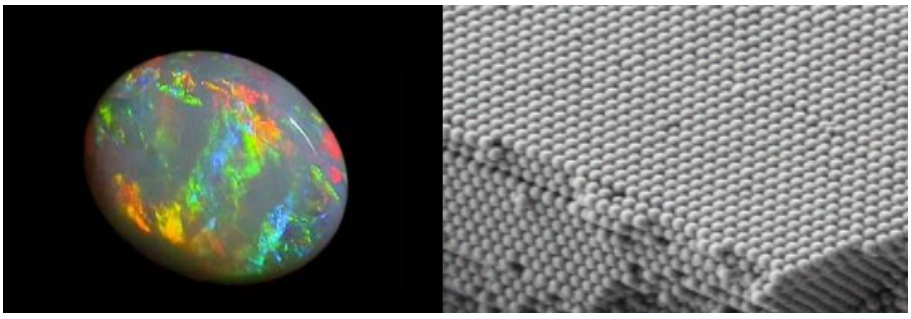

Figure 3-3: Photograph of opal gemstone, naturally occurring three-dimensional photonic crystal (left); Scanning electron microscope image of 1 µm tightly packed spheres in the opal structure (right); [109] [110]

3.2 Engineered Photonic Crystal Structures

Scientists have been able to synthesize photonic crystals for various applications [111]. Similar to the photonic crystals found in nature, engineered photonic crystals can be designed and fabricated as one-, two-, or three-dimensional structures, depending on the periodicity of the dimension.

a. One-dimensional Photonic Crystal Structures

A one-dimensional photonic crystal is represented by a multilayer film consisting of alternating layers of material with different dielectric constants[‡‡]. As explained earlier, this means that the dielectric function varies in only one direction. For example, Figure 3-4 depicts a 1-D photonic crystal that varies along the z axis but is homogeneous in the x and y axes. As the difference between the dielectric constant of the different layers (represented by blue and green color in Figure 3.4) increases, the photonic band gap of the material becomes larger; this means that a larger range of photon frequencies are prohibited through the material [94].

One-dimensional photonic crystals are frequently referred to as "Bragg mirrors" and are generally utilized in dielectric mirrors and optical filters [112]. The concept of 1-D photonic crystals and their optical properties have been analyzed by Rayleigh in 1887 [113].

[‡‡] In the case of photonic crystals the dielectric constant is a function of the periodicity within the material.

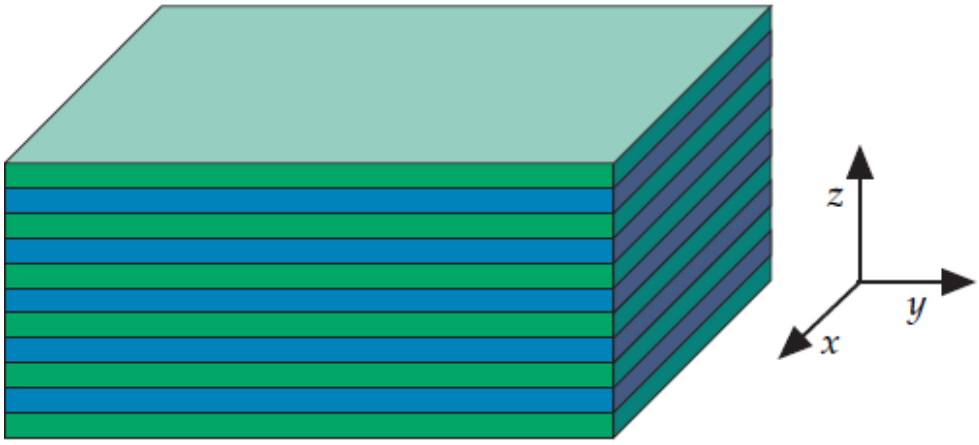

Figure 3-4: Multilayer film – alternating layers of materials (blue and green), 1-D photonic crystal with variation of the dielectric function along the z axis [94].

b. Two-dimensional Photonic Crystal Structure

A two-dimensional photonic crystal is a photonic crystal with a periodically varying refractive index in two dimensions that retains its homogeneity in the third dimension. This is the case of the two-dimensional photonic crystal depicted in Figure 3-5, in which the dielectric function varies in the x-y plane. Adding another dimension to a one-dimensional photonic crystal typically increases the complexity of the behavior of the structure. For instance, in order to produce a repeating two-dimensional photonic crystal one must define the lattice type and the geometry of a unit cell. A unit cell is the smallest repeating unit of volume that contains all of the structural and symmetry information about the lattice. Among the most frequently used lattices are square and hexagonal lattices. For the purpose of this dissertation only square lattices were utilized for the materials of interest. Further information on lattice types can be found in [94], [111].

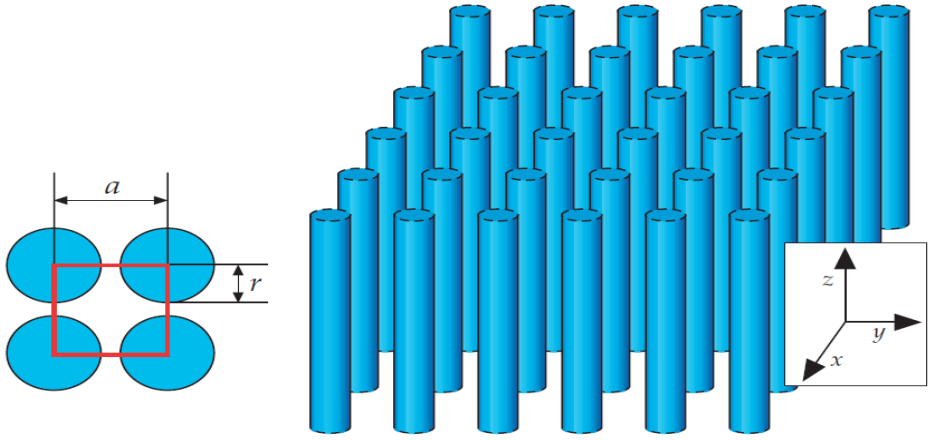

Figure 3-5: Square lattice of dielectric columns, a 2-D photonic crystal, where *r* is the radius and *a* is the lattice constant. The material's homogeneity is retained along the z-axis [94].

Two-dimensional photonic crystals are commercially available in the form of photonic crystal fibers, utilized in telecommunications and sensing applications. The difference between photonic crystal fibers and conventional optical fibers depends on their waveguide properties [114]. The waveguide properties in the photonic crystal fibers are dictated by the arrangements of the air holes in the fiber where in the conventional optical fibers they are influenced by the varying glass composition [114]. Therefore, the ability of photonic crystal fibers to guide exotic wavelengths presents new opportunities for the technology beyond the above-mentioned applications.

c. Three-dimensional Photonic Crystal Structure

A three-dimensional photonic crystal is a loss-less dielectric structure that is capable of guiding and returning light in three dimensions [115]. This is the most challenging photonic crystal for fabrication.

One of the simplest three-dimensional photonic crystals to visualize is called a "woodpile" structure. Woodpile structures produce complete photonic band gaps and are composed of beams of a dielectric material stacked in alternating 90 degree orientations with air-filled spaces, as seen in Figure 3-6.

Unlike one- and two-dimensional photonic crystals, three-dimensional photonic crystals are still far from being commercialized; however, they have bright future in optoelectronics.

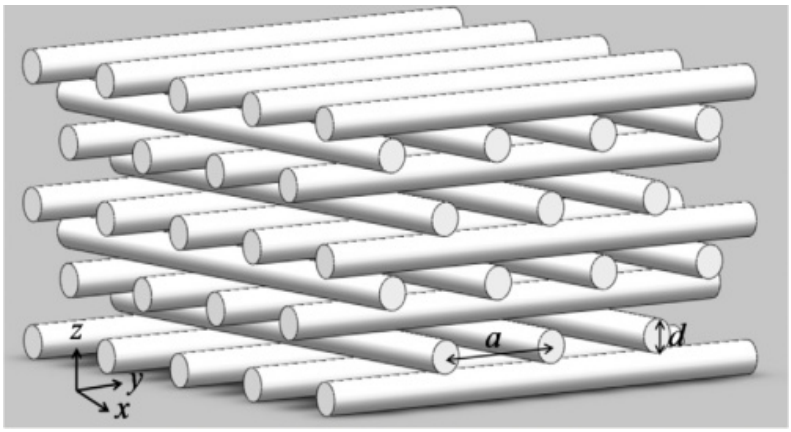

Figure 3-6: Woodpile, a 3-D photonic crystal, dielectric cylindrical rods where *d* is the diameter of the rods and *a* is the lattice constant [116].

3.3 *LightGauge* Sensors

Photonic crystal structures can be generated on materials with the purpose of delivering information regarding the forces acting on those materials. The experimental work in this thesis utilized a design based on engraving the surface of the material with photonic crystals to provide real-time evaluation of the stresses inherent in the bulk material as a function of change in behavior of the light reflecting properties of the

crystals. This is a feasible application for in-situ monitoring of material changes during reactor operation since the sensors are capable of operation in a reactor environment.

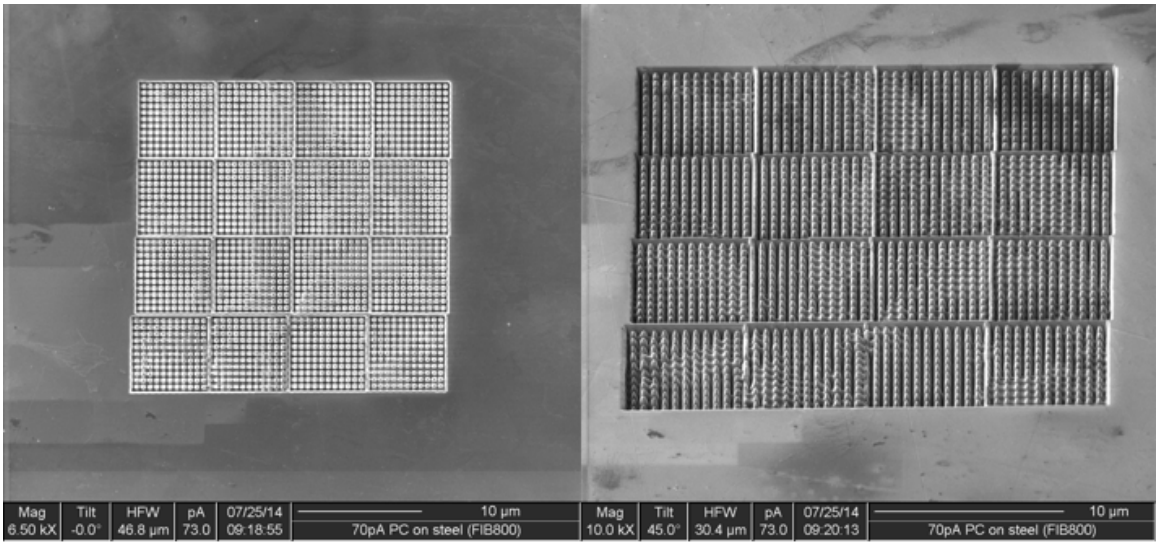

Figure 3-7: FIB micrographs of the same photonic crystal structure (*LightGauge* sensor) etched on the surface of steel; (left) top view, (right) 45 degree tilt view.

Numerous parameters can be monitored using the *LightGauge* sensor. The *LightGauge* sensor applied on the surface of a steel sample can be depicted in Figure 3-7. Such a sensor can be applied over both single grains and grain boundaries. Changes in parameters will result in deformation of the photonic crystal structure which will affect the properties of the refracted light. Through this sensor, changes to an entire grain, changes to a grain boundary and creation of new grains can be observed. If the grain separates, compresses, or shifts, the change in morphology would be evident in the signal from the photonic crystal. Figure 3-8 illustrates an example of how the *LightGauge* sensor can be applied on grain boundaries and single grains.

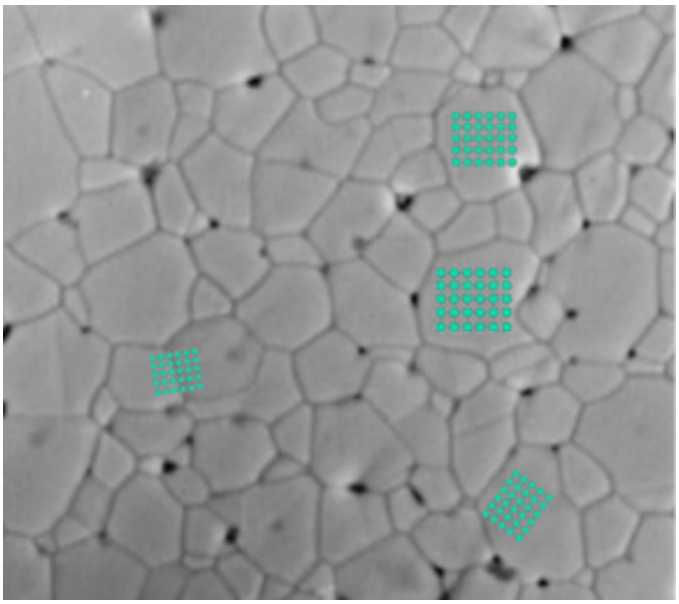

Figure 3-8: Example of how *LightGauge* could be applied to a grain boundary (left) and single grain (right).

The *LightGauge* concept is based on the Fiber Bragg Grating (FBG) technology which uses FBG fiber optic devices to monitor strain and temperature. There is a substantial work already performed on the FBG devices [114], [117]–[119]. These are effectively one-dimensional photonic crystals located at the center of a fiber optic cable. The structure acts as a dielectric mirror, reflecting light at the Bragg wavelength. This work exploits two-dimensional photonic crystals instead of the Bragg grating or Bragg mirror.

4 Nuclear Structural/Cladding Materials of Interest

The nuclear core is defined as the region within the nuclear reactor where the fuel is located and nuclear fission takes place. Core structural materials include all materials used for fuel cladding, fuel assemblies, control rods and monitoring instruments, as well as the entire core supporting structures. Selection of an appropriate material, with the right combination of features for a nuclear applications, is a very common problem among material scientists.

Most nuclear reactors use either steel- or zirconium-based alloys as structural materials and/or fuel cladding. To summarize the discussion in Chapter 2 in regards to cladding materials, an ideal cladding material must feature the following [27]:

- High thermal conductivity – to minimize thermal stresses derived from both normal and transient operating conditions and facilitate transfer of heat from fuel pellet to coolant

- Low susceptibility to radiation damage – to prevent fission product diffusion and maintain cladding structural integrity in a high-radiation field

- Low neutron capture cross section – to prevent the attenuation of neutrons in the cladding material and subsequent neutron activation

- High melting point – for structural integrity, especially in regards to fission product and fuel pellet containment under high-temperature conditions, including transient and accident scenarios

- High corrosion resistance (particularly in water and steam at high temperatures) – to prevent the production of hydrogen and stress-corrosion cracking of the cladding during potential pellet-cladding interactions that may result in cladding breach and failure

- Good mechanical properties – including high tensile strength, low creep, and high ductility, which allows for ease in fabrication

Retaining the above properties, zirconium-based alloys make an excellent uranium fuel cladding material in water-cooled nuclear reactors. Steel-based materials are other materials that have been used extensively as cladding; however, their high neutron absorption cross-section has warranted the use of zirconium alloys for most in-core applications [120]. On another hand, zirconium alloys are more expensive than steel [121].

For the experimental work of this thesis, suitable known reference materials were chosen as an alternative for actual fuel cladding materials. *LightGauge* sensors were applied to both steel- and zirconium-based alloys.

4.1 Steel Alloys

Steel alloys are currently used for many nuclear core components. Fast reactors that are cooled with liquid metals face the challenge of finding a suitable fuel cladding and assembly components that can withstand temperatures up to 750 °C and neutron irradiations greater than 100 dpa [43]. There are steel-based alloys that can fulfill these requirements.

In the vastly demanding design conditions for a commercial fast reactor, steel alloys encounter limitations due to irradiation-induced swelling [122] or to a lack of high-temperature strength [123]. However, steel alloys still allow safe reactor operations in power regimes that are at the lower limit of commercial efficiency [80]. For instance, the Russian Federation's BN-600 is presently the only operating commercial fast reactor, containing fuel cladding composed of austenitic stainless steel with a ferritic-martensitic stainless steel fuel assembly casing [80]. On another hand, carbon steels are major structural materials for reactor pressure vessels and their performance under irradiation is of key importance.

Steels are iron-carbon alloys of which there are many different categories. Carbon steel is one such category that contains 0.02 to 2 weight % carbon. Carbon steel increases in hardness and strength through heat treatment when the carbon percentage content increases; however its ductility is reduced [124]. The concentration of carbon in the steel affects the mechanical properties of the same, by which they are categorized into low-, medium-, and high-carbon type. Low-carbon steels are steels containing less than 0.25 wt. % carbon, medium-carbon steels are the ones containing from 0.25 to 0.55 wt. % carbon, and high-carbon steels are knows as steels with weight percentage of carbon from 0.55 to 2 wt. % carbon [125].

Steel-based alloys used in this work are ASTM[§§] A36 mild steel and AISI[***] 1018 mild steel, most commonly available as hot-rolled and cold-rolled steels, respectively.

[§§] ASTM – American Society for Testing and Materials

[***] AISI – American Iron and Steel Institute

The difference between the hot-rolled and cold-rolled process is the resultant roughness of the surface of steel such that cold-rolling results in a smoother surface and better properties. The chemical composition and mechanical properties of the used steels are given in Table 4-1 below [126], [127].

Table 4-1: Mechanical and chemical properties of the carbon steels utilized in this dissertation.

Mechanical Properties	**AISI 1018 Mild (low-carbon) steel**	**ASTM A36 Mild (medium-carbon) steel**
Ultimate Tensile Strength, psi	63,800	58,000 - 79,800
Yield Strength, psi	53,700	36,300
Elongation, %	15.0	20.0
Chemical Composition, wt %		
Iron (Fe)	98.81 - 99.26	99.00
Carbon (C)	0.18	0.26
Manganese (Mn)	0.60 - 0.90	0.75
Phosphorus (P)	0.04 max	0.04 max
Sulfur (S)	0.05 max	0.05 max
Copper (Cu)		0.20

According to the properties in Table 4-1, the steel 1018 falls under the low-carbon category and steel A36 falls under the medium-carbon category. Both materials are readily available in rectangular bars or round rods, and are very easily machined, weldable and not very expensive to fabricate.

As mentioned before, steel is an iron-carbon alloy with iron as the major constituent in the alloy. The crystal structure of the alloy plays an important role when determining the irradiation effects because of the various differences in microstructures

that are associated with different alloy phases[†††] at different temperatures. The iron phases can be divided into five groups, each corresponding to different temperature range and carbon content in the alloy, presented in Figure 4-1. The microstructures of the steels used for the experimental work of this dissertation, fall under the "ferrite + pearlite" group because of their low carbon concentration and the irradiation temperature is kept below 100 ˚C. The ferrite and pearlite constitutions make these alloys comparatively soft and weak in exchange for exceptional ductility and robustness [68].

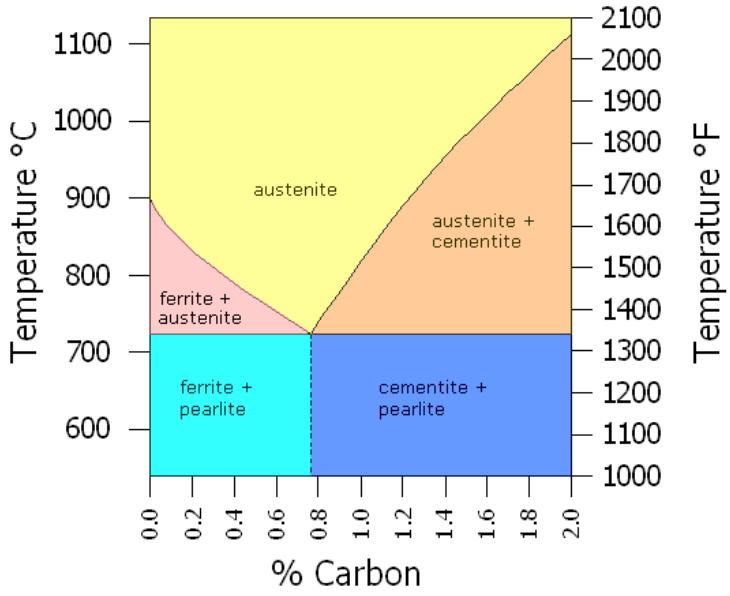

Figure 4-1: Iron-carbon phase diagram [128].

Ferrite refers to a body-centered cubic structure (BCC) of the iron crystal. BCC is a common metallic crystal structure in which a unit cell is composed of eight atoms located at each corner of the cubic lattice and a single atom located in the center of the

[†††] The phenomenon by which a crystal structure changes from one to another due to a change in temperature is referred to as a phase transformation.

cube [68]. Figure 4-2 depicts the BCC, representing a collection of multiple unit cells (left), following by one space-filling unit cell from the collection (middle) and ending with a reduced-sphere unit cell.

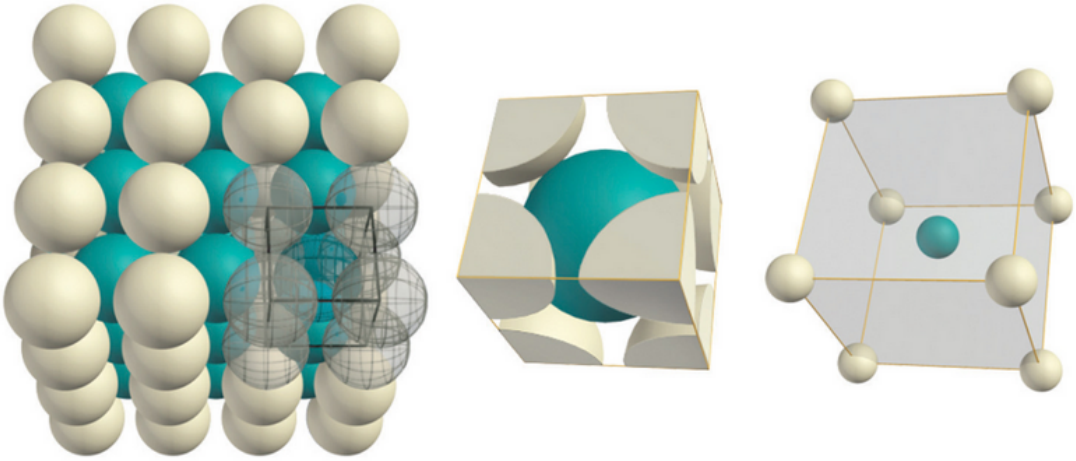

Figure 4-2: Representation of a body-centered cubic structure: collection of multiple unit cells (left), space-filling unit cell (middle) and reduced-sphere unit cell (right) [129].

On the other hand, pearlite is a layered structure composed of alternating layers of ferrite and cementite that occurs in parts of the steel where there is an increase of the carbon content. Steel with carbon content less than 0.83 weight percent, formed at 727 ˚C on very slow cooling, incorporates the pearlite structure [130].

The strength and properties of plain carbon steel depend on its composition and details of the particular phases present in the finished product. The carbon content of plain carbon steel varies from 0.02% to a little less than 2%. The structures, and thus the properties of the steel depend on the carbon content and particularly the position of the alloy in respect to the eutectoid point on the phase diagram. The eutectoid point is

analogous to the eutectic point on phase diagram, the difference being that at the eutectic point, the material transitions from a homogeneous liquid to two intermixed solid phases at a single temperature, while in the case of the eutectoid that transformation is from a single homogenous solid to two intermixed phases at a single temperature. The eutectoid point for carbon steel exists at 727 °C and at a concentration of 0.76% carbon. At temperatures above the eutectoid, the BCC ferrite structure begins the transformation to the face-centered cubic structure (FCC) austenite. Upon cooling, a steel of eutectoid composition transitions to a composition consisting of 100% pearlite. Pearlite is characterized by laminated layers of ferrite and carbide (Fe_3C). The lamina is always found in a ratio of 9 to 1 in terms of mass, with the carbide layer being the smallest. The exact size of these structures is dependent on the specifics of the cooling process. Pearlite can be characterized as course or fine, and all levels in between. The properties of the steel vary with the size of these structures. Very rapid cooling can also produce bainite structures where the carbide forms small needle like structures within the ferrite.

For steel that does not contain the eutectoid concentration of carbon, a proeutectoid phase forms before crossing the eutectoid temperature and forming pearlite. Steels containing less carbon than the eutectoid concentration are known as hypoeutectoid steels; in this case the proeutectoid phase is ferrite. The relative quantities of proeutectoid ferrite and pearlite can be found by examining the position of the alloy on the phase diagram in comparison to the eutectoid concentration. In the case of the steel 1018 used in this work, one would expect to find approximately 75% of the structures will be proeutectoid ferrite, surrounding 25% pearlite. The actual size of these structures depends on the thermal treatment of the steel. Steels containing carbon higher than the

eutectoid concentration are known as hypereutectoid steels, for these steels the proeutectoid phase is cementite. In the case of hypereutectoid steels, the proeutectoid phase is limited to less than 20%, with the remaining structures being pearlite.

The properties of steel are not only dependent on the concentrations of the elements in the material, but also on the thermal treatment of the steel. As temperatures are increased, diffusion becomes more active in the solid, and the material tends towards the lowest energy state. This results in large microstructures and a soft material. Some of the possible structures are as follows, in order of softest to hardest:

- Spheroidite: this material is characterized by carbide that is expressed as small spherical balls dispersed within a matrix of the ferrite. This microstructure is achieved by holding the steel at temperatures just under the eutectoid for long periods of time.
- Course pearlite: this material is relatively soft, as the microstructures are large, though the laminated pearlite structure is still apparent.
- Fine pearlite: this material is characterized by smaller microstructures and is harder than course pearlite.
- Bainite: this material is characterized by its carbide composition that forms small needle like microstructures along with no evident lamina; if the phase transition happens quickly enough, there is not sufficient time for diffusion to produce pearlite lamina, rather it produces a structure known as “martensite”. This is recognized as a diffusionless transformation from austenite where the energy is removed so fast that often the phase changes from FCC to BCC

cannot complete. This process produces very brittle structures that are not often used without tempering.

4.2 Zirconium Alloys

The most commonly used fuel cladding for both light and heavy water-cooled reactors is Zircaloy, an alloy of mostly zirconium and aluminum also containing low percentage of tin, niobium, iron, nickel and other metals. Its common use is due to its relatively good mechanical properties and excellent corrosion resistance, as well as its low neutron capture cross-section. While pure zirconium is exceptionally resilient to corrosion, alloying of this material is necessary because of its low strength at high temperatures, but in comparison to steel alloys, zirconium alloys have higher thermal properties. The high corrosion resistance of these alloys is due to the protection of a metal-oxide interface by a tightly adhered protective oxide film.

Zirconium alloys are used in nuclear systems due to their special material properties as its alloys have an anisotropic crystal structure, which implies identical properties in all directions [131]. This property is due to the material's hexagonal close packed (HCP) lattice structure. The HCP structure is made out of three layers of atoms arranged in hexagonal patterns. An HCP unit cell, as depicted in Figure 4-3, consists of six atoms both in the top and bottom layer that create a regular hexagon with an additional atom in the center of each hexagon [68]. The middle layer, consisting of three atoms arranged in a triangular pattern, is organized in a way so the closest possible packing of atoms is accomplished.

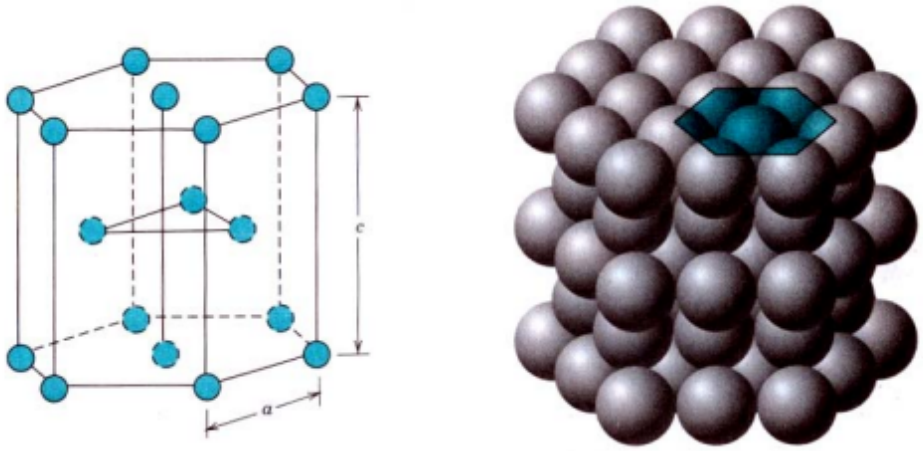

Figure 4-3: Representation of a hexagonal close packed (HCP) structure: reduced-sphere unit cell with two lattice parameters, a and c (left) and collection of multiple unit cells (right) [132]

Zirconium alloys were first developed for use as structural materials in fuel rods and fuel assemblies in PWRs and BWRs under the designations zircaloy-2 and zircaloy-4. The need for suitable materials in reactor designs of different irradiation environments and water chemistries led to revolutionary developments of reactor materials in the countries expanding nuclear power industries, specifically France, Japan, Russia and the United States. Many of the variations in the zirconium alloys included small amounts of oxygen (~0.1%), iron (~0.01–0.4%) and chromium (~0.1%), which spawned the current generation of zirconium alloy fuel rod claddings known as M5, MDA, ZIRLO and E-635 [80], [133]. Also developed were duplex alloys, which included an enhanced corrosion resistant outer layer of a different alloy composition is applied to a zircaloy-4 base material. These duplex alloys are used in some high burn-up applications. The mechanical properties and chemical composition of the zircaloy-4 material used for the experimental work of this study are presented in Table 4-2 [134].

Table 4-2: Mechanical and chemical properties of the zircaloy-4 utilized in this study.

Mechanical Properties	**Zircaloy-4 (Alloy Zr4) (UNS R60804)**
Ultimate Tensile Strength, psi	74,600
Yield Strength, psi	55,200
Modulus of Elasticity, ksi	14,400
Chemical Composition, wt %	
Zirconium (Zr)	97.56 - 98.27
Tin (Sn)	1.20 - 1.70
Iron (Fe)	0.28 - 0.37
Iron (Fe) + Chromium (Cr)	0.18 - 0.24

4.3 *LightGauge* Sensor Design and Fabrication

4.3.1 MIT Photonic-Bands (MPB) Software Design Simulations

As described in Chapter 3, photonic crystals can be designed to perfectly reflect light to manipulate light to propagate in controlled directions or to confine the behavior of light within specified volumes. They are of enormous benefit to applications involving the characterization of a material's behavior.

With the rapid evolvement of photonic crystals, the technical requirements and approaches for these systems are becoming more complex to the extent that the final product becomes highly dependent on the design software. Simulations of photonic structures are typically performed with MIT photonic-bands (MPB) software [135]. Joannopoulous Ab Initio Physics group [136] at Massachusetts Institute of Technology (MIT) has developed this software and it is used for calculating band structures and electromagnetic modes of periodic dielectric structures.

The Finite Difference Time Domain (FDTD) model is utilized in the MPB software. This is a numerical analysis technique that finds approximate solutions for differential equations. In the case of a photonic crystal, it solves the Maxwell's equations [94]. MPB is also designed to simulate repeating regular structures. Since the *LightGauge* sensors fulfill these requirements, the MPB software was used to simulate their design using parameters such as the lattice constant of the structure, the geometry of the unit cell and the materials used.

4.3.2 Fabrication of *LightGauge* Sensors

Prior to inserting the steel and Zircaloy samples in the focused ion beam for micromachining, they required initial preparation. First, a series of samples were produced using standard machining techniques. The samples are shown in Figure 4-4. Steel and Zircaloy rods were cut into 32 x 13 mm rectangles, each 3 mm thick, with two holes away from the center to allow for attachment to a holder. Each sample was of average weight of 6.77 grams. The dimensions of the samples were chosen as such in order to fit primarily in the FIB as well as all the other integration instruments. There were two types of samples, one was the dog-bone shape (left photograph in Figure 4-4) and one was a plain rectangle (right photograph in Figure 4-4). The dog-bone sample was made as such so it can serve as a tensile specimen for future experiments.

The second step of the fabrication process was the polishing of the samples. The samples were polished using a Buehler Vanguard automated polisher using abrasives with 50 nm particle size. Polishing usually removes all deformations and scratches of the

material. While there is no need for a smooth surface to produce a photonic crystal, it is very advantageous for milling consistency.

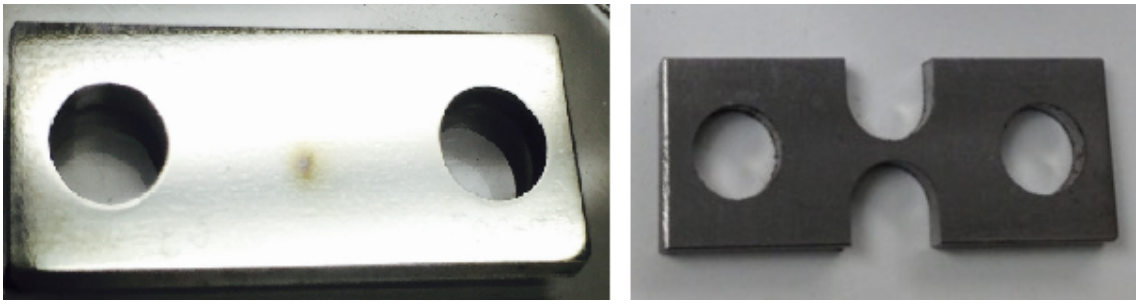

Figure 4-4: Photographs of rectangle type sample (left) and dog-bone type sample (right); in this example both samples are made out of steel.

The last step of the fabrication process is the micromachining of the *LightGauge* sensors on the steel and Zircaloy samples. The *LightGauge* sensors were milled in the center of the sample as shown in Figure 4-5.

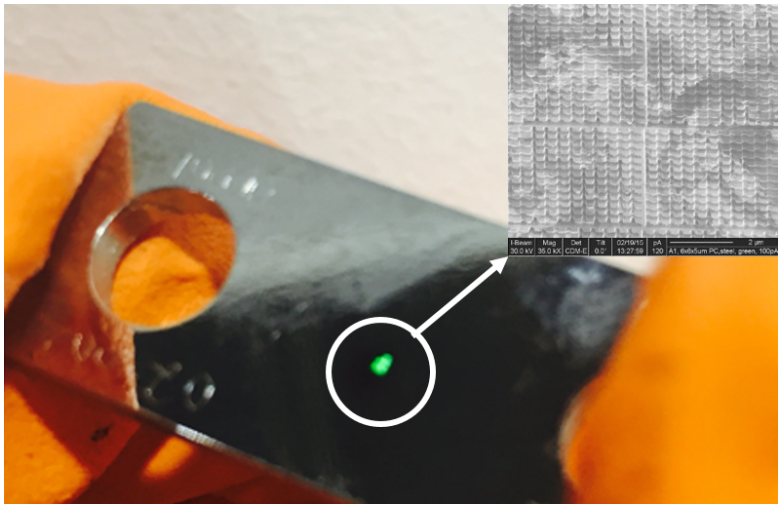

Figure 4-5: Image of steel sample, representation of light reflection of the *LightGauge* sensors; green light reflection in the center of the sample.

As mentioned earlier, the square lattice with square pillars (Figure 4-6) was employed in the current design as being one of the easiest to produce. According to MPB simulations, this design proved to have desired bandgaps. A milling script was developed to use with the FIB instruments and employed to produce the *LightGauge* sensors.

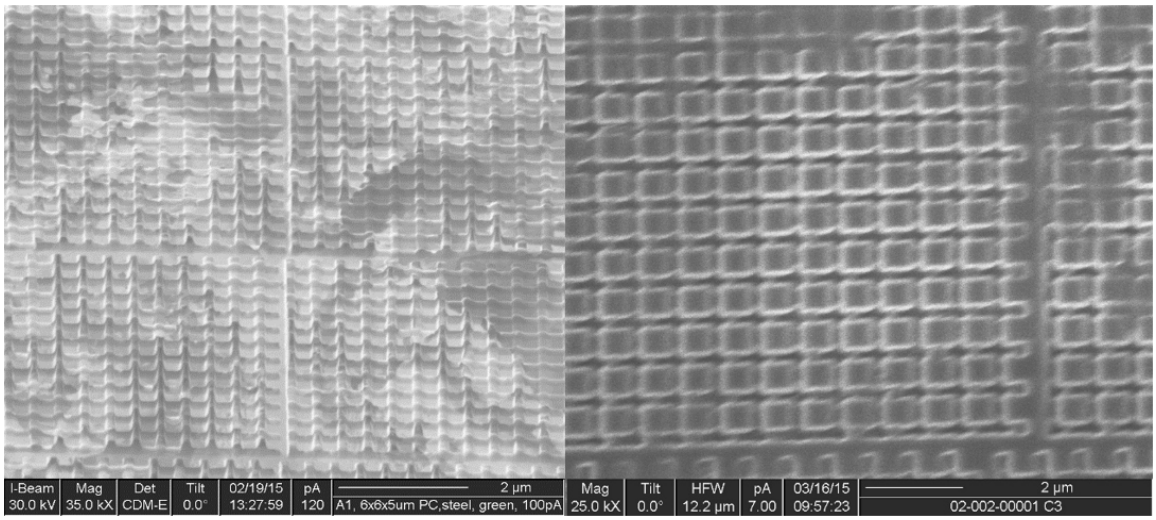

Figure 4-6: FIB micrographs; 0 degree tilt view of a typical square lattice on steel sample with square pillars.

Figure 4-7 and Figure 4-8 represent a typical FIB micrograph of the surface of a two-dimensional photonic crystals and show the typical layout of the fabricated sample on steel and Zircaloy, respectively. Several *LightGauge* sensors were written on both steel and Zircaloy samples. Each sensor contained 25 photonic crystals fabricated in a 5 x 5 array. Each *LightGauge* sensor written on steel contained 324 pillars, corresponding to an 18 x 18 grid. Each *LightGauge* sensor written on Zircaloy contained 121 pillars, corresponding to an 11 x 11 grid.

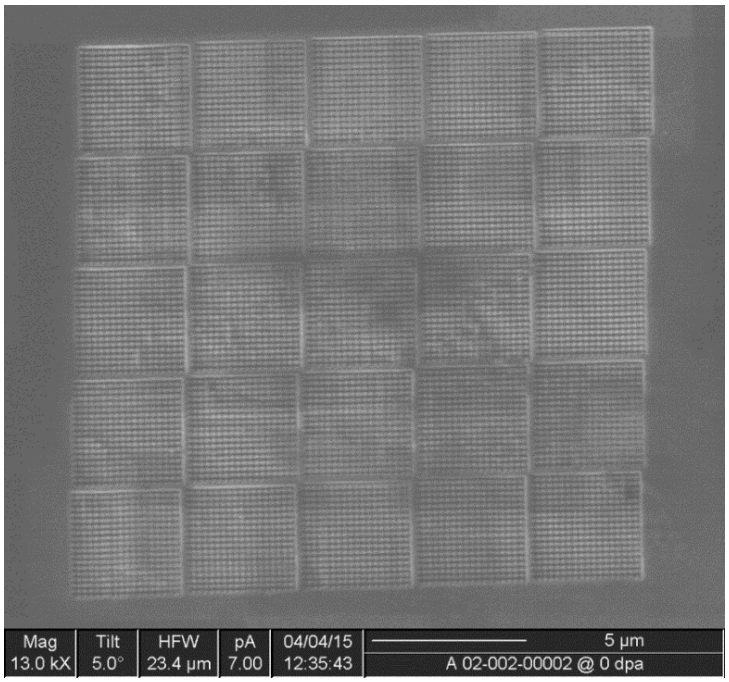

Figure 4-7: FIB micrograph; typical layout of a single *LightGauge* sensor on a steel sample.

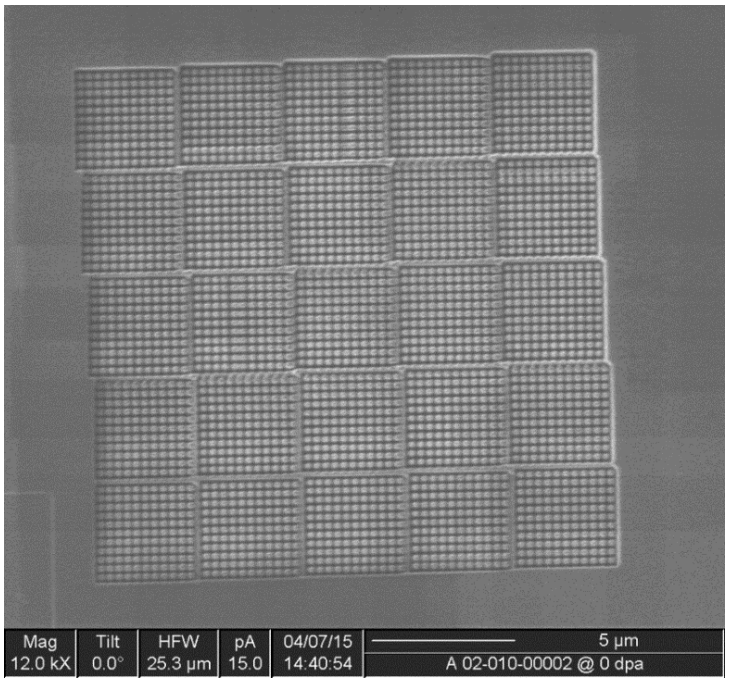

Figure 4-8: FIB micrograph; typical layout of a single *LightGauge* sensor on a Zircaloy sample.

The experimental section of this thesis covers the irradiation of the samples. The samples were subjected to six different irradiation doses. Therefore, each sample contained six *LightGauge* sensors, corresponding to each irradiation dose. Figures 4-9 and 4-10 represent the layout of the *LightGauge* sensors on the steel and Zircaloy samples, respectively.

The FIB and the dual beam were used to mill the photonic crystals. As seen from the above figures, the pillars of the photonic crystals in either sample are not perfect; there is noticeable rounding of the tops of the pillars and the sides are sloped. It is possible to achieve near perfect structures with milling at lower beam currents; however, completing those structures is very time consuming.

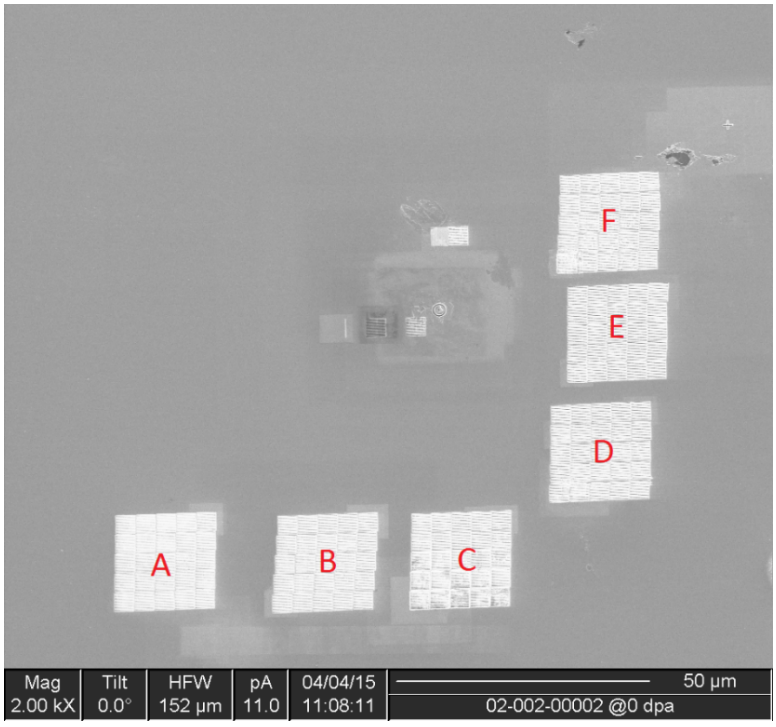

Figure 4-9: FIB micrograph; overview of *LightGauge* sensors position on steel sample.

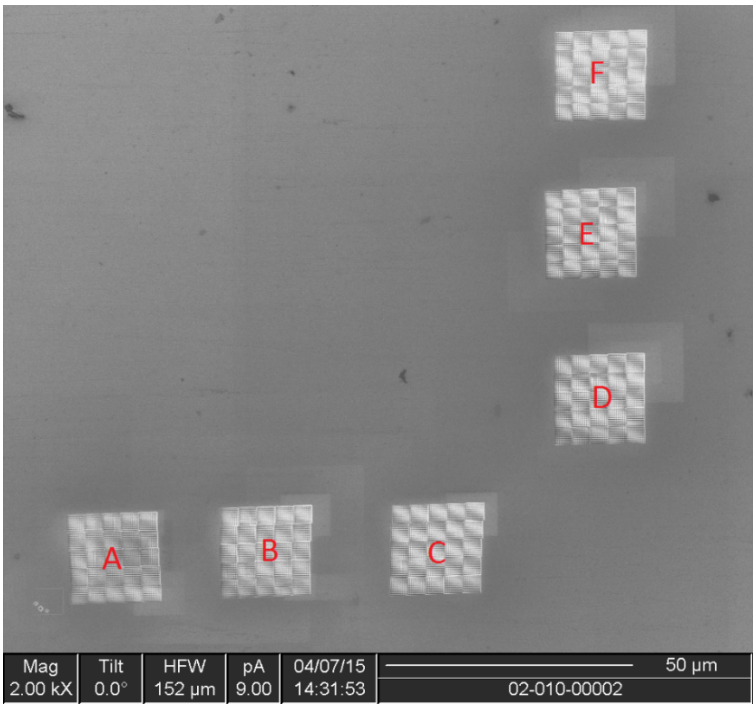

Figure 4-10: FIB micrograph; overview of *LightGauge* sensors position on Zircaloy sample.

5 Experimental Facilities, Design and Setup

The majority of the experimental work presented in this dissertation was performed at Idaho State University's Research and Innovation in Science and Engineering (RISE) complex. The RISE complex features a proton beam accelerator, which was used to induce damage in the materials of interest and a state-of-art microscopy laboratory, used for machining and imaging the *LightGauge* sensors. In addition to that, one other experiment was performed at the University of Maryland's Radiation Facilities.

5.1 RISE Proton Beam Accelerator – "Pelletron"

5.1.1 Description

The RISE complex 12SDH-4 Pelletron is a four million volt, gas-insulated, electrostatic tandem-type accelerator that can be used to accelerate a variety of ion species (negative and positive ions) over a broad range of energies for use in ion beam analysis, ion implantation, nuclear physics experiments and other applications. The name "Pelletron" originates from the pellet chain through which the charging current is generated. The chain rotation transfers charge to build up voltage potential between the terminal and ground. This potential is then used to accelerate a variety of ion species. The accelerating tube, consisting of a pair of ceramic and metal tube assemblies on each end of the HV terminal, provides an insulated high-vacuum environment through which the ion beam can travel [137].

The Pelletron is housed in a steel pressure vessel (Figure 5-1) filled with sulphur hexafluoride (SF_6), which serves as an insulating gas. The steel pressure vessel is known as the "accelerating tank". Other components of the system include a high voltage insulating support structure that features lateral and vertical adjustment for beam alignment, a charging system to generate the high potential, and an evacuated acceleration tube through which the ion beam passes [137].

The support structure provides physical support to the terminal and accelerating tube while also acting as electrical insulation and as a potential distribution between the terminal and ground. The terminal charging system, ion stripping unit and electronics are contained in the high voltage terminal [137].

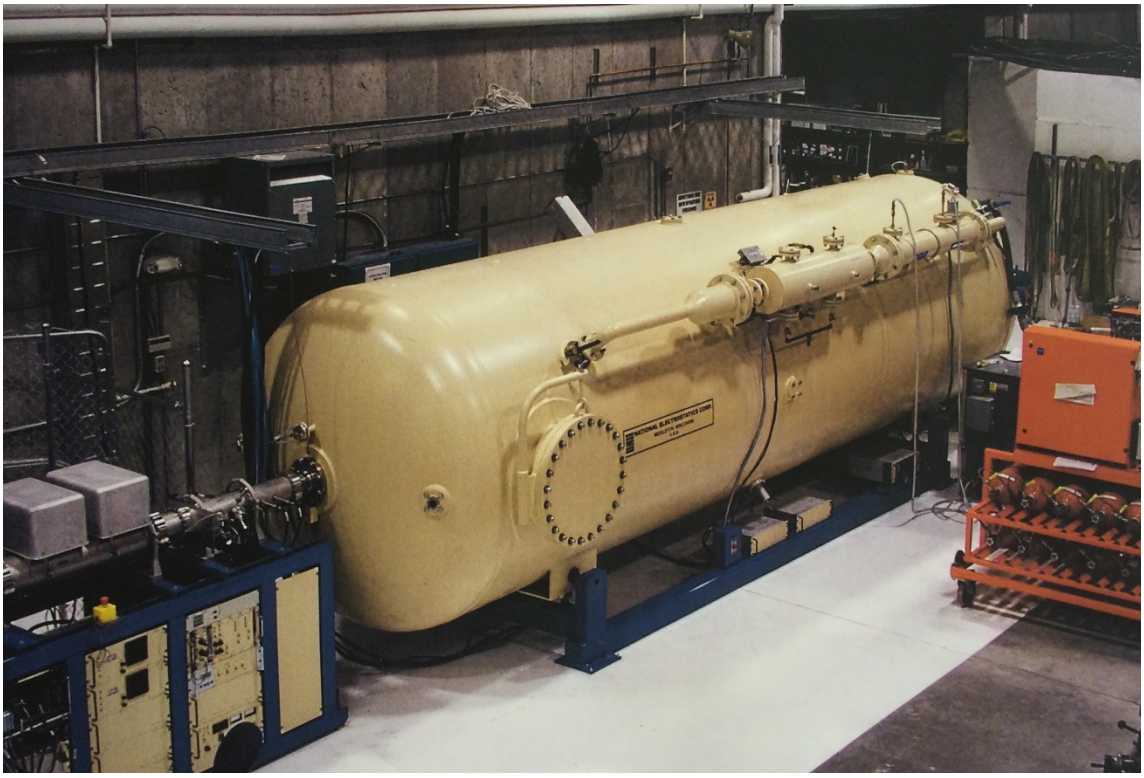

Figure 5-1: National Electrostatic Corp. (NEC) 12SDH-4 Pelletron.

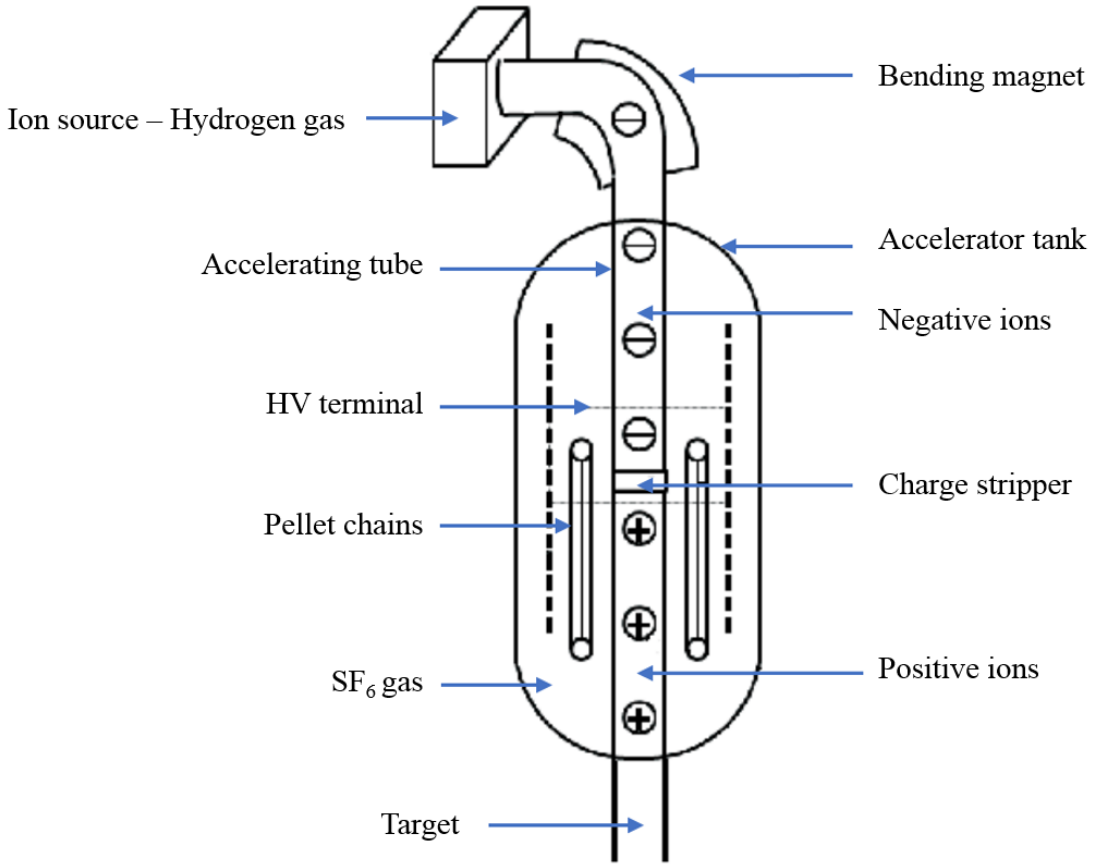

Figure 5-2: Schematic diagram of the Pelletron.

The constituents stated in the following explanation are presented in Figure 5-2 above**.** The principle of operation is quite simple: negative ions produced in the ion source (hydrogen gas) are pre-accelerated to modest energies (about 50 keV) and injected into the low-energy acceleration tube where they are accelerated to the positively-charged high-voltage terminal. Inside the terminal, the negative ions enter a "stripper" (a long narrow tube filled with nitrogen gas) where two or more electrons are removed ("stripped") through collisions with the stripper gas, and the resultant positively charged ions are then repelled by the terminal potential and undergo a second acceleration. The final energy of the ions emerging from the accelerator is represented by V(n + 1)e, where

V is the accelerator voltage, n is the charge state of the ion, and e is the electron charge. Assuming a maximum 4 MV operating potential, singly-charge ions will be accelerated to 8 MeV, doubly-charged ions 12 MeV and so forth [137].

The high voltage in the Pelletron is generated by means of a mechanical charging system. A charging chain consisting of steel pellets connected by nylon insulating links rotates around two pulleys: one at the ground end, driven by an electric motor, and one in the high voltage terminal. Positive charge is induced on the pellets at the ground end, which then carries the charge to the terminal. Similarly, negative charge is induced on the pellets in the terminal, which are then carried to ground. The 12SDH-4 contains four such charging chains for a total charging capacity of more than 600 μA [137].

5.1.2 Ion Source

The Pelletron is equipped with a Canberra negative hydrogen ion source that is specialized for use in accelerators. Negative ion sources produce beams of atoms with additional electrons. Negative hydrogen ions, specifically, have very weakly bound electrons with binding energies of 0.754 eV in comparison to the 13.6 eV binding energy of neutral hydrogen.

Ion sources typically have two components, a plasma generator and an extraction system. The hydrogen is present in the system in the form of a gas and the electrical discharge forms the plasma. The extraction system is composed of an electrode with an aperture from which the desirable ions are extracted and are further accelerated while the undesirable ions are removed. With the Pelletron, the desirable species are high energy ions generated at the high-energy side of the Pelletron; however, for the purpose of this

work the low-energy side of the Pelletron was utilized. In this case, the desirable species are negative hydrogen ions. Both the high- and low-energy sides of the Pelletron, together with its applications associated to the experiments performed for this research, are discussed in section 5.2 of this chapter.

5.1.3 Current Monitoring

The fundamental quantity of every charged-particle beam is its ion beam current. Ion beam current is the rate of ion flow past a given point. Since the electric charge is quantified as a multiple of the electron or proton charges (negative or positive 1.602×10^{-19} C respectively), the total number of charged particles can be effectively counted. If the incident beam's cross sectional area is known, then a Faraday cup can serve as a fluence meter (particles/area).

A Faraday cup (FC) is a device made out of conductive material (metal), commonly used to monitor beam current in charged particle accelerators. Typically, the Faraday cup is connected to an ammeter, which is used to collect and measure the total particle charge carried by the ion beam. This method of charge collection, where the FC must intercept the beam of interest in order to perform the measurement, is considered a destructive method. Nevertheless, FC still provides precise information of the beam current in a very simple manner.

Faraday cups are not capable of directly providing a measurement for absorbed dose in a material at a given location along the beam. Rather, since dose is equivalent to the product of the beam fluence and the mass stopping power, the FC can be used to determine absorbed dose if the mass stopping power of the particles is also known.

The RISE Pelletron Faraday cup (Figure 5-3) control unit consists of a power switch and an actuator switch with “IN” and “OUT” positions which makes its operation, and the insertion and removal of the cup from the beam path very simple. The Pelletron consists of two Faraday cups: a low-energy Faraday cup located before the accelerating tank, i.e. low-energy side of the Pelletron and a high-energy Faraday cup located after the accelerating tank, i.e. high-energy side of the Pelletron.

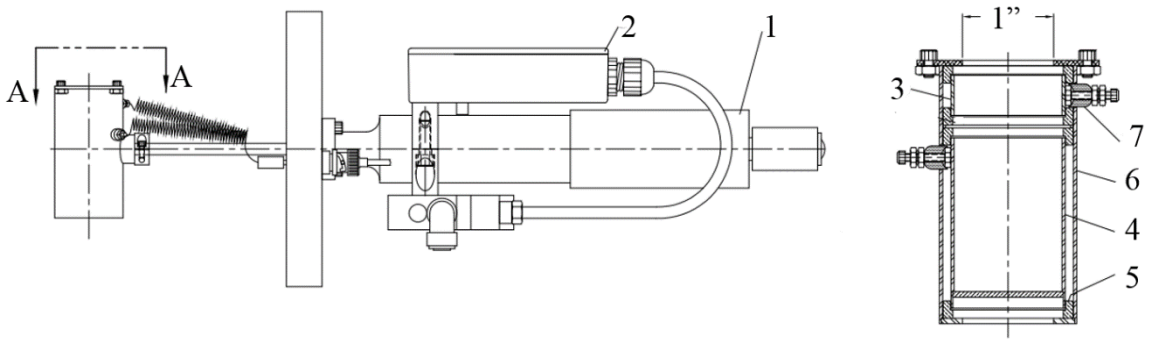

Figure 5-3: National Electrostatics Corp. Faraday Cup: Model FC50 [137]

1	actuator, 2” travel
2	pneumatic drive limit switch box 2” travel assembly
3	Faraday cup suppressor
4	Faraday cup collector
5	Faraday cup insulator
6	Faraday cup shield
7	ceramic insulator bead
A-A	detailed cup assembly

5.2 Pelletron Experimental Apparatus

The pelletron accelerator, described in section 5.1.1, was employed for the majority of the experimental work presented in this dissertation. The purpose of these experiments was to study charged particle irradiation damage in nuclear fuel cladding materials. Specifically, the pelletron was utilized as a negative hydrogen ion radiation source to induce damage in the *LightGauge* sensors written on steel and zircaloy samples. In order to proceed with the experimental work, two configurations of the experimental setup were developed; one at the high-energy side and one at the low-energy side of the pelletron. Each configuration employed two different experimental stations. All configurations are discussed in detail in the following sections.

5.2.1 High-energy Beamline Configuration

Initially, the aim was to irradiate samples with accelerated protons at the so called "high-energy" side of the pelletron, past the accelerating tank. A beamline configuration at the high-energy side of the pelletron was designed and built, and its final configuration is shown in Figure 5-4. The components of the beamline configuration, as seen from left to right in Figure 5-4, include an experimental station, beam profile station, turbo pump, gate valve and the high-energy side exit of the accelerating tank. Two supporting structures were custom-built to reinforce the beamline configuration, represented by 4 in Figure 5-4. The high-energy beamline configuration employed two experimental stations: one without cooling (named setup "A") and one with cooling accessories (named setup "B").

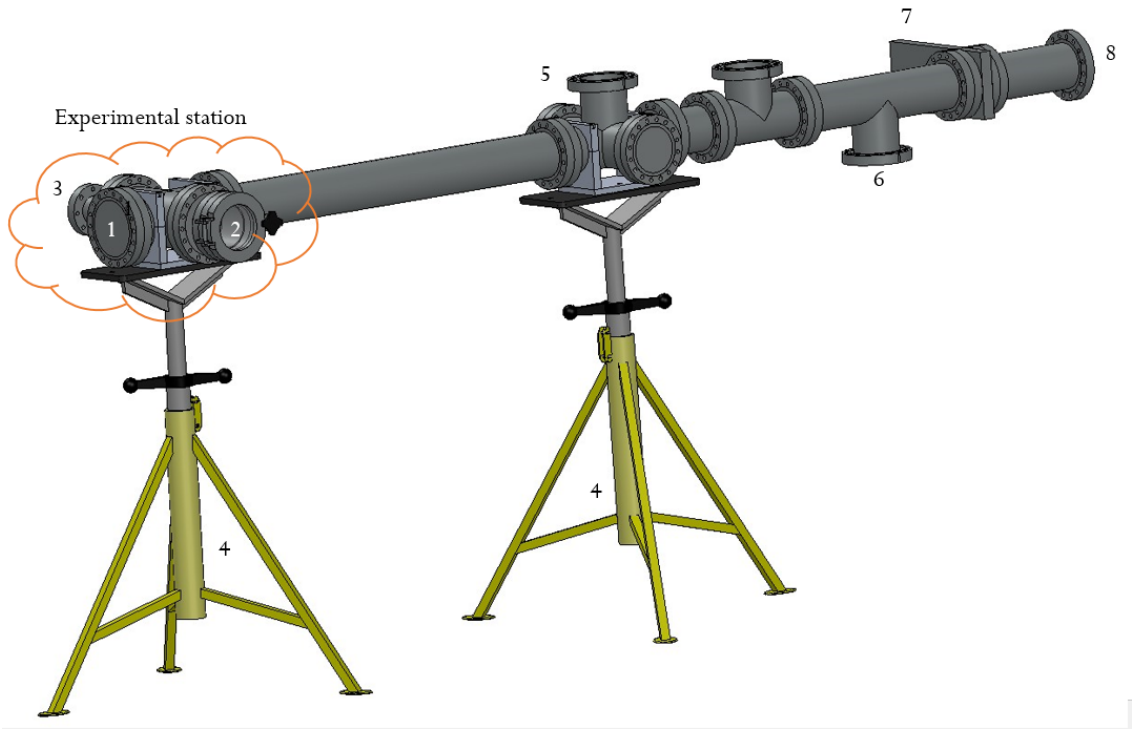

Figure 5-4: High-energy beamline configuration ("high-energy" side of pelletron); in the experimental station (left), 1 represents the sample holder (end flange), 2 represents the fast-access door, 3 represents the position for "wobble stick", then 4 represents the beamline stands, 5 represents the beam profile station, 6 is the turbo-pump chamber, 7 is the beam-stop valve and 8 is the pelletron accelerating tank exit.:

The experimental station that is located at the left end of the beamline configuration in Figure 5-4 is composed of a four-way 6 ¾-inch standard cross, widely used for high-vacuum systems. In Figure 5-4, the end flange, the fast-access door and the "wobble stick", are labeled as 1, 2 and 3, correspondingly, and they served as the main components of the experimental station, leaving the front end of the four-way cross open

for the beam path. The components of the experimental station of the high-energy beamline configuration are discussed in the following paragraphs.

The end flange discussed in the following paragraph will be noted as part of the setup "A". The end flange was designed and constructed to fit a single sample. As depicted in Figure 5-5, a 6 ¾-inch blank flange with a 2-inch center hole was placed at the end of the four-way cross that was intercepting the beam. The center hole was sealed with a 2 x 2-inch copper plate that served both as a sample holder and a heatsink. The sample was mounted onto the copper plate via two thumb screws (Figure 5-5, right). The copper plate is electrically insulated from the beam line using a rubber gasket. Electrical connections were made to the plate and beam line to allow the beam current to be directly measured using a picoammeter.

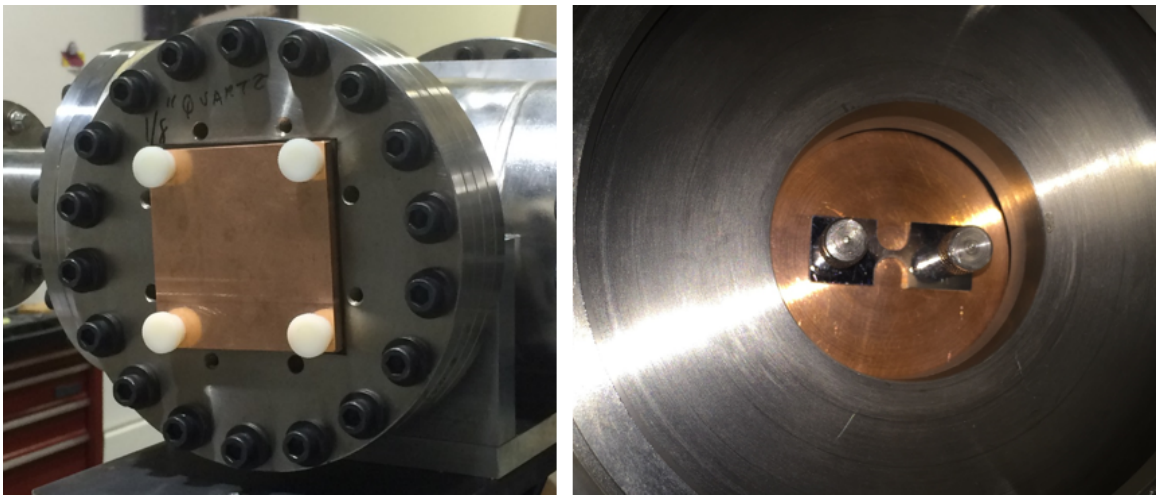

Figure 5-5: Photographs of setup "A" end flange; the outside of the sample holder (left) and inside the beamline with a sample mounted onto the copper plate (right).

A 6-inch fast-access door was installed on one of the four-way cross ends perpendicular to the beam path. An adaptor nipple was used to compensate for the

different flange sizes of the fast-access door and the four-way end. The purpose of the fast-access door is to provide convenient and fast loading of the samples in and out of the sample chamber. This door is equipped with a viewport window and a manual knob locking mechanism, Figure 5-6.

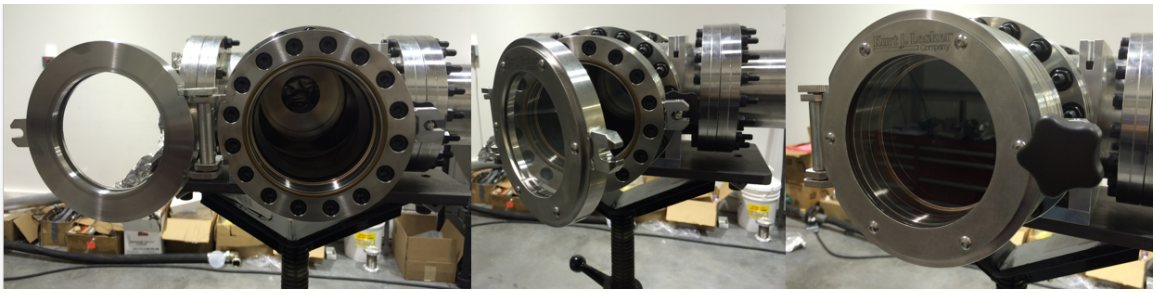

Figure 5-6: Photographs of the fast-access door installed on the four-way cross of the beamline setup.

The other perpendicular end of the four-way cross is equipped with a "wobble stick". The "wobble stick" is a tool that allows movement within a vacuum chamber. It is typically accompanied by a gripper or pincer for sample handling [138]. The "wobble stick" flange size differed from the four-way end size by 2 ¾ inches; therefore, installment required the use of an adaptor nipple, similar as the one connecting the fast-access door and the four-way.

In the experimental setup the "wobble stick" is employed to move a scintillator screen in and out of the beamline along one plane via an air-driven actuator system. The zinc oxide scintillator screen was installed on the "wobble stick" at a 45 degree angle using spring clips connected to a milled block of aluminum. The scintillator screen is used to visualize the beam size and intensity. Scintillator screens are made out of

materials that emit light through a fluorescence process through which ionizing radiation is converted into light when they come into contact with charged particles. In this case high-energy protons. These materials absorb the energy of the charged particles and emit it in the form of light. Figure 5-7 shows the "wobble stick" with the zinc oxide scintillator attached inside the experimental chamber.

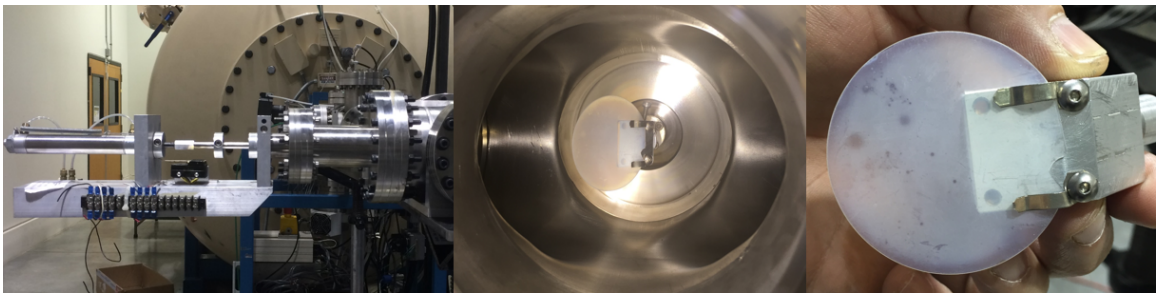

Figure 5-7: Photographs of the "wobble stick" (left), the scintillator attached to the "wobble stick" (middle and left).

Very few experiments were performed using setup "A" for a number of reasons. First, after the pelletron beam was tuned to maximize the output current at a range of energies between 1 and 2 MeV, the zinc oxide scintillator attached to the "wobble stick" was used to visualize the beam (Figure 5-10 shows the illuminated zinc oxide scintillator). The high-energy beam destroyed the scintillator disk after a few minutes of irradiation; however, these attempts did provide some useful information about the beam geometry. Furthermore, two blank test steel samples (without *LightGauge* sensors) were irradiated up to 30 dpa total fluence at a range of energies between 1 and 2 MeV which corresponded to approximately 5 hours of irradiation (various current). However, the steel samples irradiated in this configuration (setup "B") became discolored, indicating that the surface of the sample was heated to an extent that the damage produced by the

irradiation would likely anneal completely before examination. Even though a limited amount of experiments were conducted using the above described experimental setup (without cooling), due to performed simulations and calculations in regards to the penetration depth of the irradiation particles in the sample, discussed in section 5.3.1 of this chapter, this experimental setup was abandoned.

In an attempt to prevent any significant sample heating due to high-energy proton irradiation, it was decided to add cooling to the initial experimental station, more specifically to the end flange (see setup "A"). This cooled experimental station is recognized as setup "B". Similar to the initial approach, the center hole of the end flange was sealed with a 5-inch round copper plate (½-inch thick) that featured accessories for cooling. The copper plate served both as a sample holder and a heatsink. The copper plate, as shown in Figure 5-8 (Page 81), included a 2-inch cylindrical piece that extended from the center of the flat copper plate.

The cylindrical piece on which a ¼-inch copper coil was wrapped in 6 turns served as a "cold-finger", depicted in Figure 5-9. Cold water from the main chiller of the pelletron was pumped through the copper tubing in order to cool the experimental station and the sample. The sample was mounted directly onto the copper plate to ensure direct thermal contact so that heat could be exchanged between the sample and the copper plate. A thermistor with a digital readout was placed on the copper plate for temperature monitoring. The experimental setup as well as the temperature reading was monitored from the pelletron control room via camera setup; a camera was positioned directly across from the fast-access door viewport window to monitor, for instance, the movement of the scintillator screen or the digital readout of the thermistor (which was placed on top

of fast-access door, see Figure 5-10). Monitoring was performed throughout the irradiations.

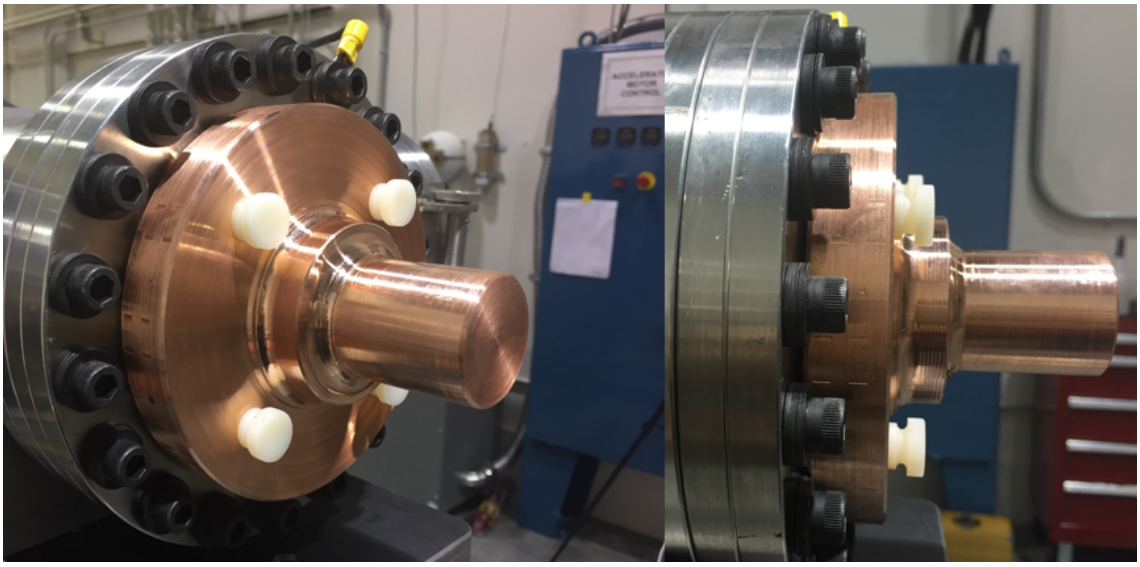

Figure 5-8: Photographs of the copper plate with the cylindrical piece (serving both as a sample holder and a heatsink) utilized in setup "B".

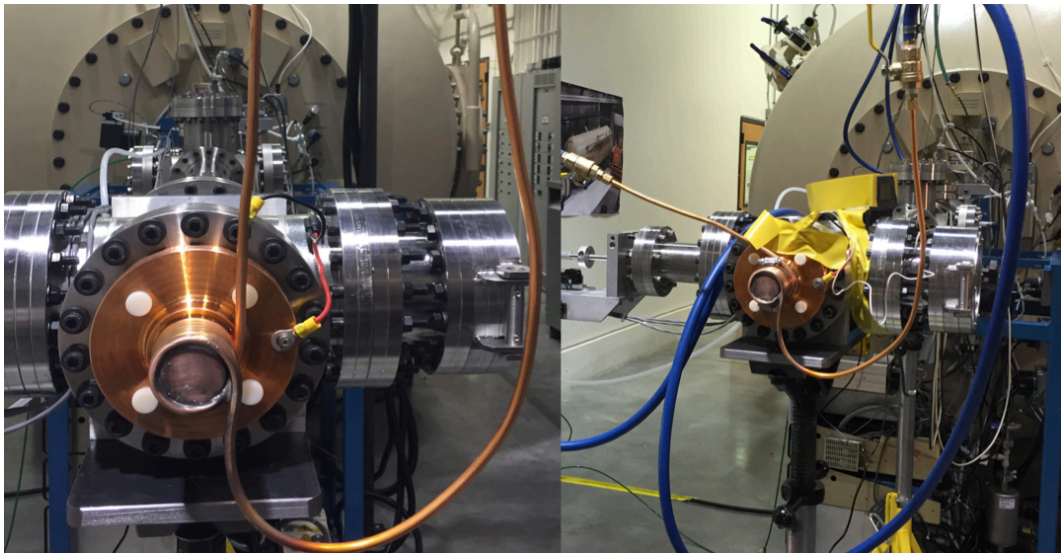

Figure 5-9: Photographs of setup "B" with cooling employed at the high-energy side of the pelletron; Representation of the "cold-finger" (cooling feature).

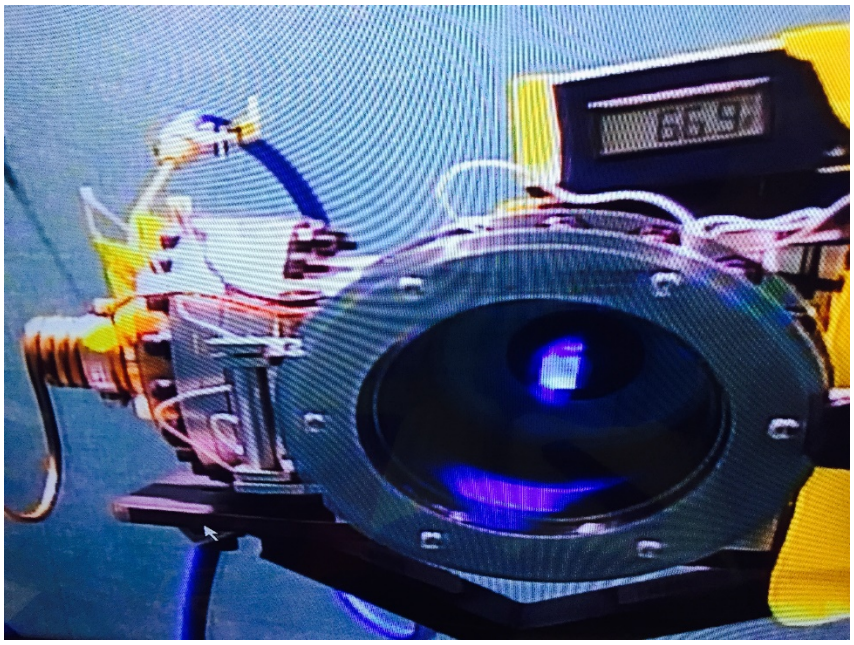

Figure 5-10: Photograph (seen from a camera) of setup "B" employed at the high-energy side of the pelletron in use, showing an illuminated zinc oxide scintillator at 1.5 MeV proton energy.

Another set of experiments were performed on test steel samples without a *LightGauge* sensor written on them using setup "B" (Figure 5-9). Similar to the first set of experiments the steel samples were subjected to a range of energies between 1 and 2 MeV to achieve a total fluence of 50 dpa. However, the steel samples irradiated with setup "B" did not show any discoloration due to the added cooling. The temperature throughout irradiation was monitored via the thermistor probe connected to the back of the heat sink; there was no observable change in temperature, which indicated that the irradiations were performed approximately at room temperature. The simulations performed (discussed in section 5.3.1) using setup "B" conditions indicated that the observed damage using these high energy protons was deeper than the depth of the

photonic sensors written on the samples. This led to the conclusion that in order to induce damage to the *LightGauge* sensors, the irradiation energy must be decreased.

In order to decrease the energy, the use of shielding foils in front of the sample was proposed to reduce the depth of the Bragg peak. This was attempted by wrapping the sample in aluminum foil. Upon irradiation, the foil promptly melted in the beam. This approach was abandoned and it was decided that the lower-energy particles directly from the pelletron source would be used instead. This decision was based on the fact that is not necessary to accelerate the protons to high energy only to slow them down to reduce the depth of the damage. The lower energy ions produced the damage depth desired for this project. The depth of the damage in the target and the ion energy required for irradiation are discussed in section 5.3.1 of this chapter.

5.2.2 Low-energy Beamline Configuration

As mentioned in the previous section, the intention was to produce damage at the desired region/depth of the samples i.e. the *LightGauge* sensors. To accomplish that, irradiation with lower energy ions was required. Therefore, the so called "low-energy" side of the pelletron (before the accelerating tank) was used. The low-energy side of the pelletron involved irradiation with negative hydrogen ions instead of protons at the high-energy side. This experimental setup entailed removing one of the quadrupoles (right before the accelerating tank) and replacing it with an experimental end flange. Similar to the high-energy beamline configuration, the low-energy beamline configuration employed two designs for the experimental flange; one with a scintillator (named setup "C") and one with cooling accessories (named setup "D").

Setup “C” was composed of an 8-inch blank flange with a 2-inch center hole for sample placement. To accommodate for this design, the beamline was sealed with a zinc oxide scintillator, a ¼-inch-thick quartz window and a hollow aluminum plate, as observed in Figure 5-11. This was done in an attempt to obtain the beam shape and consistency at the low-energy side of the pelletron, similar to the high-energy beamline setups, “A” and “B”.

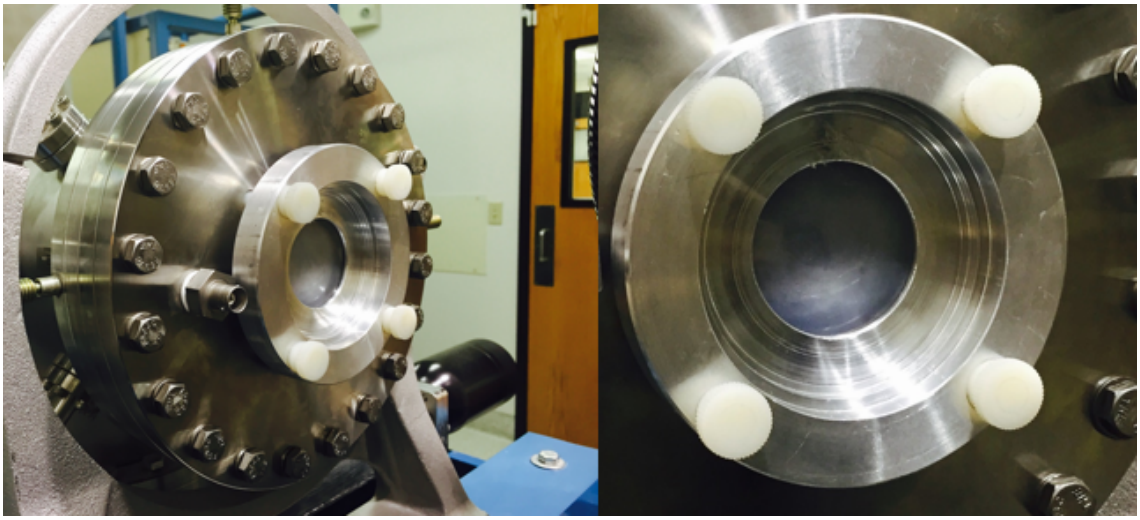

Figure 5-11: Photographs of setup “C” employed at the low-energy side of the pelletron.

This experimental setup (setup “C”) was tested by employing an ion beam of 53 keV and a current of 400 μA; however, both the scintillator and the quartz window fractured within 20 seconds of irradiation due to the heat produced by radiation and the inability to transfer that heat rapidly (setup “C” did not employ any cooling). Therefore, this design was discarded. Figure 5-12 shows three photographs of the illuminated scintillator during the irradiation and the splintered quartz disk.

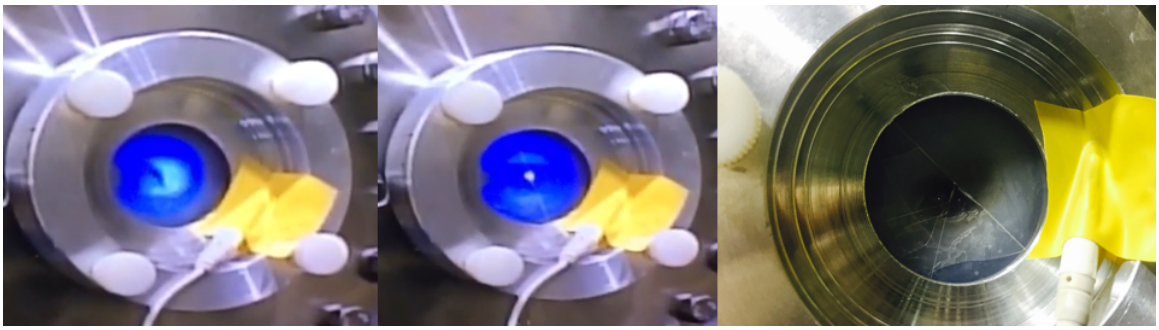

Figure 5-12: Photographs of: the illuminated zinc oxide scintillator employed in setup "C" at the low-energy side of the pelletron (left), rupturing the scintillator (middle) and the fractured scintillator and quartz window.

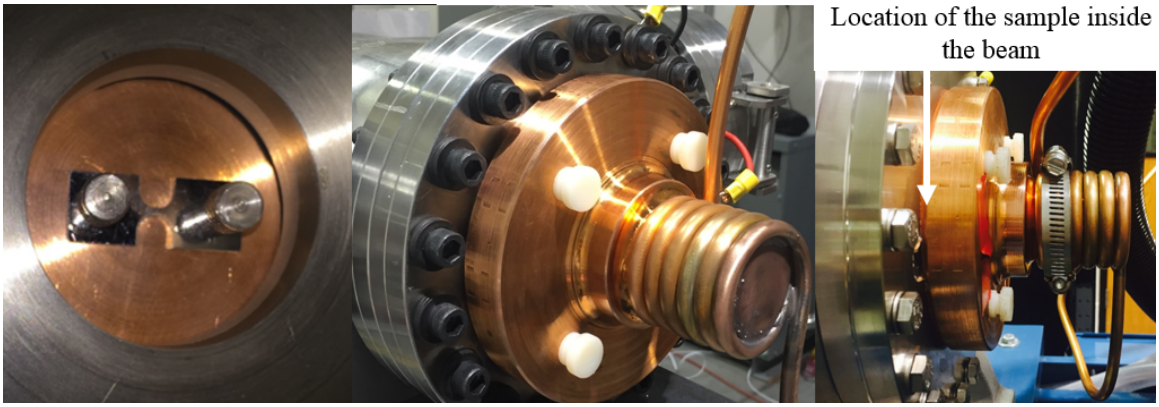

Figure 5-13: Photographs of the final experimental station (setup "D") employed at the low-energy side of the pelletron; Mounted sample on the copper plate sample holder inside the beamline (left), cooling station employed at the "low-energy" side of the pelletron (middle and left).

Consequently, the fourth and final setup (setup "D") that was designed and constructed at the low-energy side of the pelletron was ultimately utilized to perform all of the experiments (Figure 5-13). The final setup was a combination of the setup "B" and setup "C" such that it utilized the cooling station from setup "B" and the geometry of

setup “C”. The same thermistor from setup “B” was used to monitor the temperature. With the mounted copper cooling station, the temperature was never observed to go over 35 °C. While this temperature is above standard room temperature, it is still well below the threshold for temperature-induced changes in the sample.

5.3 Experiments

Ion beam irradiation is a valuable practice for fast assessment of nuclear structural materials radiation stability under neutron and gamma irradiation [44]. Radiation-induced damage in materials is measured by the number of displacements per atom, defined in the ASTM E521 [4] Standard Practice for Neutron Radiation Damage Simulation by Charged-particle Irradiation. The unit dpa has been discussed in details in section 2.3 of Chapter 2. The quantification of displacements per atom is a complex radiation transport problem normally resolved by Monte Carlo based codes such as the SRIM package discussed below.

5.3.1 SRIM/TRIM Simulations

The SRIM (Stopping and Range of Ions in Matter) software is a compilation of programs that calculates the ion penetration of a material through statistical simulations of ion-atom collisions. These simulations provide quantum mechanical approximations of Coulomb collisions, long-range interactions, and the charge state of each ion as it passes through a target. The TRIM (Transport of Ions in Matter) code is part of the SRIM package that simulates depth profiles of irradiation induced target damage using binary collisions approximation (BCA) method [55]. The software has very easy-to-use user

interface, built-in parameters for all ions and materials. User inputs, shown in Figure 5-14 (specifically for a steel sample), for TRIM include ion charge, name, mass, energy (10 eV - 2 GeV), angle of incidence, as well as a target description. TRIM outputs include the final ion distribution within the target, the total energy loss distribution, information on the electronic excitation of the material, and lattice displacements (target damage). This software was initially developed in 1983 by Ziegler and Biersack and is publicly available [139].

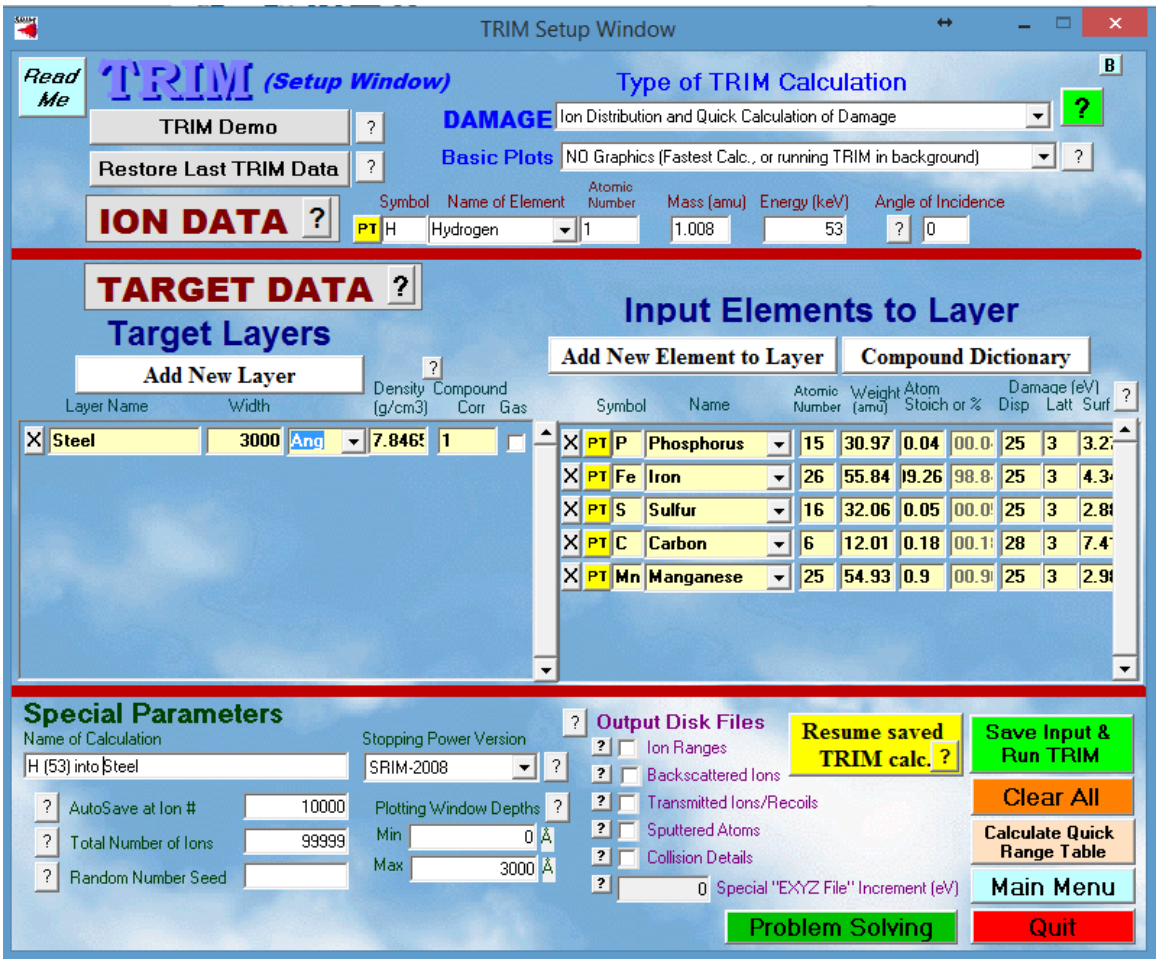

Figure 5-14: Typical TRIM setup window for a steel sample.

For this research, SRIM was used to calculate the range of Hydrogen ions in the materials of interest and TRIM was used to gain knowledge about the changes (displacements per atom) to the target (steel or zircaloy-4 samples) under bombardment with hydrogen ions. Since TRIM provides significant information concerning the penetration depth of the ions into the material, can therefore be used for investigations of the target damage.

TRIM offers two types of damage: ion distribution and quick calculation of damage and detailed calculation with full damage cascades. Both options provide a calculation of the final distribution of ions in the target and ion energy loss by the target, backscattered and transmitted ions; however, a twofold difference appears between the profiles calculated with "quick damage" and "full cascade" damage. This issue has been thoroughly discussed [140] with conclusions such as when TRIM is used for ion irradiation of nuclear materials, the preferred simulation option is "quick damage" since its results can be compared with the "NRT-dpa standard" [4] calculations. The NRT-dpa standard was developed by Norget, Torrens and Robinson, the source of its moniker, in 1975 to estimate the number of Frenkel pairs formed for a given energy transferred to the primary knock-on atom [141]. This method is incorporated in the ASTM E521 [4] and it is a suitable option to estimate the actual damage in irradiated materials, for typical nuclear reactor applications. The initial model for displacement damage (Equation 5-1) is expressed by Kinchin and Pease [142] as:

Equation 5-1

$$N_d = 0 \ \rightarrow T < E_d$$

$$N_d = 1 \rightarrow E_d \leq T < 2E_d$$

$$N_d = \frac{\beta\, T}{2E_d} \rightarrow T < E_d$$

Where:

N_d number of displaced atoms produced by a recoil atom of energy E with damage energy T

T damage energy

E_d minimum energy required to create a stable Frankel pair, 40 eV

β the factor was determined from binary collision models to account for realistic scattering, 0.8

5.3.2 Optimization of irradiation conditions

Prior to irradiation of the samples, the first prerequisite was to find the energy required to deliver damage to the target at a given depth. Since the pelletron source was used to induce the damage in the samples, hydrogen ion was used as an ion of interest. Before irradiation energy selection, SRIM was used to generate tables on ion stopping and range data of hydrogen into both steel and zircaloy-4 samples.

Table 5-1 (Page 91) shows the projected range of hydrogen into steel and zircaloy-4 over various energies. Since the *LightGauge* sensors fabricated on the materials of interest were approximately 300 nm deep, it is observed that the suitable ion energy range varied from 10 to 60 keV.

Figure 5-15 (Page 91) shows the projected range of hydrogen versus the ion energy; it is apparent that hydrogen has a very similar range in both steel and zircaloy-4. The data for this plot was obtained from the stopping and range tables included in the SRIM package and it was customized for the specific materials used.

Table 5-1: Projected range in steel and Zircaloy of hydrogen ion for different energies; projected range in red represents the desired range for hydrogen bombardment.

Ion Energy (keV)	25	27.5	30	32.5	35	37.5	40	45	50	55	60
Projected Range (nm) in Steel	152.4	164.7	176.7	188.3	199.8	211	222	243.6	264.7	285.3	305.6
Projected Range (nm) in Zircaloy	170.1	184.8	199.2	213.5	227.5	241.4	255.1	272.3	293.4	309	361.4

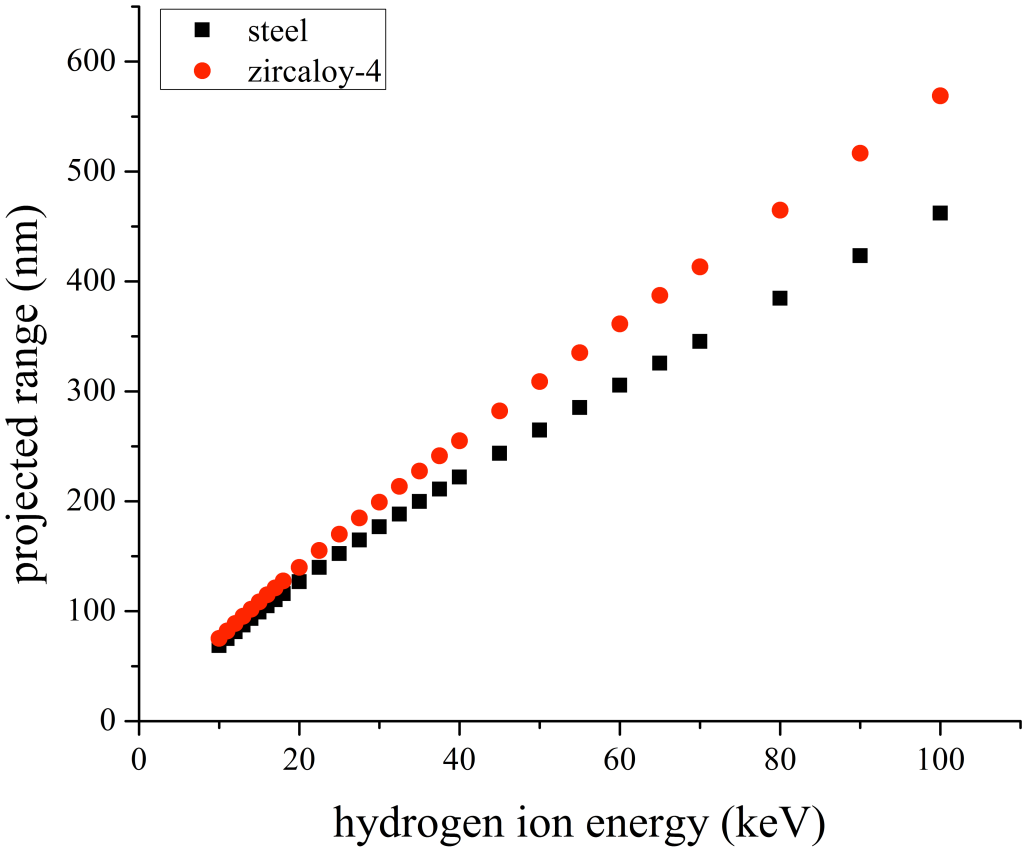

Figure 5-15: Projected range of hydrogen in the materials of interest (steel and zircaloy-4) as a function of the ion energy.

After obtaining data for the ion energy, TRIM was used to simulate the displacements per ion in the materials of interest with respect to their depth. Angstrom (Å) is the most common unit of depth used by TRIM in assessing target microscopic damage; 1 angstrom is equal to 10^{-10} meters or 0.1 nanometers [55]. Multiple sets of simulations were conducted for this research. They are described in the following paragraphs. All of the simulations were run in the quick calculation of damage mode for 100,000 particle histories. An example of typical plots of particle trajectories can be seen in Figure 5-16; the depth plot represents the ion concentration around a depth of 3500

angstroms, which corresponds to 350 nm and the transverse view shows a head-on view of the steel sample.

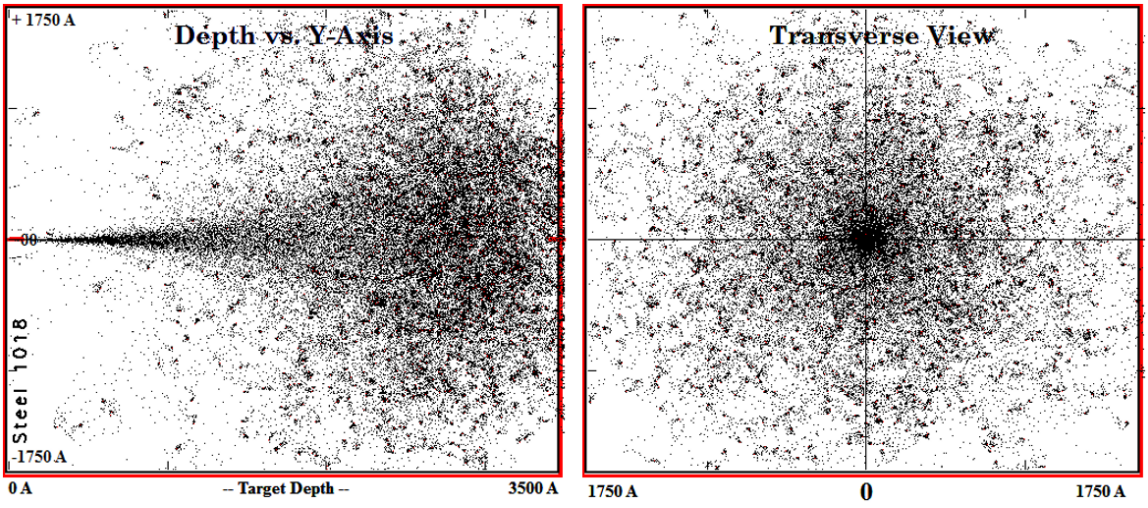

Figure 5-16: TRIM simulation; particle trajectory plots of 53 keV hydrogen into steel sample. Depth plot (left) depicts the ion concentration around 3000 angstroms and the transverse view (right) shows a head-on view of the steel sample.

The first set of simulations was conducted for higher hydrogen energy range (between 1 MeV and 3 MeV) in the materials of interest; however, the outcome suggested shielding the samples with another material since the projected range of hydrogen into the samples was in the micrometer range (between 6 µm and 35 µm) rather than in the nanometer range, and the photonic crystal was approximately 300 nm deep.

In spite of this, the second set of simulations was performed using various thicknesses of shielding materials, such as thin foils (approximately 20 µm to 150 µm thickness depending on the material used and the penetration depth of hydrogen into the material) of molybdenum, titanium and aluminum. These simulations demonstrated

desired ion implantation in the actual photonic crystal sensor, though that would have been achieved with irradiations at higher energies with the shielding in place. Such irradiations would have produced unwanted neutrons since the proton energy was above the threshold energy for (p, n) reactions. At the time, the experimental setup was not suited for neutron production while irradiating for extended times, therefore it was decided to irradiate at low energies without shielding.

Another issue with using shielding materials is range straggling (spread of ion distribution). Range straggling results from statistical energy loss processes throughout the range of impacting ions (it is basically a deviation of the projected range). This option would have spread the irradiation damage over a larger depth due to the flattening of the Bragg peak. The lower displacements per atom would have significantly lengthened irradiation times.

As discussed in Chapter 2, the peak in the Bragg curve is caused by increased cross section for interaction as a particle slows down. When a charged particle travels through matter, it ionizes atoms of the material and deposits energy along its path. As the particle slows down along the path, its probability of interaction increases. This peak is apparent in all of the future figures and it represents the depth of maximum damage concentration in the material.

The third set of simulations was performed using multiple energies of hydrogen that belonged to the lower energy range (10 keV, 20 keV, 30 keV, 40 keV and 53 keV). The damage-depth profiles are presented in Figure 5-17 and Figure 5-18. Both plots show

the Bragg peak for each energy and it is evident that those particular energies cover the depth of the photonic crystal in steel (Figure 5-17) and zircaloy-4 (Figure 5-18).

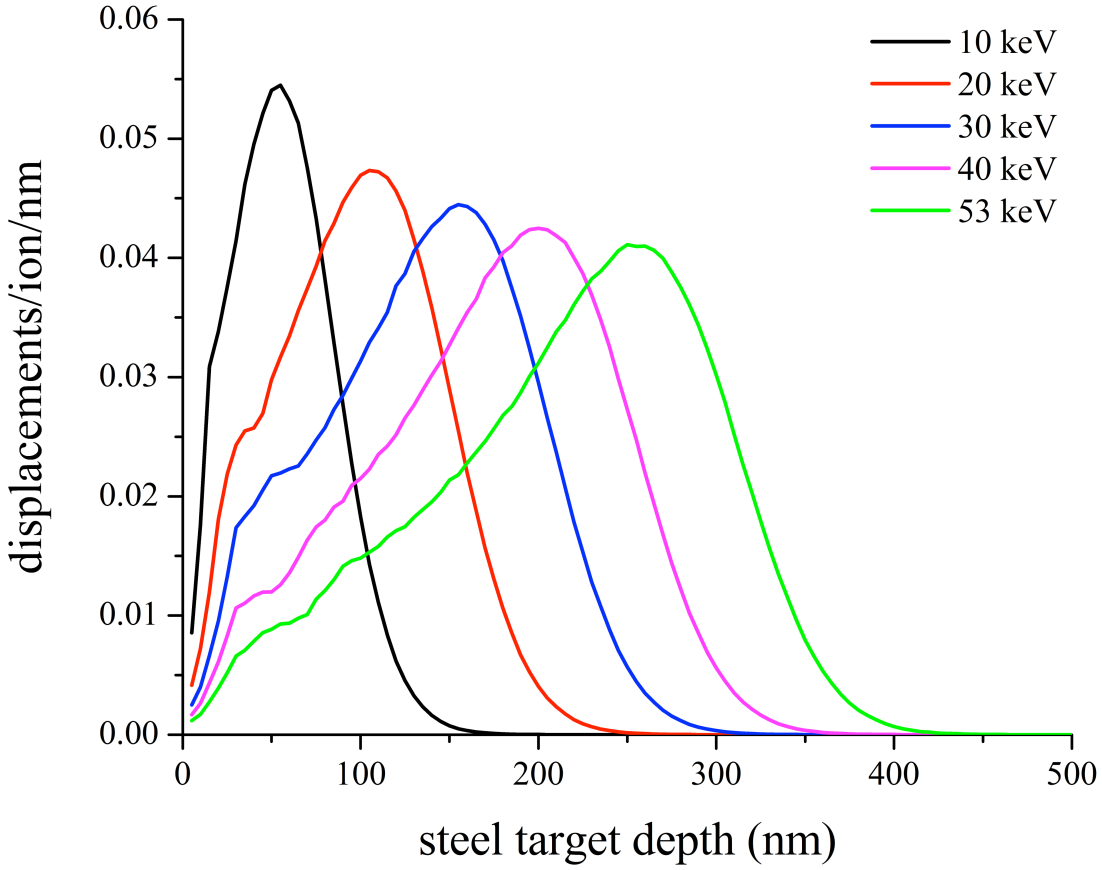

Figure 5-17: Damage-depth profile for steel; displacements/ion/nm as a function of depth for various hydrogen energies.

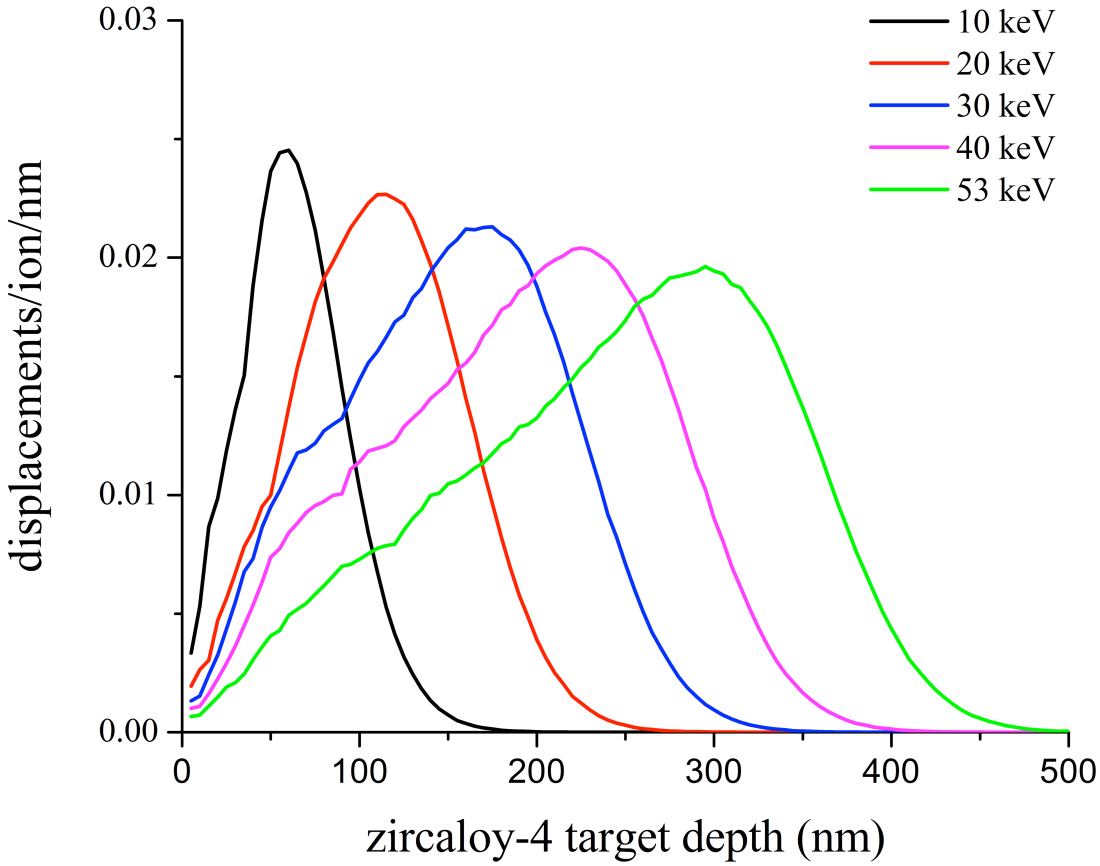

Figure 5-18: Damage-depth profile for zircaloy-4; displacements/ion/nm as a function of depth for various hydrogen energies.

The energy 53 keV was chosen for the reason that initially the ion source of the pelletron was tuned and optimized for that energy to maximize the beam current. Since it belonged to the range of energies that satisfied the damage profile for the materials of interest and their depth, it was the ideal energy to use rather than changing the ion source settings and optimizing it for a new energy. The damage profiles for steel and Zircaloy samples are shown in Figure 5-19.

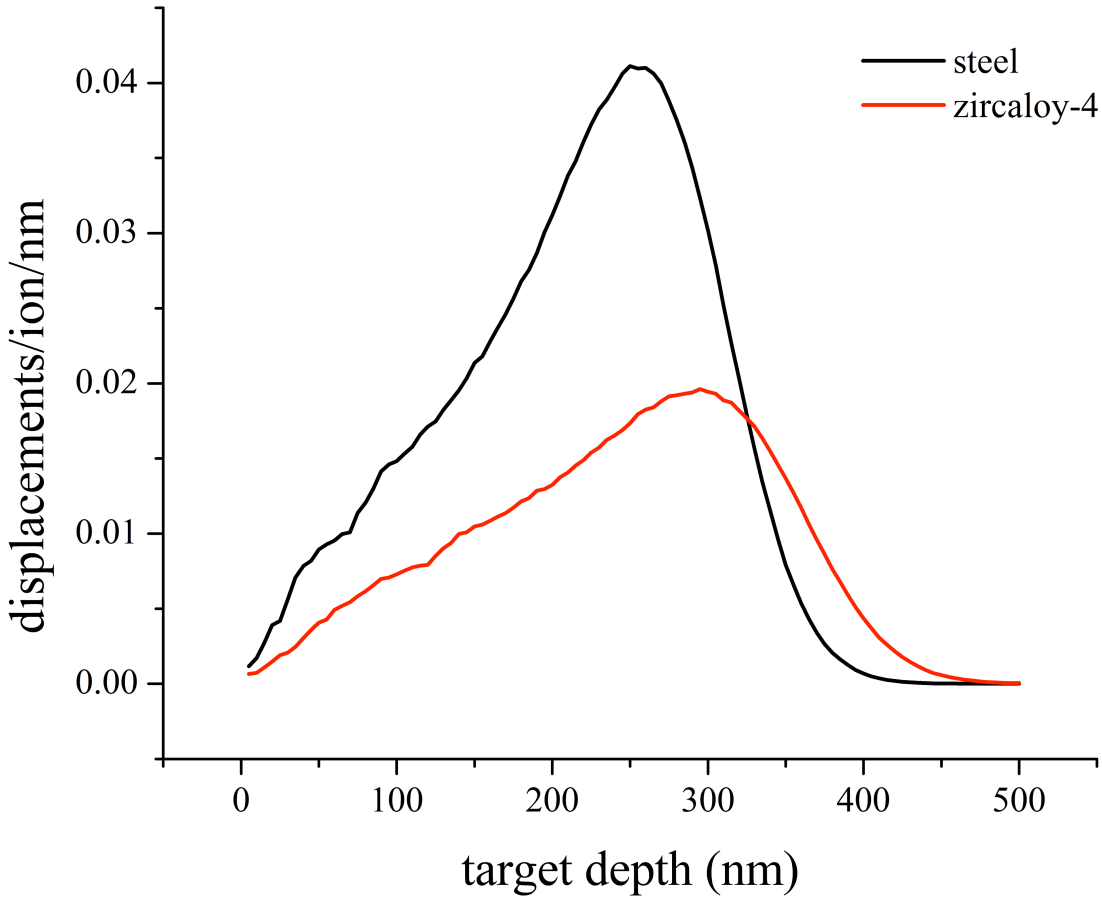

Figure 5-19: Damage-depth profiles for steel (black) and zircaloy-4 (red); displacements/ion/nm as a function of depth for 53 keV.

The information from the damage profile in Figure 5-19 (black plot) shows that the most damage (displacements/ion/nm) in steel occurs between 210 and 260 nm. Similarly, the zircaloy-4 sample's damage is depicted in Figure 5-19 (red plot); the most damage occurs between 270 and 320 nm.

The calculations of the irradiation time and the total fluence were based on the TRIM data. TRIM outputs the displacements per ion per angstrom over the depth of the target material and the mass density of the target material. The following equations summarize the calculation for number density of the materials of interest (Equation 5-2),

the irradiation ion flux (Equation 5-3), the displacement per atom rate (Equation 5-4) and the irradiation time for the desired fluence (Equation 5-5).

Equation 5-2

$$n = \frac{N_A \times \rho}{M}$$

Where:

n number density of the target material, atoms/cm^3
N_A Avogadro's number, 6.023 x 10^{23} mol^{-1}
ρ mass density of the target material, g/cm^3
M molar mass of the target material, g/mol

Equation 5-3

$$q = I \times t \qquad \& \qquad I = \frac{q}{t}$$

Where:

q total electric charge of the negative hydrogen ions, C (coulomb)
I ion current, A (ampere)
t time, sec (seconds)

As mentioned is section 5.1.3, the electric charge of a proton or an electron is positive or negative 1.602 × 10^{-19} coulombs; so is the case with positive and negative ions, they carry the same elementary charge. A coulomb is the number of electric charges

per ampere flowing past given point (Equation 5.3) [143]. For the purpose of this research, negative hydrogen ions move in vacuum of the pelletron and carry the electric charge of 1.602×10^{-19} coulombs.

Equation 5-4

$$1\,A = \frac{1\,{}^{C}/_{sec}}{1.602\times10^{-19}\,C} = 6.25\times10^{18}\ {}^{ions}/_{sec}$$

From Equation 5-4, an ion current of 1 μA is equivalent to 6.25 x 10^{12} ions/sec, which is the case for the 1 μA of ion beam current of the low energy side of the pelletron. On the other hand, the ion flux is the ion beam current per unit area; the area of the pelletron ion beam is approximately 5 cm^2, which makes the ion flux equal to 1.23 x 10^{12} ions/sec/cm^2 for 1 μA.

Equation 5.5 represents the dpa rate per microampere calculation. The data for the displacements/ion/angstrom was obtained from TRIM (the highest value of the Bragg peak was used for the calculations), the ion flux was calculated from Equation 5.4 and the number density was calculated from Equation 5-2. Table 5-2 shows calculated values of the above-mentioned parameters.

Equation 5-5

$$\frac{{}^{dpa}/_{sec}}{\mu A} = \frac{\frac{dpi}{\text{Å}} \times \frac{ions}{sec\ \cdot\ cm^2} \times \frac{1\,\text{Å}}{10^{-8}cm}}{\frac{atoms}{cm^3}}$$

Where:

dpa/sec/μA	rate of displacements per atom for 1 μA of current
dpi/Å	displacements per ion per angstrom
ions/sec/cm^2	ion flux of the pelletron source
atoms/cm^3	number density for the materials of interest

Table 5-2: Materials of interest based calculations of number density, displacements/ion/angstrom and displacements/second/microampere.

Sample	Number Density	Displacements/ion/Å	dpa/sec/μA
zircaloy-4	4.29E+22	1.95E-03	5.62E-06
steel	8.48E+22	4.07E-03	5.92E-06

Equation 5-6

$$dpa = \frac{dpa/_{sec}}{\mu A} \times I \times t$$

Where:

dpa/sec/μA	rate of displacements per atom for 1 μA of current
dpa	total fluence
I	irradiation beam current
t	irradiation time

Equation 5-6 calculates the total displacements per atom. These calculations are shown in Table 5-3 for the steel samples and Table 5-4 for the zircaloy-4 samples.

In summary, the irradiation conditions were set in favor of minimizing the time of irradiation and of maximizing the total fluence.

- Since the penetration depth of the hydrogen ions is in the range of few micrometer when passing through metals and in order to irradiate and damage the materials of interest with the incorporated *LightGauge* sensors directly, the energy of the hydrogen ions had to stay in the low range (53 keV).

- In order to simulate in-pile irradiation, the bombardment of hydrogen ions was carried out under a zero degree angle of incidence between the ion beam and the sample. This means that the sample was positioned to be perpendicular to the ion beam.

- The irradiation temperature was kept below 100 ˚C, in order to study radiation effects in the materials of interest independently of temperature. Especially for the steel samples, the irradiation temperature was kept below the iron phase transition temperature (eutectoid temperature = 727 ˚C [68]). The temperature was kept as low as possible to minimize annealing that can happen at much lower temperatures than the eutectoid temperature.

- The irradiation time varied between 15 minutes and 5 hours, mainly depending on the desired fluence and ion beam current.

- All irradiations were carried out under a high vacuum (1.0×10^{-7} to 1.0×10^{-9} torr). Prior to starting the accelerator, all components were properly cleaned with methanol and acetone to prevent surface contamination.

As described in Chapter 4, there were two rectangular type samples that were subjected to ion beam irradiation, one steel and one zircaloy-4 sample. Each sample had

six sensors and each sensor served as an individual sample for every irradiation; thus after every irradiation a TEM lamella was removed out of a sensor for further characterization, hence that particular sensor was no longer existent for the following irradiations. Having multiple sensors on one sample made the irradiations easier as all of the sensors were irradiated at the same time, and furthermore with additional irradiations the total dose could be calculated as the accumulation of the previous doses from each individual irradiation.

The ion fluences that the samples were subjected to were 1, 5, 10, 20, 50 and 100 dpa, which cover the common damage levels for reactor materials. Tables 5-3 (for steel) and 5-4 (for Zircaloy) systematically show the irradiation time of the samples, the current measured by the pelletron low energy Faraday cup, the dpa rate and the total fluence reached.

Table 5-3: Hydrogen ion irradiation of steel, performed at the RISE pelletron.

Sample - Steel 02-002-00002 - dpa/min/μA = 3.55E-04						
Date	**Irradiation Time (min)**	**FC Current (μA)**	**ions/s/cm^2**	**Dose rate @ highest peak (dpa/min)**	**Total Fluence (dpa)**	
5-Apr	2	105	1.294E+14	0.037	0.075	1.029
	7	155	1.911E+14	0.055	0.386	
	8	200	2.465E+14	0.071	0.569	
12-Apr	5	530	6.534E+14	0.188	0.942	5.035
	6	420	5.178E+14	0.149	0.896	
	8	200	2.465E+14	0.071	0.569	
	9	500	6.164E+14	0.178	1.600	
15-Apr	5	700	8.629E+14	0.249	1.244	10.025
	10	680	8.383E+14	0.242	2.417	
	5	630	7.766E+14	0.224	1.120	
	1	590	7.273E+14	0.210	0.210	
19-Apr	6	720	8.876E+14	0.256	1.536	20.038
	10	690	8.506E+14	0.245	2.453	
	15	650	8.013E+14	0.231	3.466	
	12	600	7.396E+14	0.213	2.559	
21-Apr	10	710	8.752E+14	0.252	2.524	50.305
	10	700	8.629E+14	0.249	2.488	
	10	600	7.396E+14	0.213	2.133	
	10	510	6.287E+14	0.181	1.813	
	15	480	5.917E+14	0.171	2.559	
	15	520	6.410E+14	0.185	2.772	
	10	500	6.164E+14	0.178	1.777	
	20	495	6.102E+14	0.176	3.519	
	30	465	5.732E+14	0.165	4.959	
	35	460	5.671E+14	0.164	5.723	
22-Apr	10	760	9.369E+14	0.270	2.701	100.263
	10	715	8.814E+14	0.254	2.541	
	10	690	8.506E+14	0.245	2.453	
	10	645	7.951E+14	0.229	2.293	
	10	555	6.842E+14	0.197	1.973	
	10	545	6.718E+14	0.194	1.937	
	10	525	6.472E+14	0.187	1.866	
	10	510	6.287E+14	0.181	1.813	
	10	500	6.164E+14	0.178	1.777	
	60	485	5.979E+14	0.172	10.344	
	120	475	5.856E+14	0.169	20.261	

Table 5-4: Hydrogen ion irradiation of zircaloy-4 sample, performed at the RISE pelletron.

Sample – Zircaloy-4 02-010-00002 - dpa/min/μA = 3.37E-04						
Date	**Irradiation Time (min)**	**FC Current (μA)**	**ions/s/cm^2**	**Dose rate @ highest peak (dpa/min)**	**Total fluence (dpa)**	
7-Apr	5	100	1.233E+14	0.034	0.168	1.044
	5	160	1.972E+14	0.054	0.270	
	9	200	2.465E+14	0.067	0.606	
12-Apr	10	610	7.520E+14	0.206	2.055	5.079
	5	600	7.396E+14	0.202	1.011	
	5	575	7.088E+14	0.194	0.969	
14-Apr	10	580	7.150E+14	0.195	1.954	10.083
	5	550	6.780E+14	0.185	0.927	
	5	500	6.164E+14	0.168	0.842	
	10	380	4.684E+14	0.128	1.280	
16-Apr	10	750	9.246E+14	0.253	2.527	20.460
	10	530	6.534E+14	0.179	1.786	
	10	400	4.931E+14	0.135	1.348	
	10	350	4.315E+14	0.118	1.179	
	35	300	3.698E+14	0.101	3.538	
17-Apr	15	650	8.013E+14	0.219	3.285	50.203
	10	550	6.780E+14	0.185	1.853	
	10	510	6.287E+14	0.172	1.718	
	85	505	6.225E+14	0.170	14.463	
	50	500	6.164E+14	0.168	8.423	
20-Apr	15	785	9.677E+14	0.264	3.967	100.465
	10	765	9.430E+14	0.258	2.578	
	10	730	8.999E+14	0.246	2.460	
	10	665	8.198E+14	0.224	2.241	
	10	640	7.890E+14	0.216	2.156	
	10	500	6.164E+14	0.168	1.685	
	20	450	5.547E+14	0.152	3.032	
	25	495	6.102E+14	0.167	4.170	
	20	455	5.609E+14	0.153	3.066	
21-Apr	35	660	8.136E+14	0.222	7.783	
	10	620	7.643E+14	0.209	2.089	
	15	600	7.396E+14	0.202	3.032	
	15	550	6.780E+14	0.185	2.780	
	15	525	6.472E+14	0.177	2.653	
	25	510	6.287E+14	0.172	4.296	
	15	450	5.547E+14	0.152	2.274	

5.4 Maryland University Training Reactor (MUTR)

The Maryland University Training Reactor (MUTR) is an open pool TRIGA (Training, Research, Isotopes, General Atomic) reactor with a maximum licensed steady state and thermal power of 250 kW. TRIGA is a type of small training reactor designed and manufactured by General Atomics. At present, the reactor is utilized as a source of neutrons for mixed field neutron and gamma radiation studies on the effects of radiation on materials.

The reactor is fueled with modified TRIGA fuel. The reactor core (Figure 5-20) consists of 93 fuel elements, 3 control elements and 1 instrumented element. The fuel elements are enriched to <20 weight % ^{235}U, and each of them contains a top and bottom slug of graphite which act as neutron reflectors. Additionally, two graphite reflector elements are positioned in the assembled core, adjacent to two of the outer fuel assemblies [144]. The TRIGA reactor can be considered to be “inherently safe”, because of its uranium zirconium hydride fuel (UZrH), which provides the highest degree of safety based on its unique physical properties.

The Maryland University Training Reactor has five experimental facilities: the through tube, two beam ports, the pneumatic transfer system (rabbit) and the thermal column. The placement, geometry and material composition of each facility determines the flux, energy and type of radiation present. A schematic of the core configuration and experimental facilities appears in Figure 5-20.

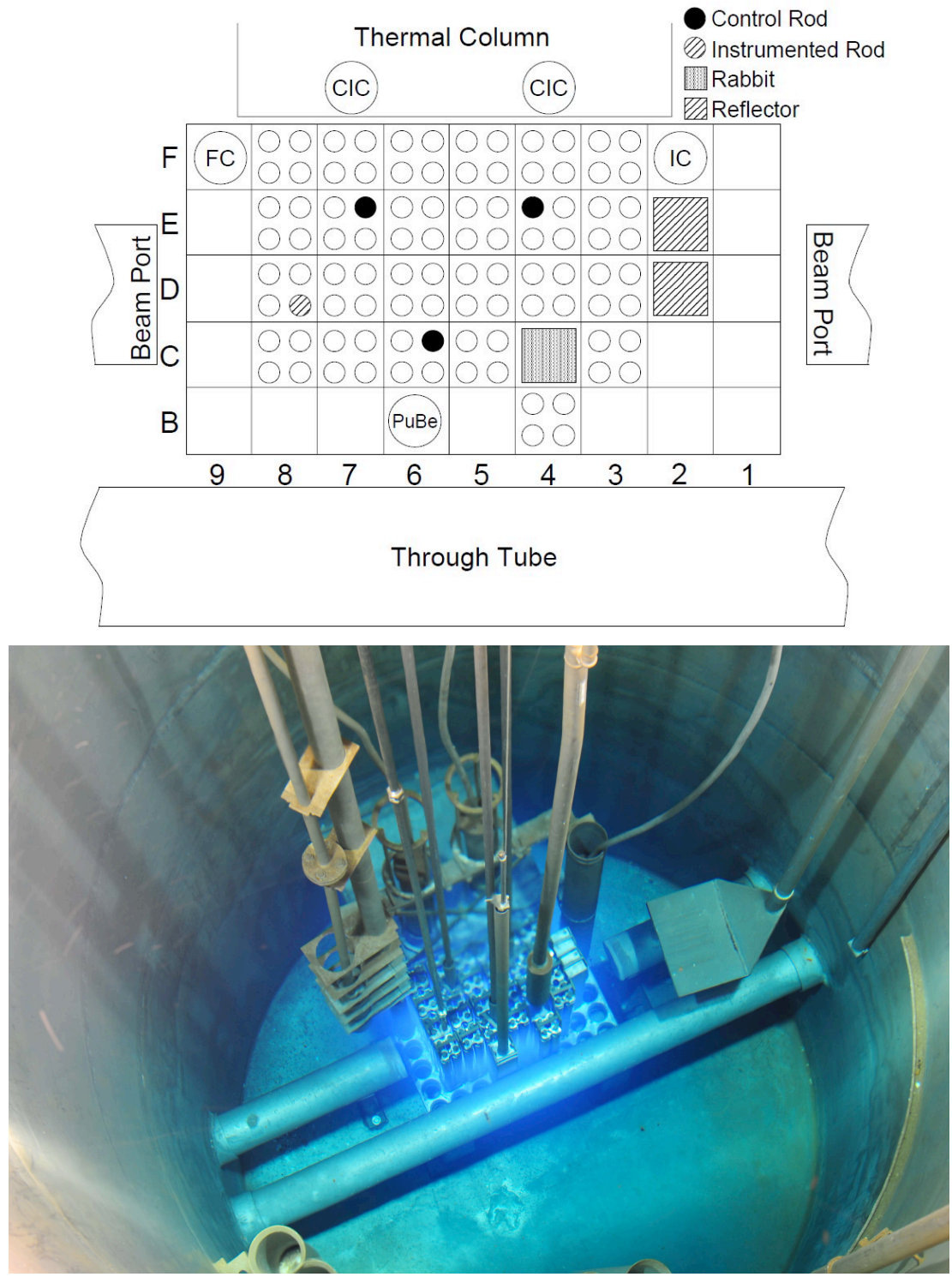

Figure 5-20: MUTR Top View of Reactor Core (top: schematic [144], bottom: actual photo).

5.4.1 Pneumatic Transfer System (Rabbit System)

The Maryland University Training Reactor is equipped with a CO_2–driven pneumatic ("rabbit") system designed for short neutron irradiations and rapid retrieval of samples. The system consists of the following components: a) the in-core experimental port (the terminal), c) the polyethylene transfer tube, c) the pneumatic transfer system and d) the hot room glove box. The sample of interest is contained in a sealed polyethylene ampule and placed inside the rabbit cylinder. The pneumatic system transfers the sample between the glove box (located in the hot room on the facility's west balcony) and the terminal (inside the reactor core). The terminal of the rabbit is located in the reactor core and is shown in the schematic of Figure 5-20, labeled as C4. The reactor operator controls the length of irradiation manually or automatically from the control room [144].

Rabbit systems are frequently used for Neutron Activation Analysis (NAA), for a technique used particularly for detecting and characterizing impurities in samples. Also, since the neutron flux in the core terminal (rabbit) is the highest that a sample can achieve in the MUTR (approximately 1.60×10^{10} neutrons/cm^2/sec/kW), the rabbit is also used to irradiate samples that need high total neutron flux (neutrons/cm^2) in a shorter amount of time than the other experimental facilities.

5.4.2 Neutron Flux Measurements

When considering the damage of materials due to irradiation with neutrons it is essential to know the magnitude of the neutron field. Further, to be able to compare work done at one facility versus another, standard techniques of flux measurements must be established. Such methods for measurement of neutron fluxes have been established by

ASTM E261 [145], Standard Practice for Determining Neutron Fluence, Fluence Rate, and Spectra by Radioactivation Techniques and ASTM E262 [146], Standard Test Method for Determining Thermal Neutron Reaction Rates and Thermal Neutron Fluence Rates by Radioactivation Techniques. In order to obtain a verification of the flux magnitude at the various penetrations of the Maryland University Training Reactor, foil activation analysis method was performed.

5.4.2.1 Definitions

Neutron Flux – A measure of the intensity of neutron radiation, determined by the rate of emission or transmission of neutrons per area; this is measured in neutrons/cm^2/sec [147].

Gamma Spectrum – the range of the most energetic part of the electromagnetic spectrum that can be emitted as a product of radioactive decay;

5.4.2.2 Neutron Activation Analysis and Theory

In order to carry out a full range of experimental work in a test reactor such as the MUTR, it is highly desirable to have standardized measurements of the neutron flux spectrum. In an effort to measure the neutron flux in a particular experimental facility, Neutron Activation Analysis can be used to reproducibly and accurately determine neutron flux spectrums. Neutron activation is a process in which neutrons induce radioactivity in materials that were not previously radioactive. This occurs when an incident neutron is absorbed ("captured") by the nucleus of a target atom, placing the

target atom in an excited state. The excited target nuclei then decay to a lower energy state, most often by the emission of a gamma ray or a beta particle. Ultimately, the neutron capture event produces unstable daughter products that exhibit various half-lives and particle emissions with various energies. Therefore, depending on the time of measurement NAA can be categorized as prompt gamma-ray neutron activation analysis (PGNAA) and delayed gamma-ray neutron activation analysis (DGNAA). In PGNAA the measurements take place during irradiation, where in DGNAA they follow a radioactive decay. Gamma spectroscopy is used to a) determine the atomic composition of an irradiated material or b) determine the flux incident on a material of known composition. Determination of the neutron flux from these measurements has been carried out in accordance with the American Society for Testing Materials (ASTM) standard methods [145], [146].

Activation foil detectors have large benefits over other detectors types through their small size, insensitivity to gamma radiation, low cost, and resistance to harsh environments. For these reasons, activation foils are extensively used in mapping neutron fluxes in reactor cores [53].

The purity of a material is very crucial in the selection of foils for activation. If the material is not pure, the neutron flux evaluation might provide false results due to presence of other neutron activation reactions. Based on the standard's recommendation, the foils should be activated in a desired location (typically the sample's position), and, after the irradiation, the induced activities of gamma rays should be measured using a High Purity Germanium Detector (HPGe).

The activation foils used to characterize the experimental facilities at the MUTR were chosen carefully to cover all neutron energy regions. Calculations involving cross sections, half-lives and gamma yields, as well as preliminary irradiations helped determine suitable irradiation times and power levels. All samples were irradiated in cadmium covers to minimize their activation by thermal neutrons. The activity per target nucleus at the time of counting was calculated for each sample using Equation 5-7.

Equation 5-7

$$A = \frac{CR}{\eta I}$$

Where:

A	activity at the time of counting (present activity)
CR	count rate (counts/sec)
η	HPGe detection efficiency (%)
I	intensity of the gamma ray (%)

The activity or number of decay gamma rays being emitted by a particular radionuclide is dependent on the disintegration rate, which is directly proportional to the neutron flux. By measuring the number of gamma rays from radioactive decay, the neutron flux can be calculated. Equation 5-8 describes the irradiation process.

Equation 5-8

$$A_0 = N\sigma\phi t_{irr}(1 - exp^{-\lambda t_{irr}})$$

Where:

A_0	activity produced for the radionuclide of interest (Bq)
N	number of target atoms in the sample
λ	decay constant (1/hr)
σ	cross section for the reaction that produces the radioisotope (cm^2)
t_{irr}	irradiation time (hr)
ϕ	neutron flux (neutrons/cm^2/sec)

After irradiation the radioactive atoms decay in at a rate that is determined from the decay equation below, where A_d is the activity of the isotope of interest after a decay time, t_{decay}.

Equation 5-9

$$A_d = A_0 exp^{-\lambda t_{decay}}$$

When a radioactive element decays, it gives off a characteristic peak of radiation that can be used to detect the radioactive isotope that is present in the sample. The activity of the activated parent nuclides created during irradiation is directly proportional to the neutron flux and the amount of stable elements present in the sample. The neutron flux magnitude for each foil was calculated by the following equation:

Equation 5-10

$$\phi = f\sigma N_A m \frac{A_0\, MW exp^{\lambda t_{decay}}}{1 - exp^{-\lambda t_{irr}}}$$

Where:

ϕ	neutron flux (neutrons/cm^2/sec)
f	natural abundance (%)
N_A	Avogadro's number (#/mol)
m	mass of the sample (g)
σ	cross section for the reaction that produces the radioisotope (cm^2)
A_0	activity produced for the radionuclide of interest (Bq)
MW	molecular weight (g/mol)
λ	decay constant (1/hr)
t_{decay}	decay time (hr)
t_{irr}	irradiation time (hr)

The experimental neutron flux data for the pneumatic transfer system (rabbit) shown in Table 5-5 is based on the above calculations.

Table 5-5: Radiation rates for the MUTR rabbit system [144]

Radiation Type	**Amount**	**Units**
Thermal Flux	1.60E+10	n/cm^2/sec/kW
Fast Flux	8.00E+09	
Gamma Dose Rate	1.90E+01	rad/sec/kW

5.5 MUTR Experimental Setup

As indicated in the introduction of this chapter, there was one experiment performed at the Maryland University Training Reactor. The sample subjected to a neutron-field irradiation using the pneumatic transfer system (rabbit) of the MUTR was a steel dog-bone sample that contained one *LightGauge* sensor as depicted in Figure 5-21. The *LightGauge* sensor was made out of 16 photonic crystals, 4 x 4 array (square lattice), and each containing 256 square pillars.

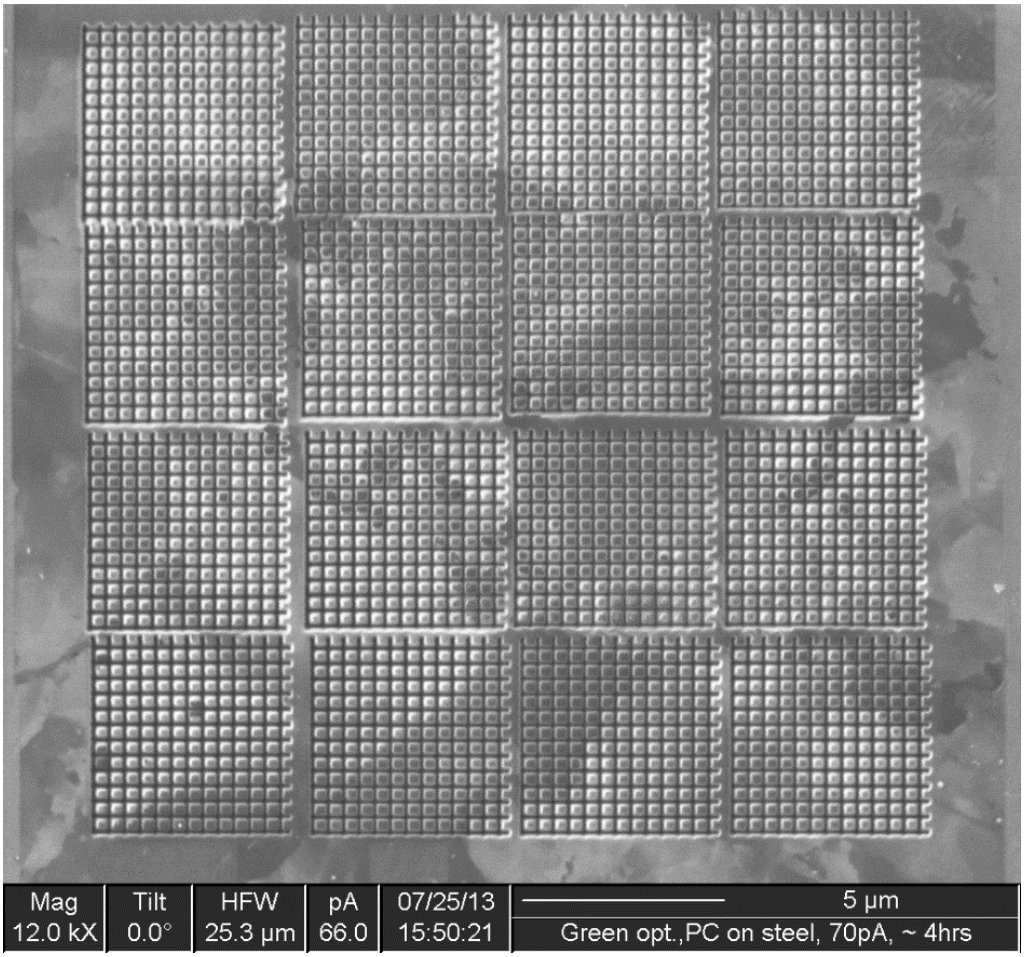

Figure 5-21: FIB micrograph; *LightGauge* sensor on steel dog-bone sample, 4 x 4 array square lattice.

Prior to irradiation, the sample and the sample container were cleaned using ethyl alcohol and acetone to remove and prevent any contamination. Following the sample preparation for irradiation, the sample was enclosed in a polyethylene container (Figure 5-22) inside the MUTR rabbit cylinder.

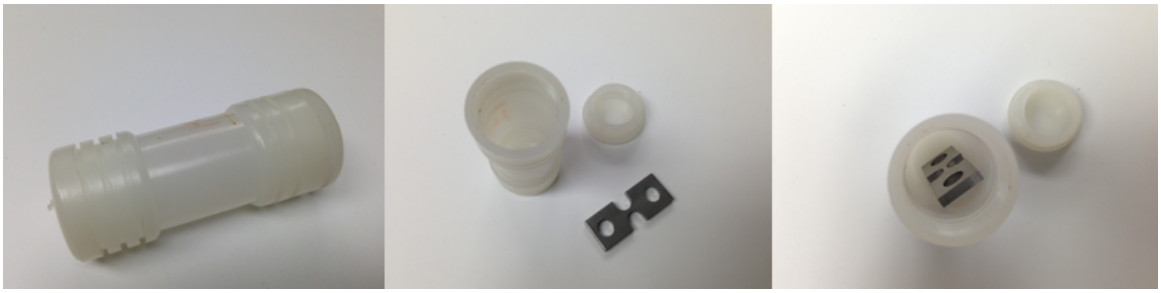

Figure 5-22: Polyethylene rabbit container (left) and a steel dog-bone sample enclosed in the container prior to irradiation.

In summary, the irradiation conditions in the MUTR were set in favor of maximizing the total neutron fluence.

- The steel sample was irradiated for a total of 87.49 hours in order to receive a total neutron fluence of 1 x 10^{18} neutrons/cm^2.
- The irradiation was carried out in the pneumatic transfer system of the MUTR; the location of the rabbit system in the core is shown in Figure 5-23.
- Similarly to the pelletron irradiation, the irradiation temperature did not exceed 100 ˚C; the temperature of the air inside the rabbit tube of the MUTR throughout reactor operations was approximately 70 to 90 ˚C.
- The irradiation time varied between 5 and 9 hours per day, in the span of 12 days, mainly depending on the power level in the reactor.

- Every irradiation required a change of sample holder since the rabbit container is made out of polyethylene; polyethylene is fairly susceptible to radiation degradation, and degrades within a relatively short period of time, becoming brittle. The sample was irradiated in the rabbit container for no more than 10 hours at a time. At each replacement of the container, a radiation survey was performed on the sample and the sample was returned to the core to minimize the radiation levels in the hot room of the MUTR.

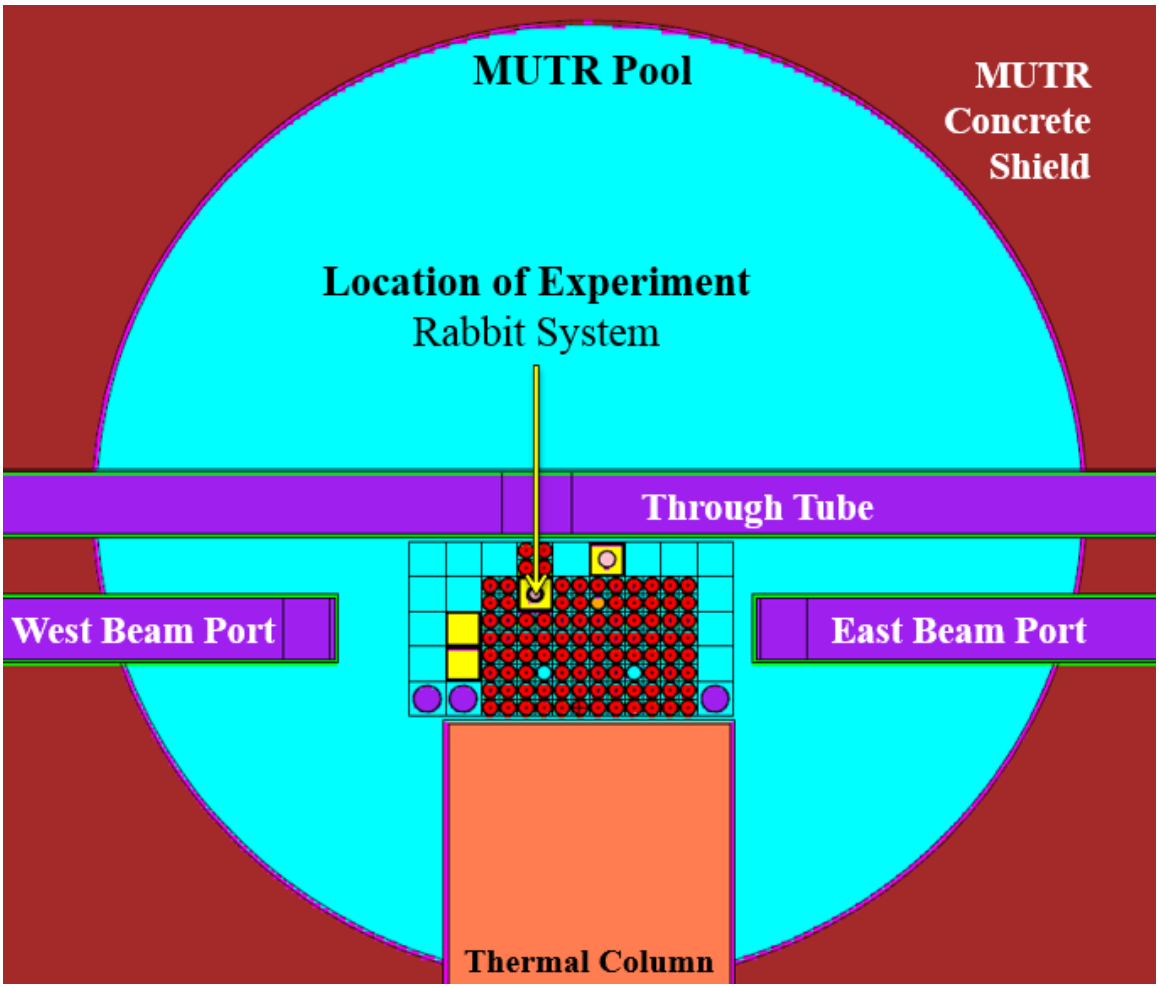

Figure 5-23: Top down view of the MUTR pool, with specified experiment's location.

Table 5-6 comprehensively shows the power level at which MUTR was operated to achieve the desired neutron fluence for the steel sample (expressed in neutrons/cm^2), as well as the sample's irradiation time (expressed in hours). These calculations are based on the experimental neutron flux data for the pneumatic transfer system (rabbit) shown in Table 5-5.

Table 5-6: Neutron irradiation of steel sample performed in MUTR.

Date	**Irradiation Time**	**Power**	**Total Thermal Fluence**	**Total Fast Fluence**
MM/DD/YYYY	**Hours**	**kW**	**n/cm^2**	
10/14/2013	6.50	200.00	7.49E+16	3.74E+16
10/16/2013	7.70	200.00	8.87E+16	4.44E+16
10/18/2013	8.53	200.00	9.83E+16	4.91E+16
10/21/2013	7.50	200.00	8.64E+16	4.32E+16
10/23/2013	0.75	175.00	7.56E+15	3.78E+15
	0.50	190.00	5.47E+15	2.74E+15
	6.75	200.00	7.78E+16	3.89E+16
10/25/2013	7.00	200.00	8.06E+16	4.03E+16
10/28/2013	8.50	200.00	9.79E+16	4.90E+16
10/30/2013	1.00	175.00	1.01E+16	5.04E+15
	7.00	200.00	8.06E+16	4.03E+16
11/1/2013	7.42	200.00	8.55E+16	4.27E+16
11/5/2013	7.34	200.00	8.46E+16	4.23E+16
11/6/2013	1.00	150.00	8.64E+15	4.32E+15
	1.00	175.00	1.01E+16	5.04E+15
	1.00	190.00	1.09E+16	5.47E+15
	1.80	200.00	2.07E+16	1.04E+16
11/8/2013	0.70	185.00	7.46E+15	3.73E+15
	5.50	200.00	6.34E+16	3.17E+16
Total →	**87.49**		**1.00E+18**	**5.00E+17**

After irradiation and transfer to the reactor's "hot room", the activity of the sample was measured with beta and gamma monitors and allowed to decay to a radiation level of less than 100 mR/hr at 30 cm from its surface. Once the radiation level of less

than 100 mR/hour at 30 cm from the sample was attained, the sample was transferred to a shielded container (lead pig) for shipment to Idaho State University for further characterization.

6 Characterization Methods, Experimental Results and Analysis

Idaho State University's Research and Innovation in Science and Engineering Complex contains their Applied Microscopy Laboratory that includes the following instruments: focused ion beam (FIB), combined focused ion beam/scanning electron microscope (FIB/SEM – dual beam) system, two transmission electron microscopes (TEM) and an environmental scanning electron microscope (ESEM) with electron backscatter diffraction (EBSD) capabilities.

After irradiation with negative hydrogen ion beam, the analysis of the samples was carried out via focused ion beam, scanning electron microscope and transmission electron microscope. Machining of the *LightGauge* samples and fabrication of lamellas for use in TEM was performed using both the FIB and the dual beam and imaging of the samples was performed with SEM, FIB and TEM. Some of the sample's characterization work was performed at the University of Maryland's NanoCenter via SEM and TEM imaging.

6.1 Characterization Methods

6.1.1 Focused Ion Beams

Focused ion beams and dual beam systems are vital tools for nanomaterial sample preparation, characterization, atomic deposition, imaging, as well as the etching of high aspect and high resolution structures [148].

FIB operates in a similar fashion to that of a scanning electron microscope (SEM) such that as the name of this technique implies, a focused beam of heavy ions is used (usually gallium, oxygen, cesium, etc.) rather than electrons [149], [150]. A gallium (Ga) liquid metal ion source (LMIS) is the most extensively used source in FIB instruments due to its operational stability and manufacturing simplicity [151]. Applying a very high electric field onto a liquid metal ion source wherein a reservoir of gallium is placed in contact with a sharp tungsten (W) needle, generates the ions. The gallium wets the needle and flows to its tip. Ions are emitted as a result of field ionization and post-ionization and are focused by electrostatic lenses into a typically 5 to 10 nm radius [152], which allows for instance, preferential machining on the surface while producing high quality photonic crystal structures amongst other uses. Also, the FIB is capable of creating an image of a sample with up to about 100,000 times magnifications due to the intensity of the secondary electrons produced at each raster position of the beam [153].

When a Ga^+ ion is accelerated toward the sample's surface, as shown in Figure 6-1, it creates a cascade of events which generate secondary electrons, secondary ions, neutral atoms or implantations of Ga^+ [153]. This is known as "sputtering", which is a process of ejecting atoms from a solid material via bombardment of the target material by energetic particles with kinetic energy higher than 1 eV. The sputtering process allows for local milling of the material. Expertise of the sputtering process is essential for operation of focused ion beam systems.

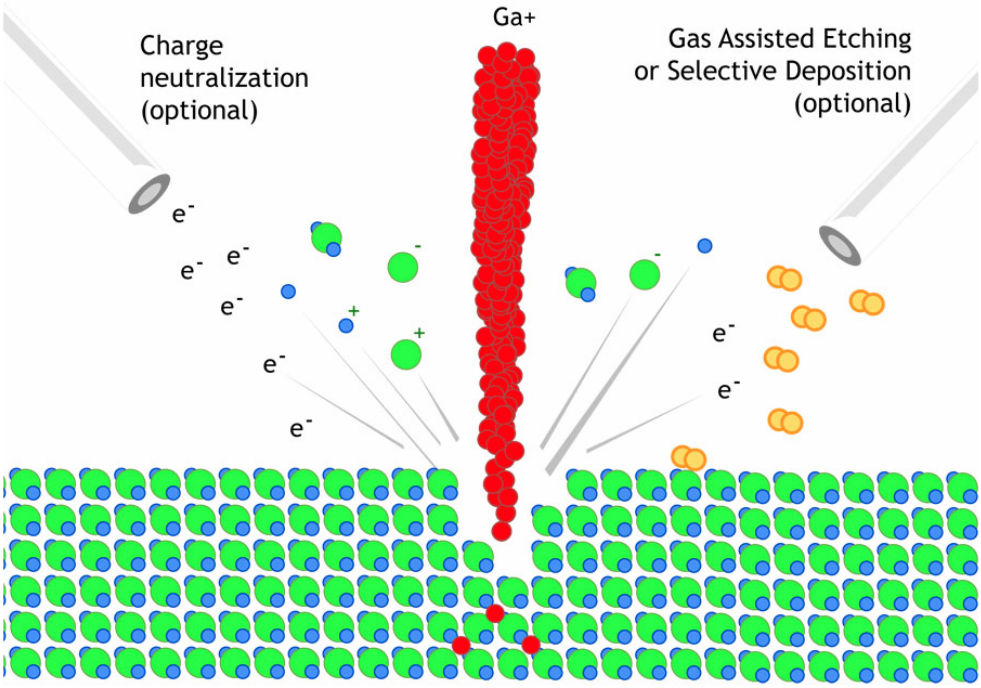

Figure 6-1: Focused ion beam sputtering process, Ga^+ strikes the surface of the material and generates electrons, ions and sputtered material; The red circles represent the gallium ions, e^- represents the secondary electrons, circles with "+" sign represent the secondary ions and the green/blue circles that are removed from the surface represent the sputtered material. [149]

The focused ion beam model that was utilized for fabrication and characterization of the *LightGauge* sensors is the FEI FIB800 (Figure 6-2). This instrument is equipped with a prelens, 30 kV, gallium liquid metal ion source. The prelens column features a working distance of 16.5 mm and an extractor voltage of 7 kV. The instrument features an eight inch plate to house multiple samples simultaneously, and a loadlock chamber to eliminate the necessity to vent and evacuate during exchanges. The sample stage of the system is fully motorized and

provides automated control of the x-y plane and tilt of the x-z plane. The stage can be controlled using a computer. The FIB also features two gas injection systems that can be initiated to provide for enhanced etching and/or platinum deposition.

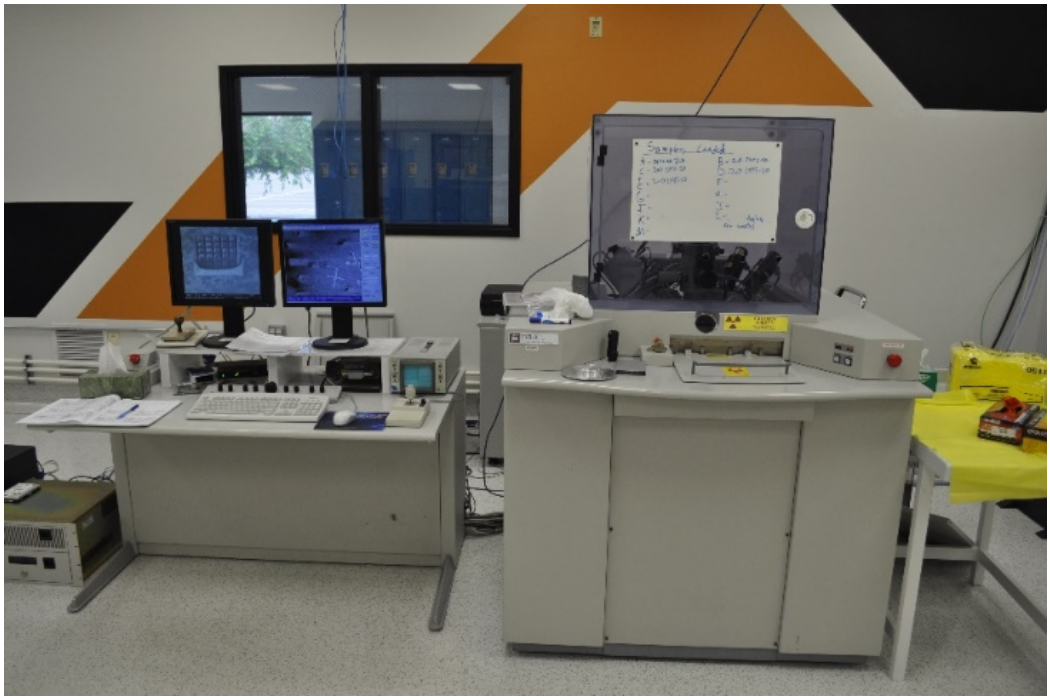

Figure 6-2: A photograph of FEI FIB800, the focused ion beam model that was utilized for characterization of the *LightGauge* samples.

Most modern FIB tools incorporate both focused ion beam and scanning electron microscope column with the purpose of turning the instrument into a multipurpose apparatus called “dual-beam”, shown in Figure 6-3, which allows for sample preparation, imaging, and analysis to be accomplished with one instrument. The SEM imaging during FIB milling enables real-time monitoring of the milling process.

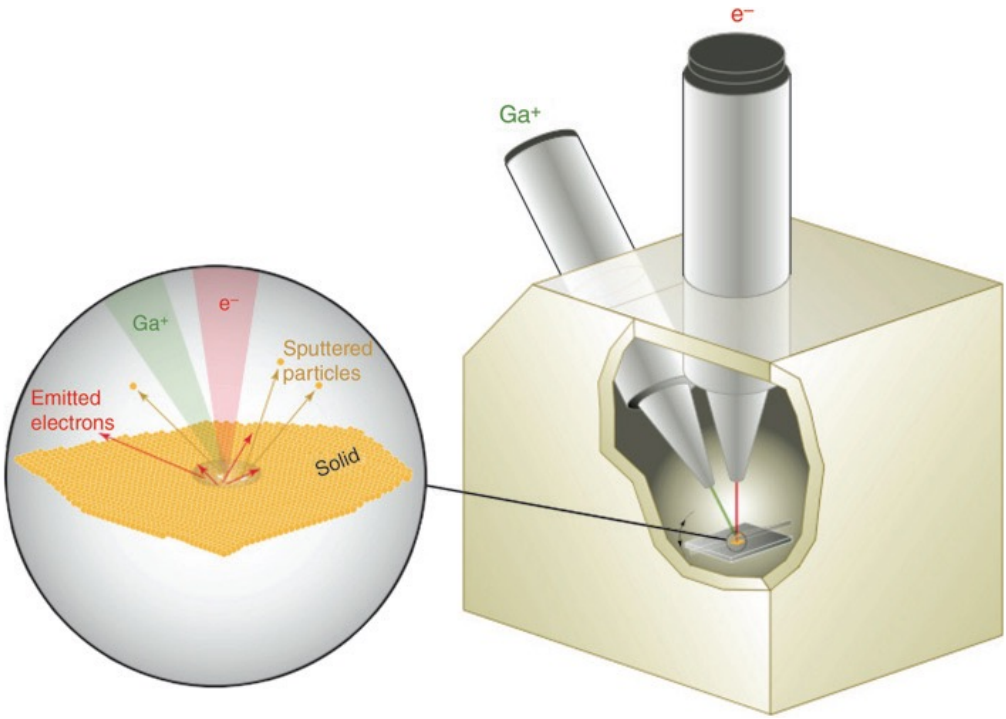

Figure 6-3: Schematic illustration of a dual-beam FIB–SEM instrument. Expanded view shows the sample interaction with the electrons from the scanning electron microscope and Ga^+ ions from the focused ion beam [150]

A key benefit of the dual beam is the ability to use the electron beam for imaging while milling, without a concern of damaging the sample surface. This technique is known as "mill and image" technique (or "slice and view" used by FEI), which can be automated and can produce series of SEM images [154]. The dual beam is also very useful in preparing precise cross-sectional specimens for TEM characterization; this technique is explained in section 6.2.1.

The dual beam utilized in this work for characterization and fabrication of the *LightGauge* sensors is FEI DualBeam835 (Figure 6-4). Similarly to the single beam FIB, the dual beam is equipped with a 30 kV gallium ion column. In this case, the ion

column is called “Magnum” and features a working distance of 18 mm and an extractor voltage of 10-12 kV that provides faster milling than the single beam FIB. In addition to the ion column, the dual beam is equipped with a 30 kV field emission gun (FEG) electron column. The dual beam has a loadlock chamber with an eight inch plate for samples, and its sample stage is fully motorized and automated in similar fashion to the single beam FIB. This instrument also features an “OmniProbe” needle to allow for physical micromanipulations, a x-ray energy dispersive spectroscopy system and two needles for gas injection that are configured for platinum and tungsten deposition.

Figure 6-4: A photograph of FEI DualBeam835, the dual beam model that was utilized for fabrication and characterization of the *LightGauge* samples.

6.1.2 Electron Microscopes

Electron microscopes are capable of extremely high magnifications (up to two million times), allowing smaller objects to be viewed in detail. In comparison to a light microscope, electron microscopes use electrons instead of photons for visualization, and electromagnets instead of transparent discs to focus the image of a sample. The basic design of an electromagnetic lens is a solenoid (a coil of wire around the outside of a tube) with a current passing through thereby inducing an electromagnetic field. The electron beam passes through the center of such solenoids on its way down the column of the electron microscope towards a sample and is increasingly focused. Electrons are very sensitive to magnetic fields and as a result changing the current through the lenses can control the shape and path of the electron beam.

The main advantage of electron microscopy over optical microscopy is their capacity to perform detailed micro-structural analysis through high resolution (better than 1 nm) and high magnification (of the order of 10^5 times) imaging [155]. Because the electron beam has a far smaller wavelength (0.0025 nm for 200 keV electrons) than light (400 – 800 nm [156]) used in optical microscopy, it reaches far better resolution. Electron microscopy is used comprehensively throughout the sciences in order to examine the structure of cells, bacteria, and viruses in biology; to study defects in metals, crystals, and ceramics in materials science; or to study rocks, minerals, and fossils in geology. The scanning electron microscope and the transmission electron microscope are the main two types used in electron microscopy.

As their names suggest, an SEM scans the surface of a material using a rastering beam of electrons whereas the electrons produced by a TEM are visualized after they have passed (transmitted) through the sample. In relation to this dissertation, electron microscopy was employed to investigate the radiation effects of the *LightGauge* sensors applied to fuel cladding materials. Since the *LightGauge* sensors are on the order of nanometer scale, transmission electron microscopy has played a central role in the characterization of these nanostructures.

6.1.2.1 Transmission Electron Microscope

A transmission electron microscope is an instrument that creates a detailed image by transmitting electrons through an ultra-thin sample (10 to 200 nm). The sample's thickness depends on the material's composition as well as the purpose of the TEM analysis. As shown in Figure 6-5, this microscope consists of an electron source from where the high voltage electron beam is discharged, a series of electromagnetic lenses through which a strong magnetic field is generated, a sample holder and an imaging system (usually composed of a charge-coupled device (CCD) camera).

Transmission electron microscopes are capable of providing compositional, morphological and crystalline information, making it possible to analyze the structure and texture of samples on molecular and even atomic level.

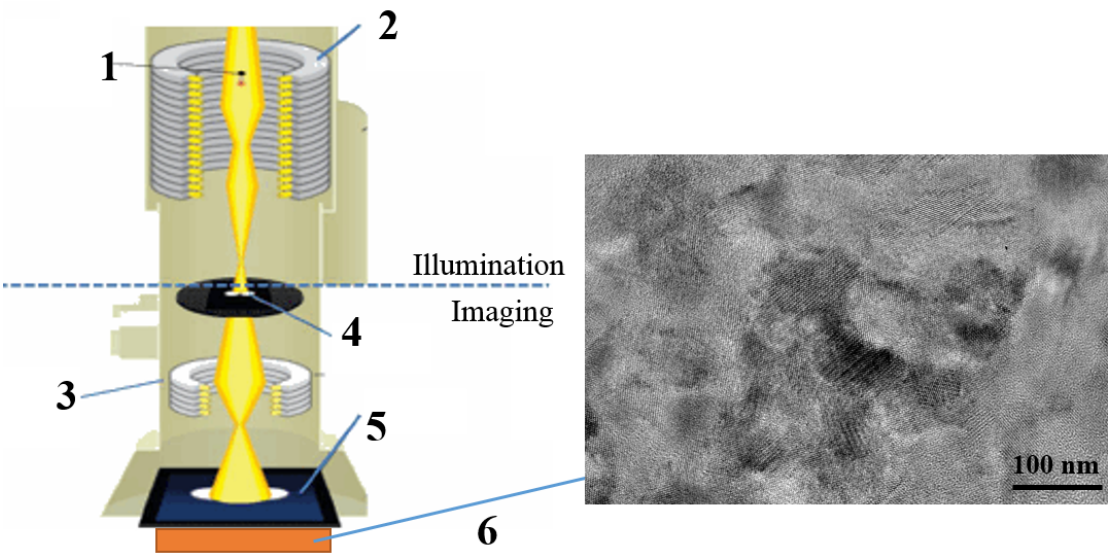

Figure 6-5: Schematic of a transmission electron microscope where 1 represents the electron beam, 2 the condenser lens, 3 the focusing lens, 4 the sample that is being investigated, 5 the fluorescent screen and 6 a CCD recorded TEM image of a zircaloy-4 sample. [157]

6.1.2.2 Preparation of TEM Lamellas

Characterization of samples with a transmission electron microscope requires special preparation/thinning in order to form specimens that are transparent to electrons without the introduction of damage by the sample preparation method. This step directly affects the quality of results obtained by TEM analysis. A focused ion beam is presently the most advanced tool used for preparation of TEM lamellas. The preparation method is presented in four steps:

1. Rough milling of the lamella where the focused ion beam is used to create a region of interest out of the sample's bulk material (Figure 6-6);

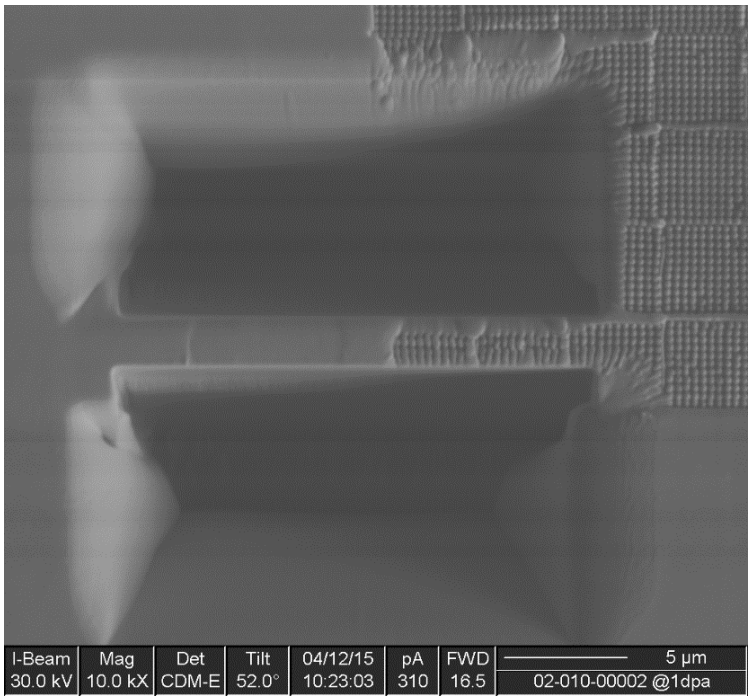

Figure 6-6: FIB micrograph; rough lamella on zircaloy-4 sample. The left half of the lamella was created by milling into the bulk material of the sample, where the right half represents a portion of the *LightGauge* sensor.

2. Lift-out of the lamella where the rough lamella is attached onto a tungsten needle (through a platinum deposition between the needle and the specimen to assure firm attachment), shown in Figure 6-7, followed by the milling of the regions around the lamella that will allow for detachment of the lamella from the bulk material and eventual lift-out; dual beam is preferred instrument over single beam FIB for lift-out techniques since the lifting of the sample can be directly monitored through the SEM mode;

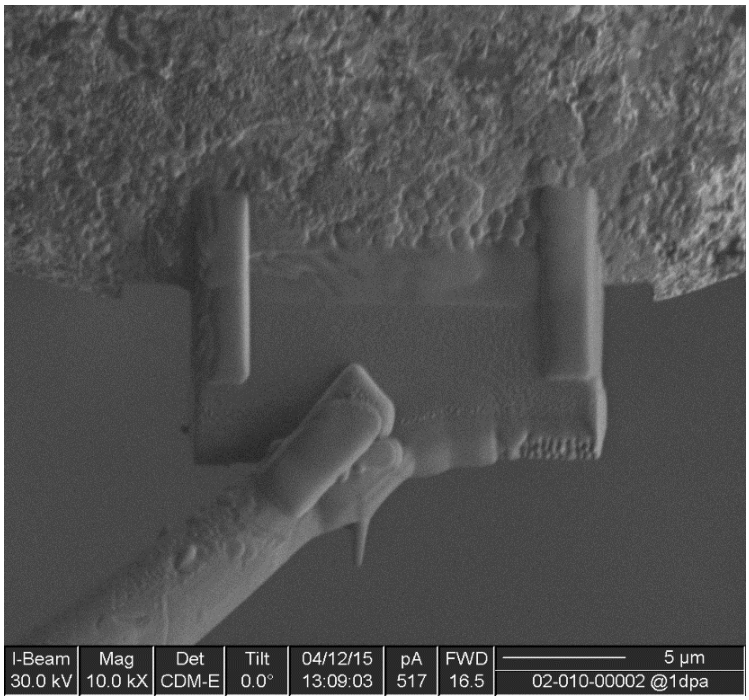

Figure 6-7: FIB micrograph; Zircaloy-4 lamella is attached onto a tungsten needle.

3. Thinning of the lamella by slicing cross sections of the desired region with precise focused ion beam milling until the desired final thickness is achieved;

4. Polishing of the lamella is performed in a similar manner to the thinning process with lower voltage and current of the ion beam (typically 2-5 keV and 2-5 nA);

Two TEM models were used for characterization of the *LightGauge* samples, one located at the Idaho State University's RISE complex and one located at the University of Maryland's NanoCenter.

The TEM at ISU is a JEOL JEM 2000FX model (Figure 6-8) which can operate at an accelerating voltage of up to 200 keV and magnifications as high as 800,000 times. The sample chamber is equipped with a side sample entrance (with z-axis control) and an automatic airlock and a roughing pump system. This microscope has triple condensed lens system with a built-in focus and magnification, and double objective lens system with digital controls for coarse and fine focusing.

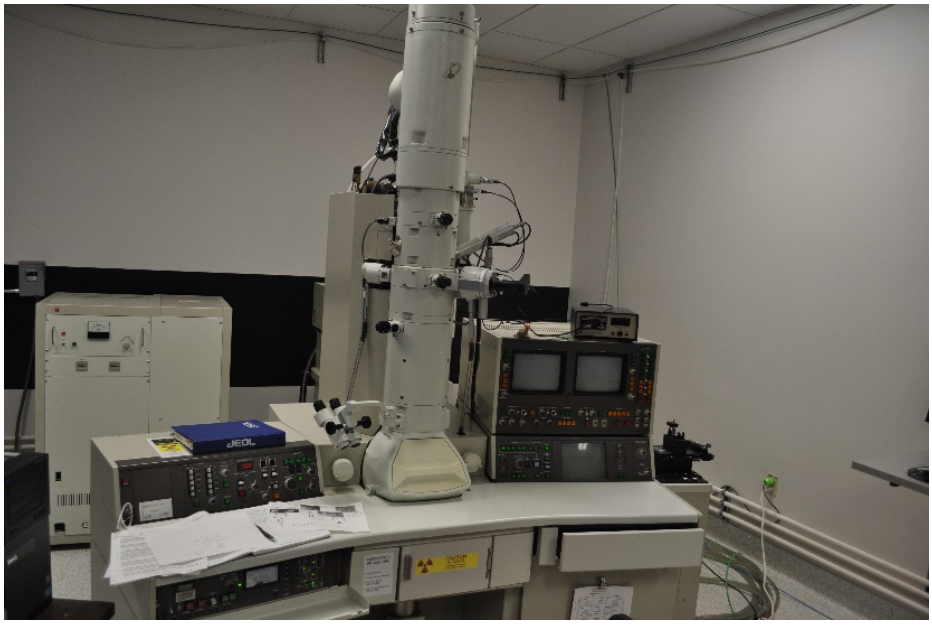

Figure 6-8: A photograph of JEOL JEM 2000FX, TEM model at the RISE complex that was utilized for characterization of the *LightGauge* samples.

The TEM at UMD is a JEM 2100 LaB_6 model (Figure 6-9) which is a model similar to the one at the RISE complex. It consists of three independent condenser lenses and produces the highest probe current for any given probe size. It also allows the user to select of various illumination conditions, ranging from full convergent

beam to parallel illumination. These functions enable improved analytical and diffraction capabilities in addition to high resolution imaging [158].

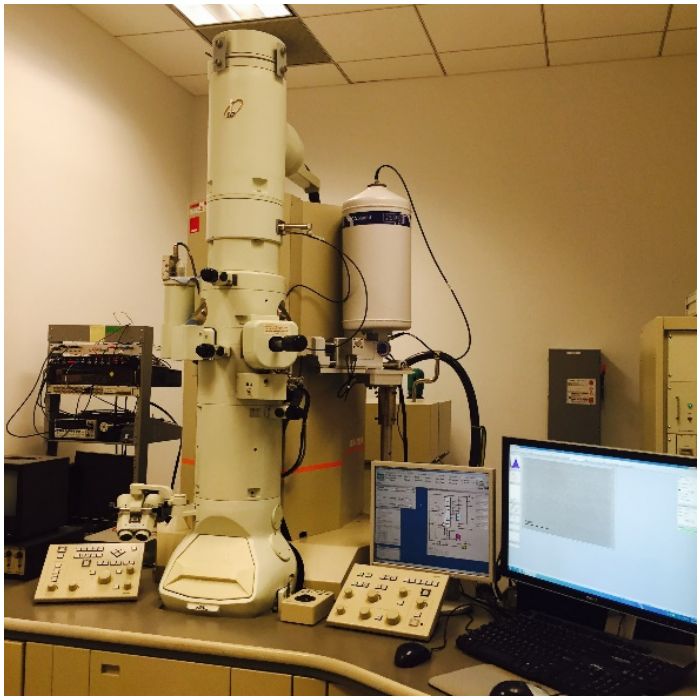

Figure 6-9: A photograph of JEM 2100 LaB6, a TEM model at the AIMLab that was utilized for characterization of the *LightGauge* samples.

6.1.2.3 Scanning Electron Microscope

Similarly to a transmission electron microscope, a scanning electron microscope uses a focused beam of electrons to create an image of a sample. SEM focuses electrons into a fine point on a sample's surface and rasters the beam in a rectangular pattern in order to obtain an image [68], [159]. When the beam of electrons impacts the sample, it produces secondary electrons, backscattered electrons, x-rays, and light. Any one of these signals can be collected by a specific detector in the microscope. A schematic of an SEM is presented in Figure 6-10.

Secondary electrons and backscattered electrons are usually used for imaging samples: morphology and topography on samples are shown by secondary electrons and backscattered electrons reveal contrasts in structure in multi-phase samples. The primary use of scanning electron microscopy is to study the surface topography of solid samples as well as the interior structures exposed by cross sectioning techniques down to nanometer scale.

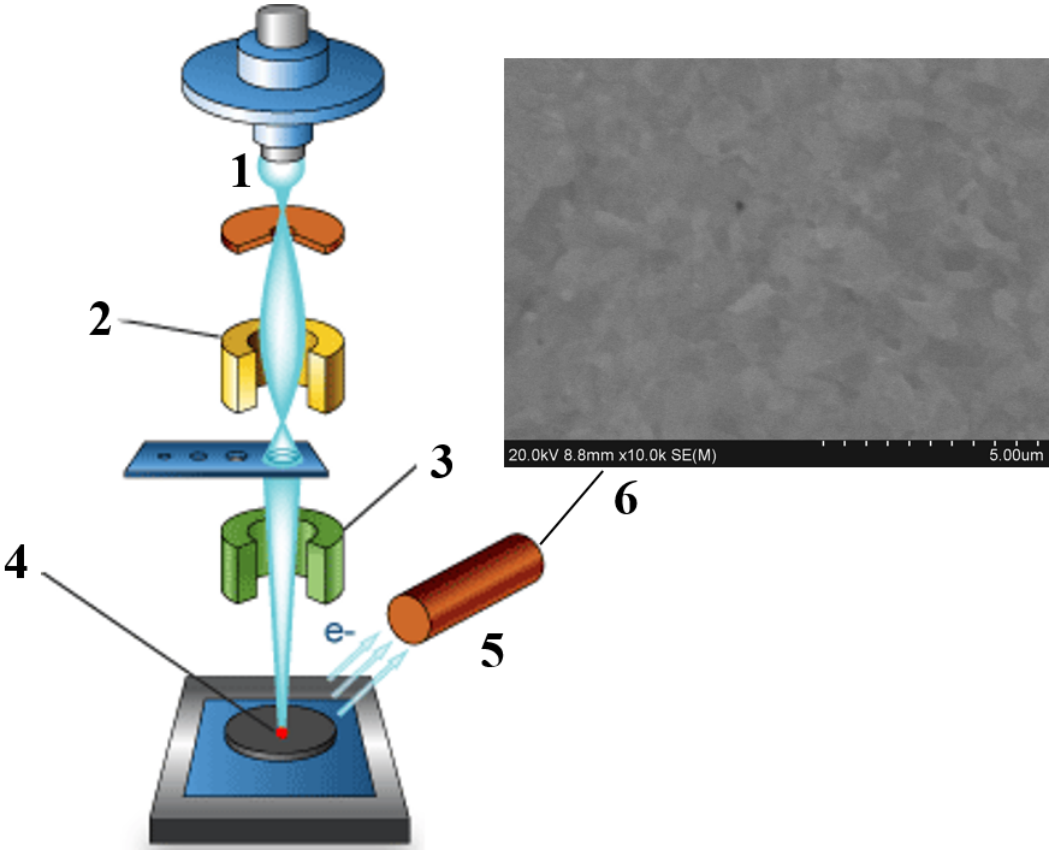

Figure 6-10: Schematic of a scanning electron microscope where 1 represents the electron beam, 2 the condenser lens, 3 the focusing lens, 4 the sample that is being investigated, 5 the secondary electron detector and 6 an SEM image of a steel sample [160].

Unlike the TEM, the sample preparation for an SEM is minimal; the samples need to be inherently electrically conductive or they need to be coated with a conductive layer of gold or carbon. The resolution of SEM is two orders of magnitude better than optical microscopes and one order of magnitude less than a TEM [161].

The scanning electron microscope that was utilized in the experimental work of this thesis is the FEI/Phillips XL30 Field Emission ESEM-FEG (Figure 6-11). The XL30 ESEM features a high brightness FEG source with a conventional electron column; this machine has operating capabilities up to 30 kV with a 2 nm digital resolution. Contrasting conventional SEMs which involve high vacuum in the sample chamber, the ESEM can be operated in a "high-pressure" environmental mode that allows examination of hydrated or insulating samples. This is very useful for investigation of biological samples.

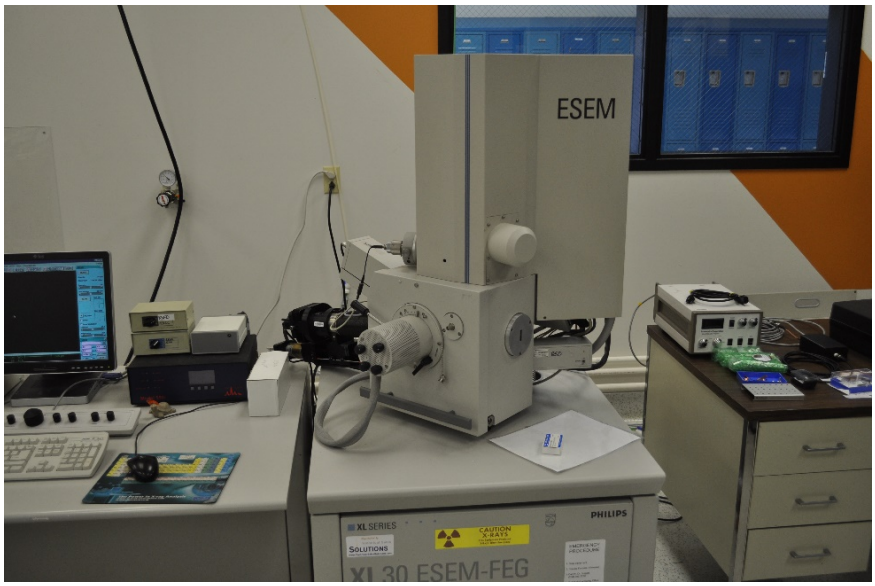

Figure 6-11: A photograph of FEI/Phillips XL30 Field Emission ESEM-FEG, the SEM model that was utilized in characterization of the *LightGauge* samples.

6.1.2.4 Electron Backscatter Diffraction

Electron backscatter diffraction (EBSD) is a method of investigating the crystallographic orientation of crystalline materials. In EBSD, the accelerated electrons from the SEM interact with a tilted crystalline sample and the diffracted electrons form patterns, called Kikuchi bands (shown in Figure 6-12, represented by the number 7), on the detector. The actual detector is a camera with an integrated phosphor screen (shown in Figure 6-12, represented by the number 5). The diffraction patterns are characteristic of the crystal structure and orientation in the sample region with the respect to the electron beam where they were generated. These Kikuchi patterns are of great value because they can be used to determine crystal orientations or different phases of crystals, characterize grain boundaries, and provide information about defects in the local crystalline structure. The discovery of EBSD by Shoji Nishikawa and Seishi Kikuchi dates back to 1928 when a gas discharge beam of 50 keV electrons was directed on a cleavage face of calcite at a grazing incidence of 6° and a crystallographic pattern was obtained [162].

The ESEM that was utilized in this work is equipped with an electron backscatter diffraction detector. As mentioned before, the electron backscatter diffraction is very useful technique for investigating the changes in crystallographic orientation as a result of irradiation. EBSD is a technique performed on the surface of a sample, therefore the sample preparation is absolutely critical. Any damage of the surface layer would either deteriorate or prevent the ability to see any diffraction patterns. Hence, use of EBSD requires mechanical polishing, electro-polishing or

chemical treatment to remove any unwanted material from the surface of the sample and create a finely smooth surface [162], [163]. For the purpose of this study, EBSD was performed on the materials of interest; however, every attempt was unsuccessful due to sample's surface roughness.

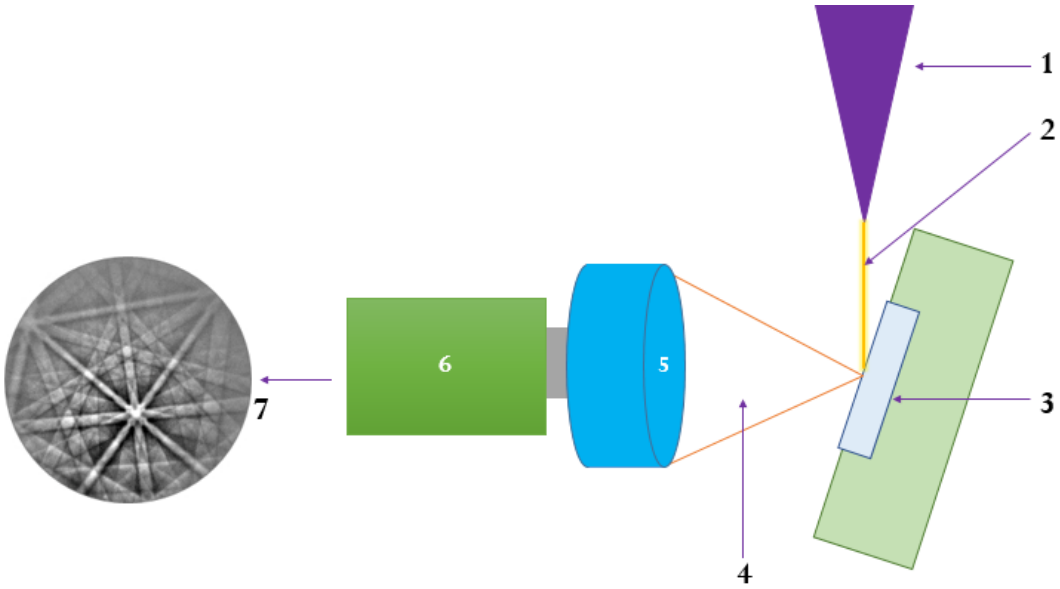

Figure 6-12: Electron backscatter diffraction diagram; 1 represents the objective lens, 2 represents the electron beam, 3 represents the sample, 4 represents the cone of backscattered electrons, 5 represents the camera with phosphor screen, 6 represents the EBSD detector and 7 is an actual Kikuchi pattern; [163], [164]

6.2 Experimental Results and Analysis

6.2.1 Post Irradiation Examination of the Neutron-irradiated *LightGauge* Sensors

The neutron irradiation of one steel sample is described in section 5.5 of Chapter 5. After irradiation, the steel sample was shipped from University of Maryland to Idaho State University for further characterization. When the sample was received by Idaho State University, it was immediately imaged via focused ion beam and scanning electron microscopy. The *LightGauge* sensor images pre- and post-irradiation are shown in Figure 6-13.

Figure 6-13 (bottom), a FIB micrograph of the post-neutron-irradiation of the *LightGauge* sensor on steel sample and Figure 6-14, a SEM micrograph of the same display a large scratch running directly over the photonic crystal, which possibly occurred during shipment rather than being caused by radiation. This occurrence has made it very challenging to determine the degree of damage instigated by irradiation since in the early stages of this project, the post-irradiation analysis focused on optical interrogation of the photonic crystals rather than microstructural analysis.

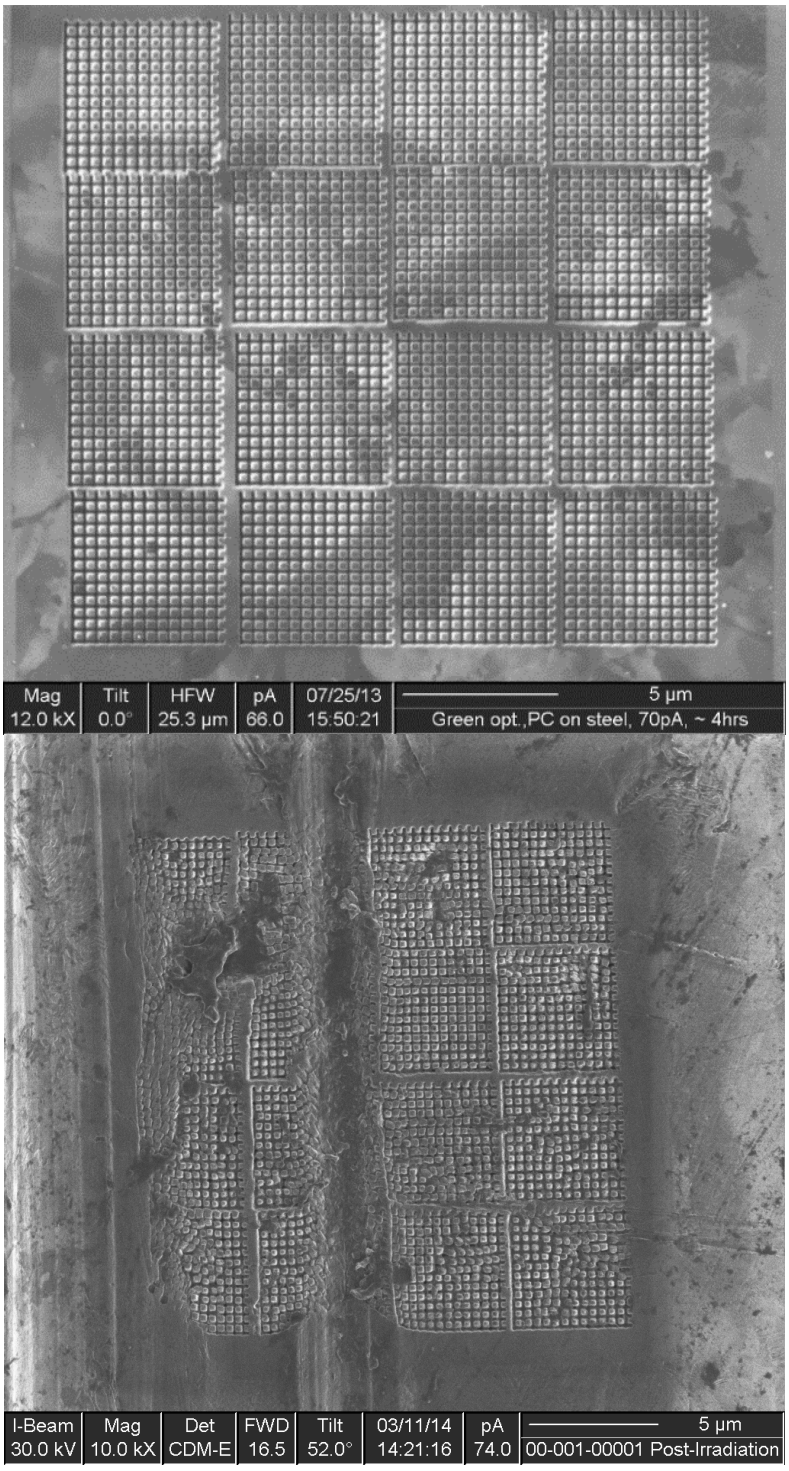

Figure 6-13: FIB micrographs of *LightGauge* sensor on steel sample (4 x 4 array square lattice); pre-neutron-irradiation image (top) and post-neutron-irradiation image (bottom).

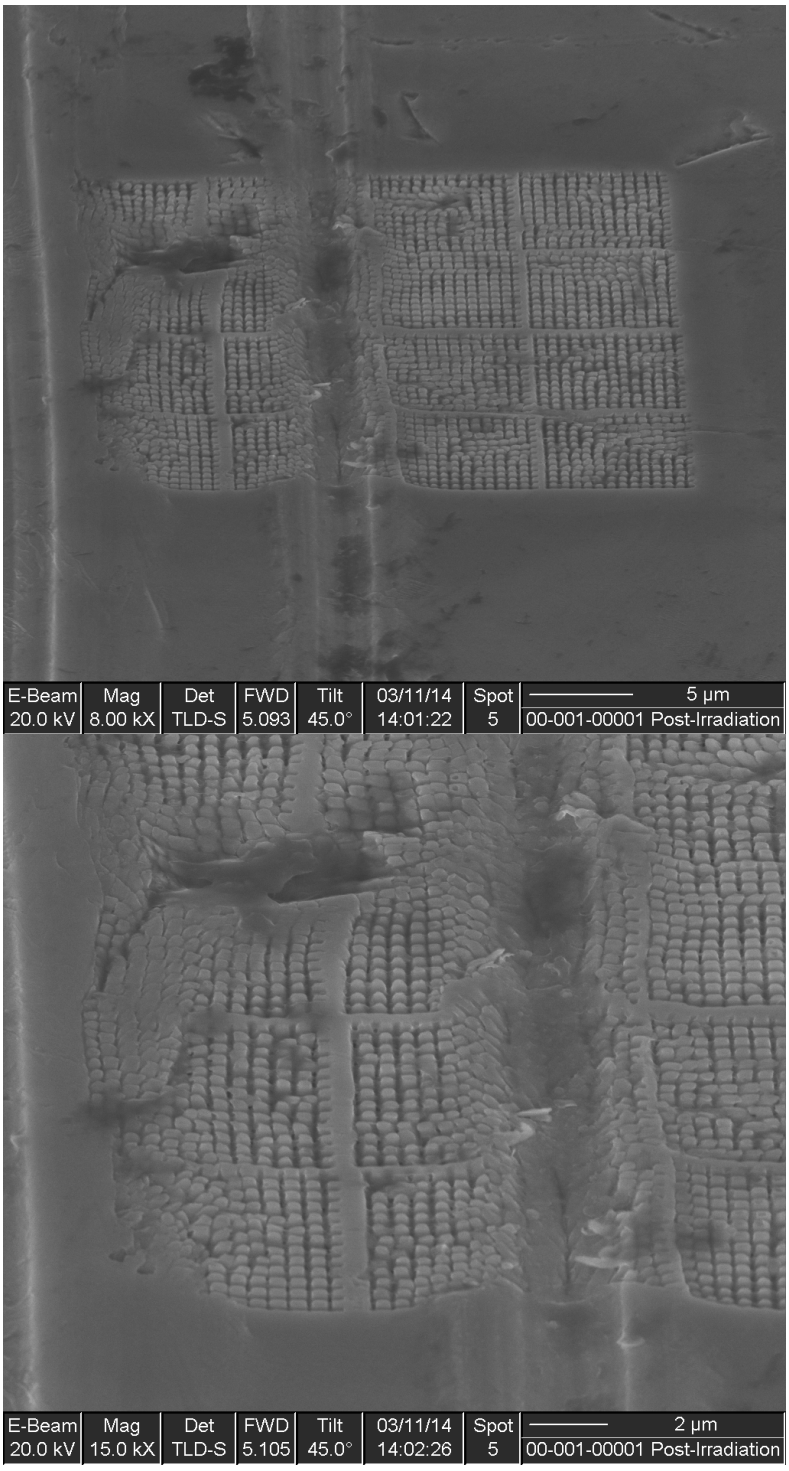

Figure 6-14: SEM micrograph of *LightGauge* sensor on steel sample (4 x 4 array square lattice) post-neutron-irradiation; the large scratch through the sensor (top) and magnified view of the same (bottom) is easily distinguished.

The *LightGauge* sensors were designed on the assumption of light being incident on them perpendicular to the axis of the rods, it is necessary to use side lighting in order to observe any photonic effects. Therefore, lighting was provided and its incident angle was manipulated in order to observe photonic effects.

The results concluded that despite the presence of mechanical damage on the *LightGauge* sensor, it appears that the crystals away from the large scratch will still exhibit photonic effects. Optical micrographs of the photonic crystal, seen in Figure 6-15, show a weak, but still visible blue-green reflection.

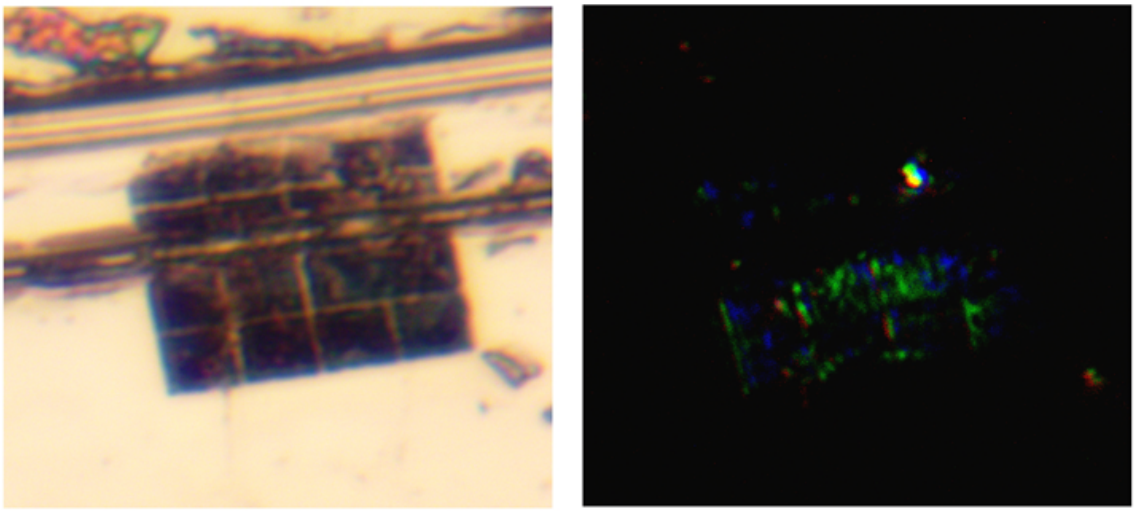

Figure 6-15: Optical micrographs of *LightGauge* sensor on steel sample (4 x 4 array square lattice) post-neutron irradiation; top-light image (left) and side-light image (right).

In addition to the optical interrogation of the neutron irradiated sample, physical deformation analysis of the pillars was performed via ImageJ software [165] using the FIB and SEM micrographs. The FIB and SEM micrographs of both

unirradiated and irradiated sample were converted into suitable format (black and white images and an appropriate threshold selection was set) to enhance the ability to execute particle analysis. Since the pillars of the photonic crystal have square-type shape (Figure 6-16), their area was easily measured through the ImageJ software. Further, the data was imported to a data analysis software for statistical analysis.

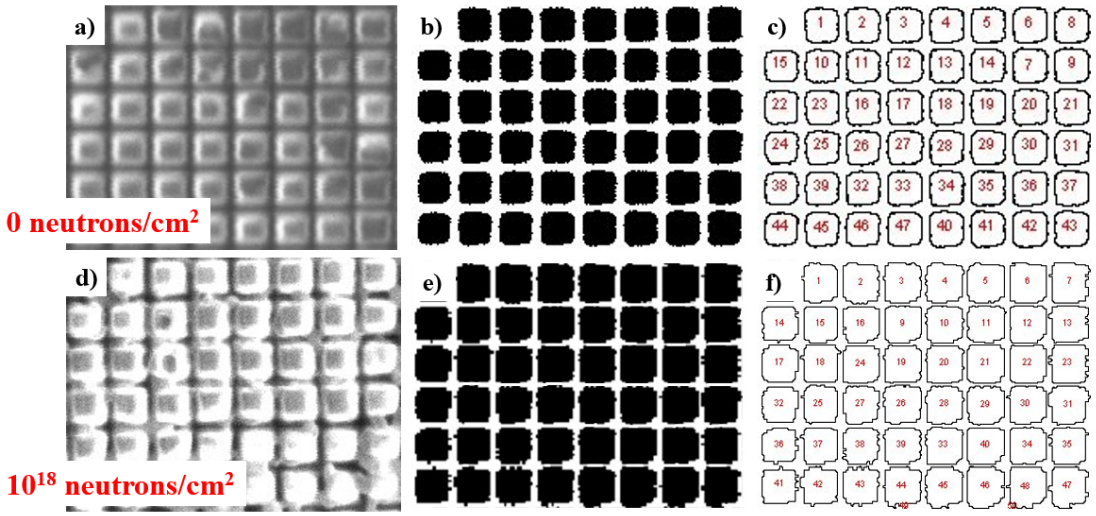

Figure 6-16: Example of physical deformation analysis of the neutron-irradiated steel sample where a) and d) represent FIB micrograph of unirradiated and irradiated pillars of the *LightGauge* sensors, respectively; b) and e) represent ImageJ format of the same; c) and f) particle outlines and an example of number of particles included in the measurement used for pillar size estimation.

Figure 6-17 provides the results obtained from the particle size analysis where approximately 100 different pillars were considered in the measurements. In Figure 6-17, the area of the unirradiated pillar in the steel sample is represented by the red color scatter plot and the area of the neutron irradiated pillar is represented by the green color scatter plot. As determined by the mode of the data for both unirradiated

and neutron-irradiated sample, the irradiated pillars show an 18% increased in size. The interaction of neutrons with steel result in lattice rearrangements and a buildup of dislocations, damage to the crystal structure and voids in the material. This event typically results in an increase of volume of the materials known as a neutron-induced swelling. However, the 18% swelling is much higher than expected and could be attributed to the mechanical damage suffered during shipment and conducting a radiation wipe test.

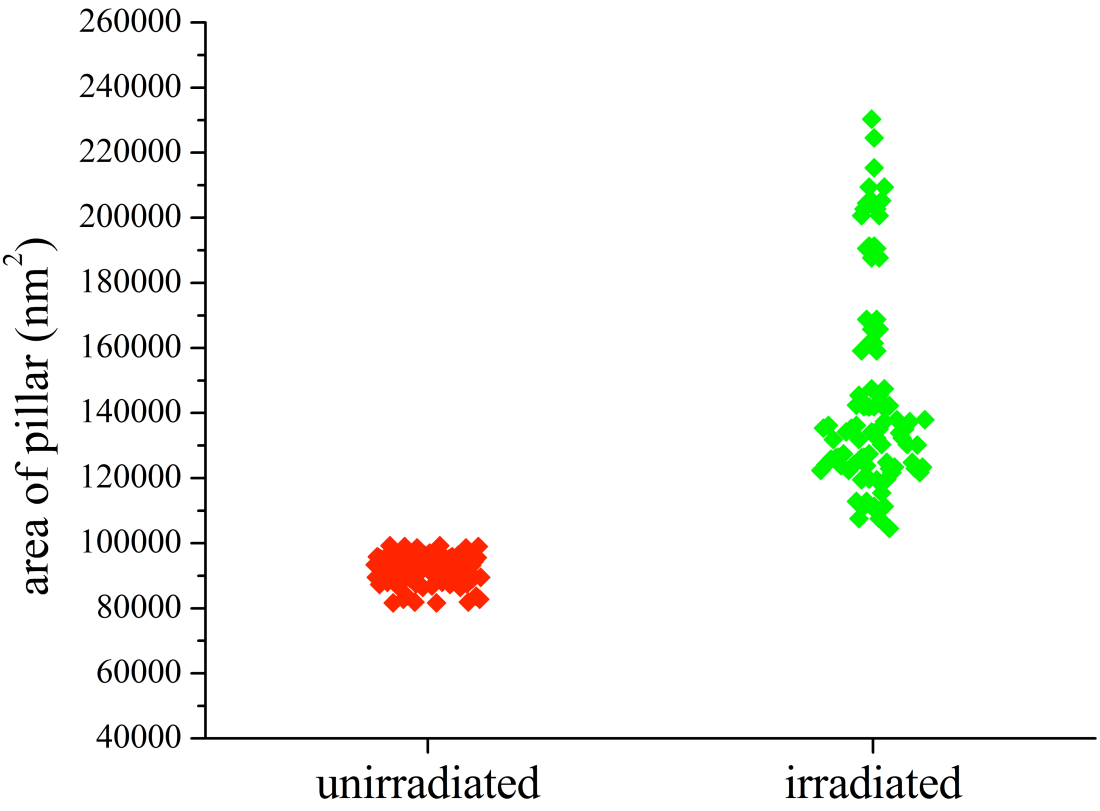

Figure 6-17: Pillar size change post-neutron-irradiation of the steel sample where the area of the unirradiated and irradiated sample is represented by "red color scatter plot" and "green color scatter plot", respectively.

6.2.2 Post Irradiation Examination of the Ion-irradiated *LightGauge* Sensors

The ion irradiation of both steel and zircaloy-4 samples is described in section 5.3 of Chapter 5. After every irradiation, the samples were imaged via focused ion beam and a TEM lamella was removed out of a single sensor for further characterization. The FIB images were used to perform swelling analysis of the samples to determine if any physical deformation of the *LightGauge* sensors occurred. This is described is section 6.2.2.1 of this chapter. Further, the samples were imaged via transmission and scanning electron microscopy, both at Idaho State University and University of Maryland. This was done in order to reveal microstructure information regarding the samples and it is described in section 6.2.2.2.

6.2.2.1 Comparison of Physical Deformation between Different DPA Levels

Similar to the neutron irradiated sample analysis, swelling analysis of the ion irradiated samples was performed using ImageJ. After every ion irradiation, high-resolution FIB mosaics were taken for both samples. Each high-resolution FIB mosaic, representing a different dpa level, was converted into the appropriate format for particle size estimation using the same technique as the neutron irradiated sample. Furthermore, the area of every pillar was measured and an average of the areas was computed. Uncertainty in the pillar analysis was mostly dominated by the actual image quality. Several factors contributed to the evaluation of the measurement uncertainty such as the image magnification uncertainty, the threshold selection in the

converted black and white image and the precise allocation of the pillars by the software. However, ImageJ provided a standard deviation error for each measurement that is included in the figures. The results together with their uncertainty are presented in Figure 6-18 for the steel sample and Figure 6-19 for the zircaloy-4 sample.

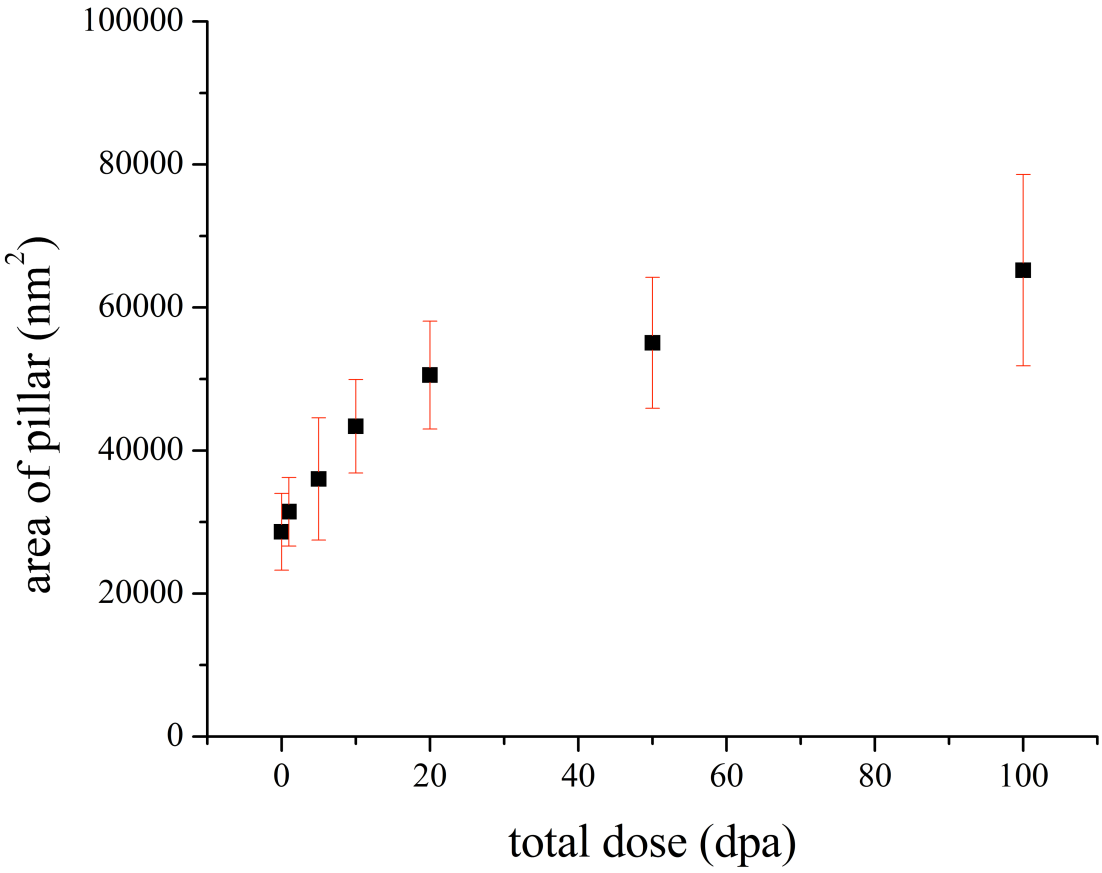

Figure 6-18: Pillar size change post-ion-irradiation of the steel sample. The plot represents the average area of the pillars over different fluence levels. The error bars indicate the standard deviation of uncertainty associated with the pillar measurements.

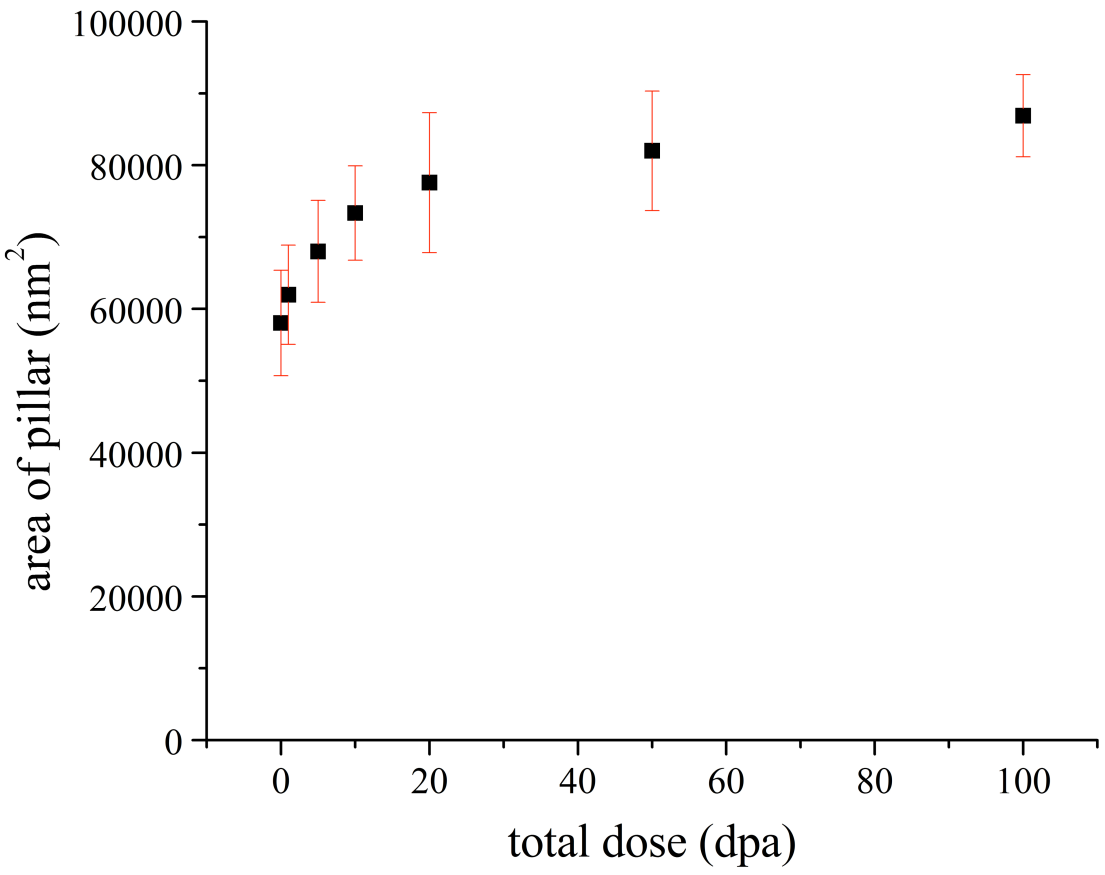

Figure 6-19: Pillar size change post-ion-irradiation of the zircaloy-4 sample. The plot represents the average area of the pillars over different fluence levels. The error bars indicate the standard deviation of uncertainty associated with the pillar measurements.

Additionally, Figure 6-20 provides the average swelling percentage of the pillar's area as a function of dose for both steel and zircaloy-4 sample. It can be noted that the ion-induced percent swelling experienced in the steel sample is pronouncedly higher than the zircaloy-4 sample. This is due to creation of interstitials that tend to form clusters and expand the system. This occurrence is common for steel alloys,

while zirconium alloys experience uneven dimensional changes in different directions of their HCP lattice [80].

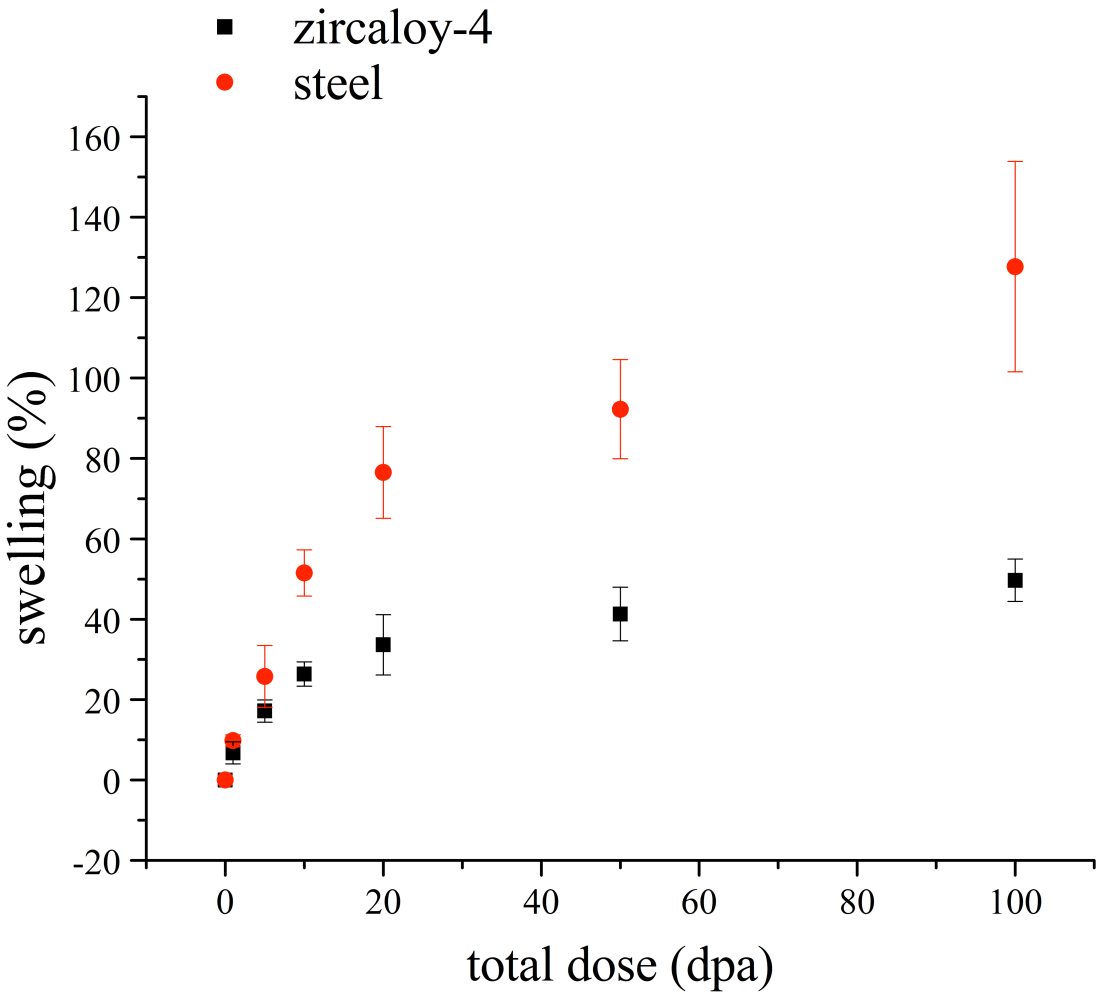

Figure 6-20: Percent swelling in steel and zircaloy-4 samples for every dose level post-ion-irradiation. The error bars indicate the standard deviation of uncertainty associated with the pillar measurements.

6.2.2.2 Grain Size and Lattice Parameters Changes

The ion irradiation of the steel and zircaloy samples is described in section 5.3 of Chapter 5. Since both samples were subjected to ion fluencies ranging from 0 to 100 dpa, after every irradiation, each sample was imaged using a focused ion beam and a TEM lamella was cut and removed from a *LightGauge* sensor for further characterization via transmission electron microscopy.

High-resolution TEM images were taken using the JEOL JEM-2000FX TEM model at the RISE complex in Idaho; however further characterization was required to obtain more structural information about the samples. Therefore, the already-cut lamellas were shipped to the University of Maryland, where they were further investigated at the Maryland NanoCenter's AIMLab using a JEOL 2100 LaB_6 TEM [166].

The TEM imaging performed at the AIMLab consisted of taking series of images along the depth of a single pillar that belonged to a *LightGauge* sensor. This procedure was repeated for every TEM lamella corresponding to a different dpa level. To accompany the high-magnification images, a conventional, bright- and dark-field images were taken, as well as selected area diffraction patterns to provide information about phase and defect analysis.

In addition, the *LightGauge* sensors lamellas were exposed to a parallel beam of high-energy electrons with a wavelength of a few thousandths of a nanometer [167]. Since the spacing between the atoms in a metal is approximately a few tenths of a nanometer [168], the atoms serve as a diffraction grating to the electrons, thus the

electrons are diffracted. In this way, the crystal structure of the specimen can be determined through the scattered electrons in particular angles. This technique resulted in a selected area diffraction pattern (SADP) image that consists of series of dots, each corresponding to a lattice plane of specific Miller indices in a single crystal [169]. The diffraction patterns were very useful in providing crystallographic data about the specimen [170].

All images were analyzed using the Digital Micrograph by Gatan Microscopy Suite software [171] and ImageJ software[24]. The tools were used to determine the grain size of the samples using the particle size analysis as well as to measure the distances between the atomic planes (interplanar spacing or d-spacing) by means of Fast Fourier transform (FFT) algorithm.

Ion and neutron irradiation typically induce grain size growth in metals. The source of this occurrence is described as the rearrangement or recombination of heavily damaged grains into bordering undamaged grains [44]. The reason for grain growth is the damage of a grain in the surrounding area of a grain boundary which gives the grain boundary mobility to expand a neighboring grain [44]. Grain growth also increases when the material is subjected to higher temperatures.

In this study the experiments were performed at low temperatures such that grain growth would not be observed. As such, a reduction in the average grain size was observed. The reduction in the average grain size indicates that at high ion fluences, the evolution of surface morphology is governed by surface diffusion. The irradiation-induced damage instigated in the materials of interest heavily depends on

the separation between the grain boundaries i.e. the size of the grains. The irradiation of the samples was performed by means of low-energy hydrogen ions wherein the maximum damage was deposited very close to the surface (approximately 250 to 350 nm deep) while the average grain size of the unirradiated samples was fairly large (approximately 24 to 34 μm) which makes it possible that all damage was deposited in a single grain away from any grain boundary. This could be interpreted as splitting a single grain into multiple grains by creation of new grain boundaries through ion implantation, hence decreasing the average grain size. The new grain boundaries would most likely come from vacancy defect accumulation which would result in an increase in hydrogen concentration at the grain boundaries and other defects of grains near the surface of the material.

For example, the selected area diffraction patterns, bright-field diffraction contrast and high-resolution TEM images recorded for the zircaloy-4 sample irradiated at 5, 50 and 100 dpa are shown in Figure 6-21 left, middle and right, respectively. The SAD patterns show that, as the dose is increased from 5 to 100 dpa, a more ring like pattern with additional spots and broadening in the patterns occurs, indicative of grain refinement. This outcome is apparent in the bright-field (Figure 6-21, middle) as well as in the high-resolution TEM images (Figure 6-21, right).

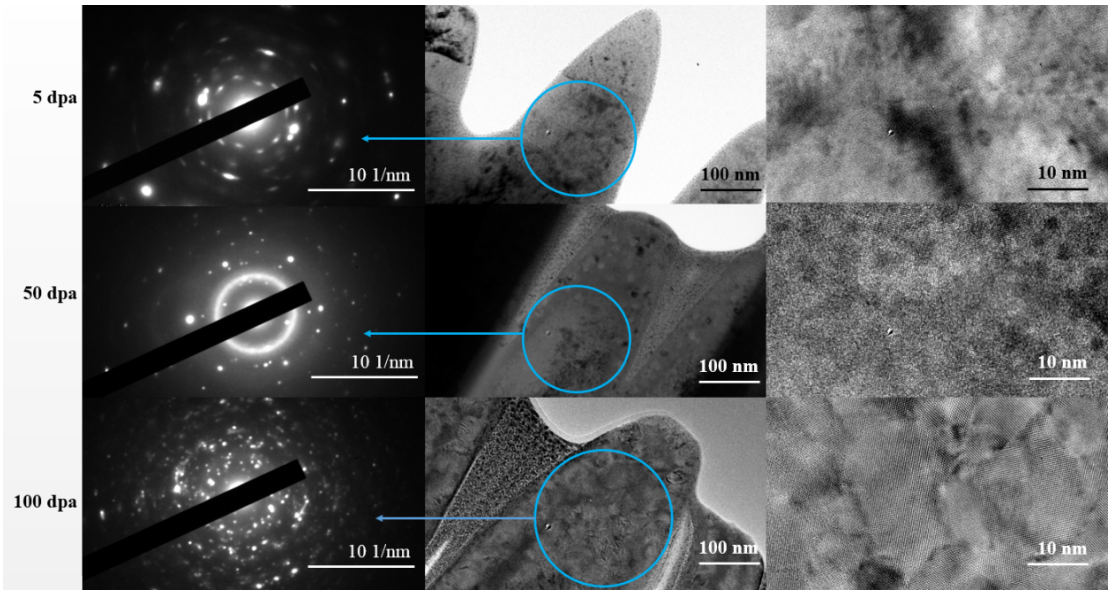

Figure 6-21: TEM micrographs of zircaloy-4 sample at different dpa levels (left) series of SAD pattern, (middle) low-magnification bright-field diffraction contrast TEM micrographs with indication of where the SAD pattern is taken, and (right) high-resolution TEM micrographs.

The average grain size estimation for the steel and zircaloy-4 sample as a function of ion dose (dpa) is illustrated in Figure 6-22 and Figure 6-23, respectively. Figure 6-22 reveals that the average grain size of the steel sample significantly decreases from approximately 24 μm (0 dpa) to 50 nm (100 dpa) over the range of irradiation doses.

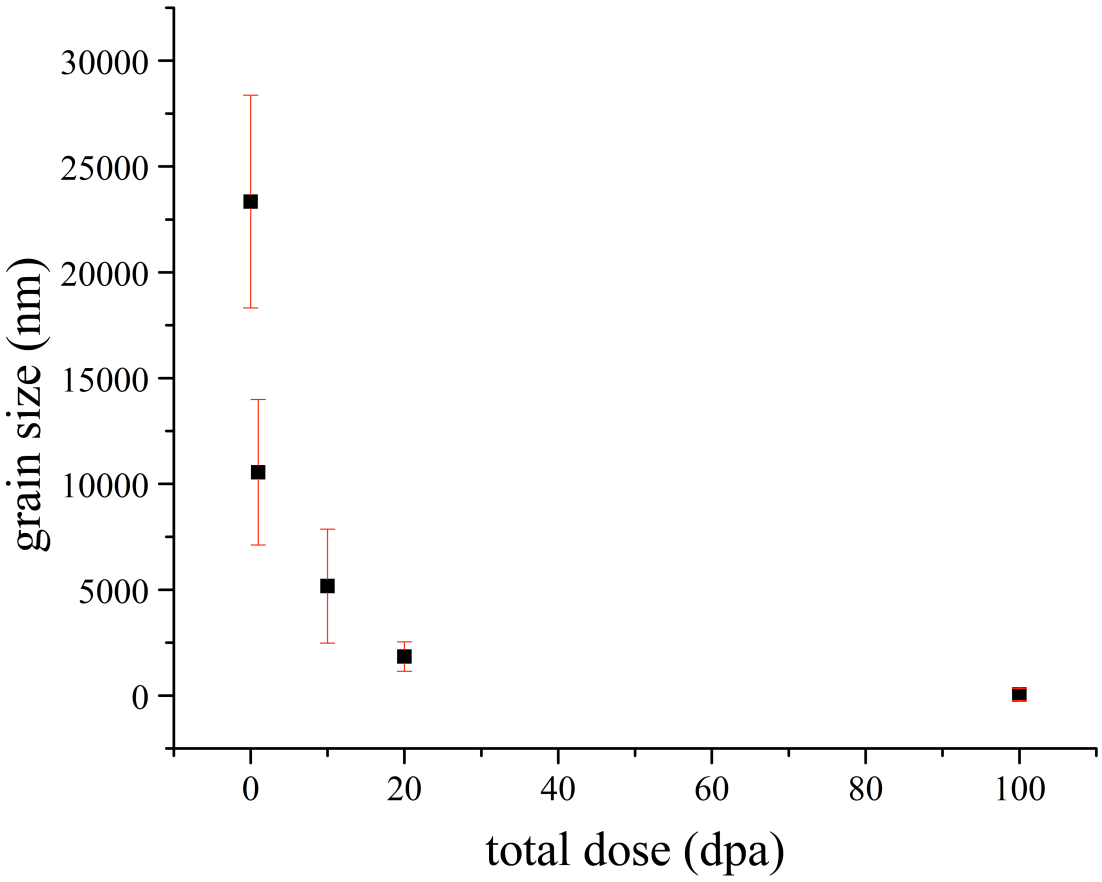

Figure 6-22: Grain size estimation of the steel sample for different irradiation doses. The error bars indicate the standard deviation of uncertainty associated with the grain size measurements.

A similar conclusion is derived for the zircaloy-4 sample, showing a decrease in the average grain size (Figure 6-23) from approximately 34 μm (0 dpa) to 60 nm (100 dpa), considering the same irradiation conditions as the steel sample.

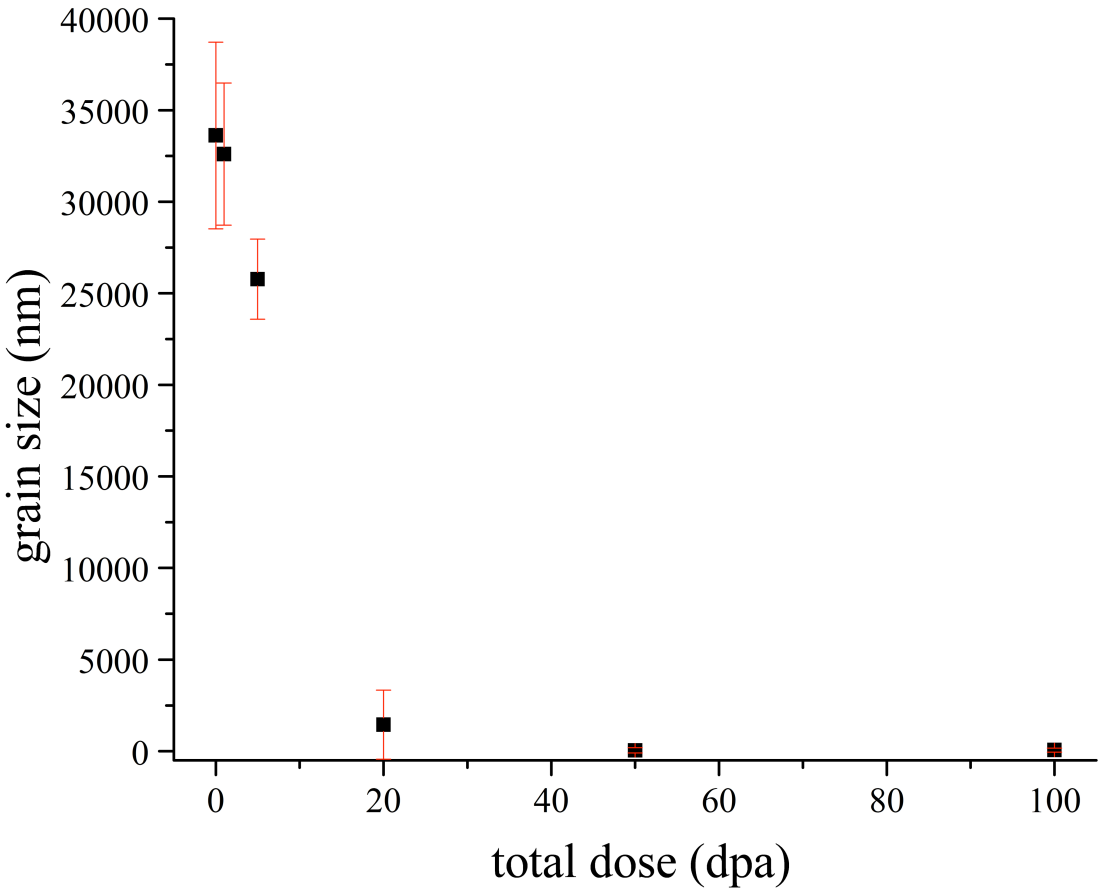

Figure 6-23: Grain size estimation of the zircaloy-4 sample for different irradiation doses. The error bars indicate the standard deviation of uncertainty associated with the grain size measurements.

To support the grain size estimate, the bright- and dark-field TEM images presented in Figure 6-24 and Figure 6-25 show an example of evident grains from which the information included in the graphs was extracted. Figure 6-24 represents four pillars of one *LightGauge* sensor in the steel sample irradiated to the minimum dose, 1 dpa. Figure 6-25 represents two pillars of one *LightGauge* sensor in the zircaloy-4 sample irradiated to the maximum dose, 100 dpa. The bright- and dark-field diffraction images assist in distinguishing the grain boundaries and, therefore,

measure/estimate the grain size. As it can be seen in Figure 6-24, the estimated grain size for the 1 dpa steel sample is certainly larger than approximately 700 nm, hence the grain in the image covers a larger area than revealed in the TEM lamella. On the other hand, the grains in Figure 6-25, representing 100 dpa zircaloy-4 sample, are much smaller which makes it possible for their size to be measured/estimated.

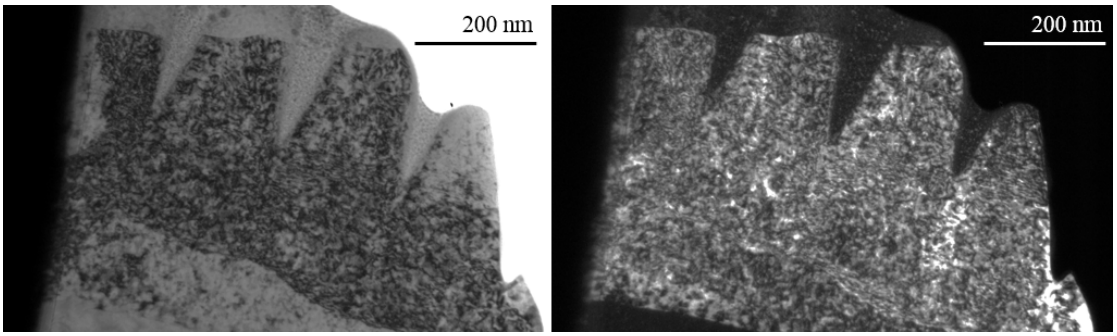

Figure 6-24: TEM micrograph of the steel sample irradiated to 1 dpa (left) bright- and (right) dark-field image.

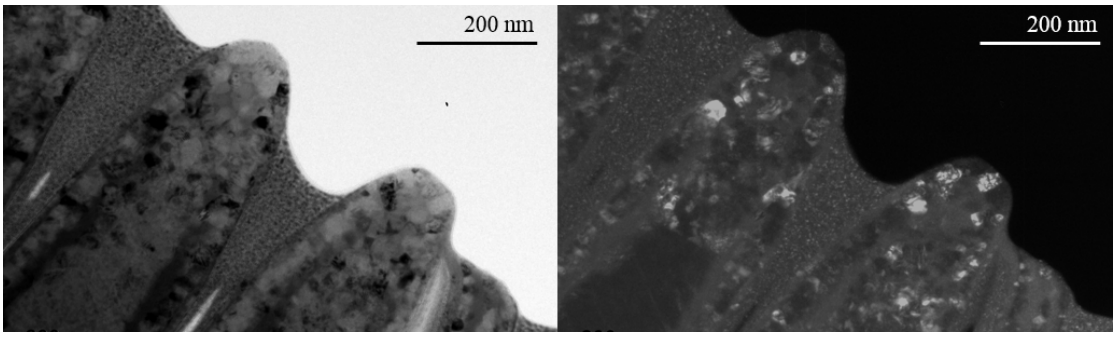

Figure 6-25: TEM micrograph of the zircaloy-4 sample irradiated to 100 dpa (left) bright- and (right) dark-field image.

Similarly to the grain size analysis, irradiation-induced changes of the lattice and crystal structure were investigated using the transmission electron microscope

images. This was performed through measurements of the interplanar spacing (d-spacing)[‡‡‡] for different planes in both materials. According to the damage-depth profiles, presented in Figure 5-19 (Page 96), the most damage in steel and zircaloy-4 occurs approximately around a target depth of 250 nm and 280 nm, respectively. Therefore, the measurements of the d-spacings were performed along the depth of a *LightGauge* sensor's pillar (0 to 350 nm) to observe the occurrence of changes in the lattice.

The d-spacing for a body-centered cubic system, such as steel, can be calculated using the crystal geometry equation below (Equation 6-1).

Equation 6-1

$$\frac{1}{d_{hkl}^2} = \frac{h^2 + k^2 + l^2}{a^2}$$

$$d_{hkl} = \frac{a}{\sqrt{h^2 + k^2 + l^2}}$$

Where:

d_{hkl}	interplanar spacing or d-spacing
a	lattice constant
h, k, l	integers, general notation that illustrates the Miller indices

[‡‡‡] Interplanar spacing or d-spacing is the perpendicular distance between adjacent *hkl* planes in a crystal structure [172].

Since h, k and l are integers that generally illustrate the Miller indices of a specific plane, the resultant d-spacing values are calculated for a given set of unit cell dimensions [173]. The lattice constant defines the physical dimension of a unit cell. For example, the lattice constant, *a*, of iron BCC system is 0.287 nm [68], which can be used as a standard to calculate the d-spacing values for an unirradiated steel sample.

The measured interplanar spacings for (110) plane in the steel sample over two different doses are shown in Figure 6-26. Each value represents the average of three or more separate measurements of the d-spacing and the uncertainty is represented by the standard deviation of the measurements. From Figure 6-26, it is apparent that the measured d-spacing in steel (110) is constant along the depth of a pillar for both (1 and 20 dpa) irradiation doses.

In comparison to the unirradiated d-spacing, 0.2029 nm, irradiation to 1 dpa caused a slight increase of the d-spacing, 0.2034 ± 0.0017 nm. This event may be due to formation of dislocation loops which were hard to determine from the TEM images since the TEM lamellas allowed for investigation of a few pillars only, covering a single grain. They could also be due to the formation of interstitials in the lattice of steel. There was additional increase of the d-spacing to 0.2095 ± 0.0016 nm observed with irradiation to 20 dpa. Irradiation to 20 dpa produces more damaging events, therefore leaving more deformations in the lattice.

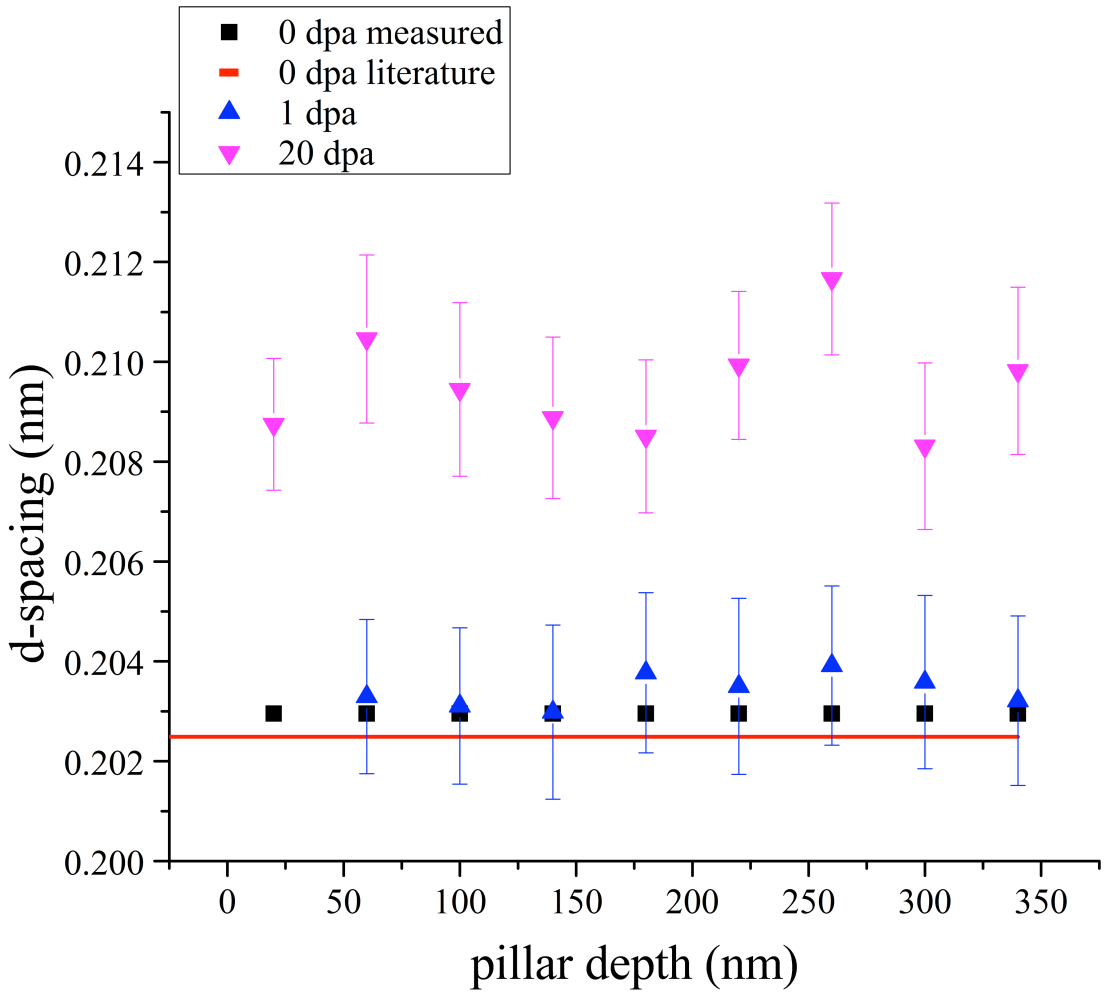

Figure 6-26: Interplanar distance (plane (110)) as a function of depth along the depth of a single pillar steel sample. The error bars indicate the standard deviation of uncertainty associated with the d-spacing measurements.

The averaged measured d-spacing for plane (110) as a function of dpa is presented in Figure 6-27. These results reveal a radiation-induced expansion of the system, associated with 0.5% and 3.5% strain, with 1 dpa and 20 dpa irradiation, respectively.

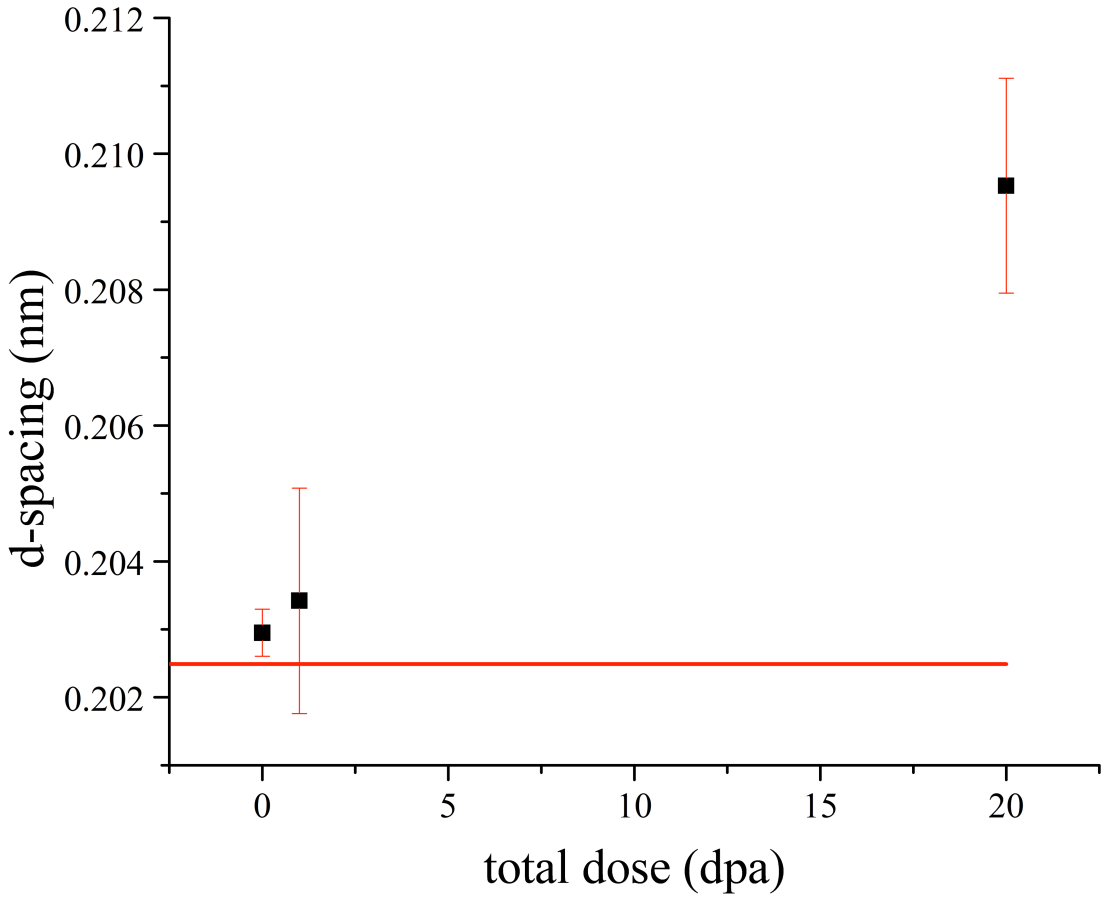

Figure 6-27: Interplanar distance (plane (110)) as a function of dpa for steel sample. The red line represents the literature value for 0 dpa. The error bars indicate the standard deviation of uncertainty associated with the d-spacing measurements.

The d-spacing for a hexagonal close-packed system, such as zircaloy-4, can be calculated using Equation 6-2.

Equation 6-2

$$\frac{1}{d_{hkl}^2} = \frac{4}{3} \times \left(\frac{h^2 + k^2 + l^2}{a^2} \right) + \frac{l^2}{c^2}$$

$$d_{hkl} = \frac{a}{\sqrt{\frac{4}{3}(h^2 + h \times k + k^2) + (l^2 + \frac{a^2}{c^2})}}$$

Where:

d_{hkl}	interplanar spacing or d-spacing
a, c	lattice constants
h, k, l	integers, general notation that illustrates the Miller indices

The lattice constants, *a* and *c*, of zirconium HCP system are 0.323 and 0.515 nm, respectively [174]. These constants were used in Equation 6-2 to determine the standard values for the zircaloy-4 d-spacing (0 dpa). The measured d-spacings, shown in Figure 6-28 and Figure 6-30, roughly agree with the standard values for zircaloy-4 system planes (002) and (102). The plots are representing the average of three or more separate measurements of the d-spacing in the zircaloy-4 sample along the depth of a single pillar over four different irradiation doses.

Figure 6-28 represents the d-spacing measurements for plane (002) for the zircaloy-4 sample. These results indicate an expansion of the system. In comparison

to the unirradiated d-spacing, 0.2574 nm, irradiation to 5 dpa caused an increase of the d-spacing, 0.2631 ± 0.0026 nm. There was additional small increase of the d-spacing to 0.2657 ± 0.0024 nm observed with irradiation to 20 dpa, 0.2728 ± 0.0033 nm observed with irradiation to 50 dpa and 0.2810 ± 0.0025 nm observed with irradiation to 100 dpa.

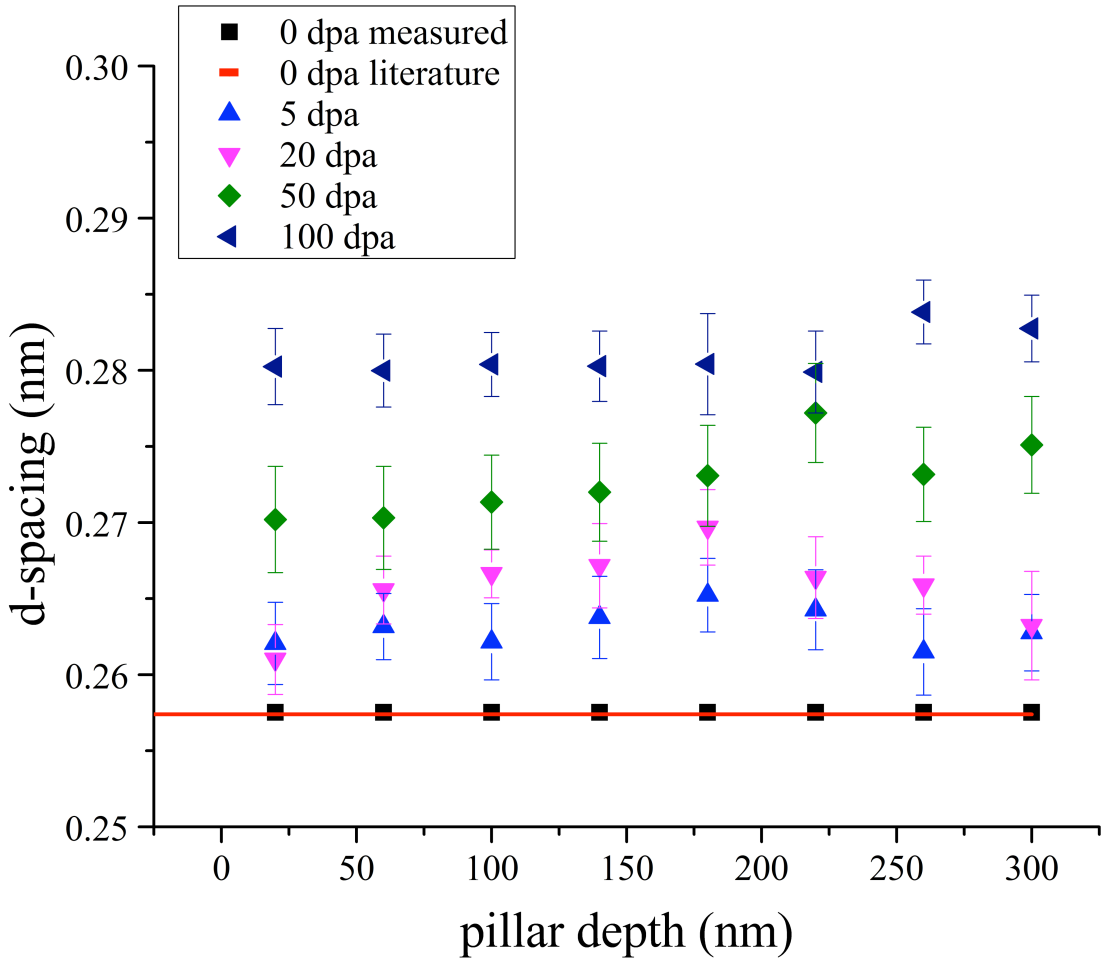

Figure 6-28: Interplanar distance (plane (002)) as a function of depth along the depth of a single pillar zircaloy-4 sample. The error bars indicate the standard deviation of uncertainty associated with the d-spacing measurements.

The averaged measured d-spacing for plane (002) as a function of dpa for zircaloy-4 is presented in Figure 6-29. The comparison of the d-spacing between the unirradiated sample and irradiated sample to 5, 20, 50 and 100 dpa reveals an increase of the interplanar distance associated with a 2%, 3%, 6% and 9% strain, correspondingly.

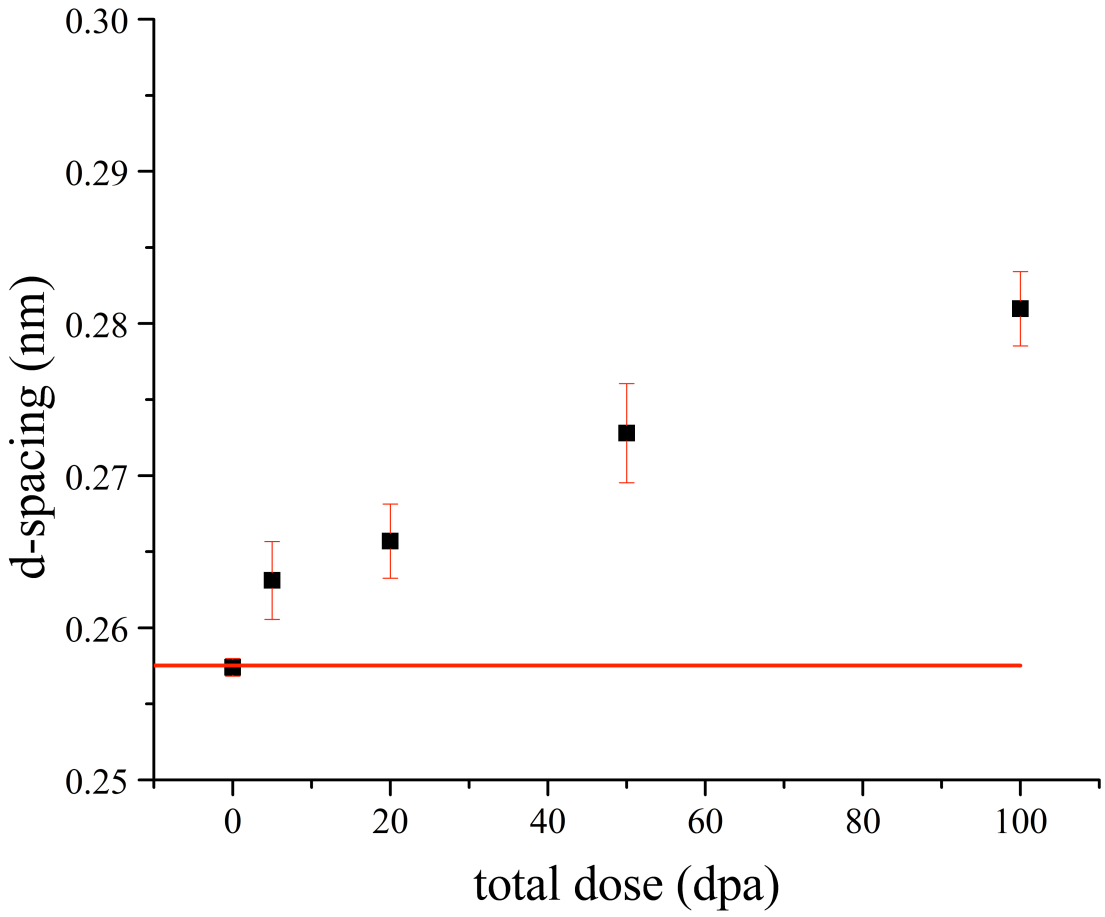

Figure 6-29: Interplanar distance (plane (002)) as a function of dpa for zircaloy-4 sample. The red line represents the literature value for 0 dpa. The error bars indicate the standard deviation of uncertainty associated with the d-spacing measurements.

Figure 6-30 represents the d-spacing measurements for plane (102) in the zircaloy-4 sample. The comparison of the d-spacing between the unirradiated sample and irradiated sample reveals an increase of the interplanar distance throughout every irradiation level. Again, similarly to all other analyzed planes, these results indicate an expansion of the system. In comparison to the unirradiated d-spacing, 0.1894 nm, irradiation to 5 dpa caused an increase of the d-spacing, 0.1920 ± 0.0029 nm. There was additional small increase of the d-spacing to 0.1924 ± 0.0027 nm observed with irradiation to 20 dpa, 0.1967 ± 0.0027 nm observed with irradiation to 50 dpa and 0.1973 ± 0.0029 nm observed with irradiation to 100 dpa.

Another interesting detail occurs in the (102) plane of the zircaloy-4 sample, there is a change in the measured d-spacing along the depth of a pillar. The change is related to an increase of approximately 2% strain in the d-spacing along the depth of the pillar. This reveals additional radiation-induced expansion of the system, which should be expected once correlated with the damage depth profile and the Bragg peak described in Chapter 5.

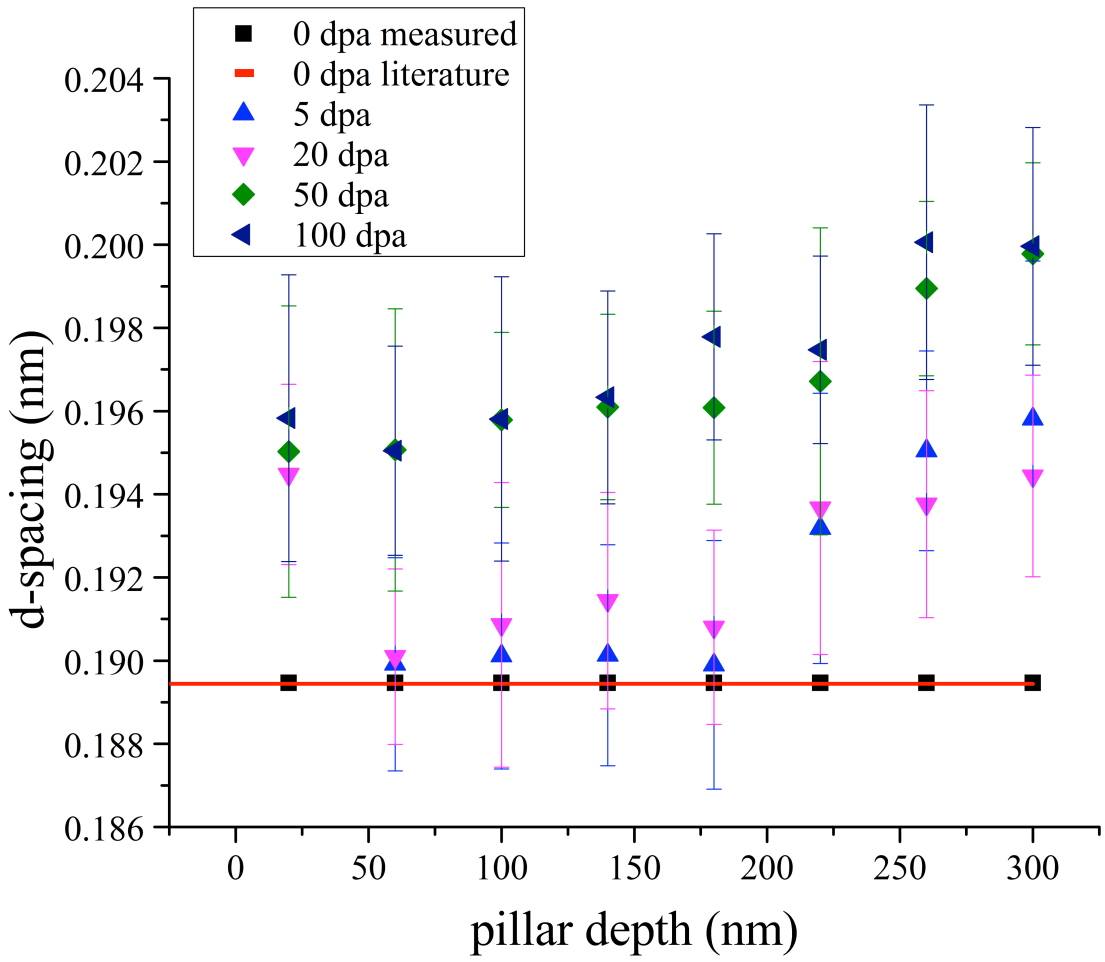

Figure 6-30: Interplanar distance (plane (102)) as a function of depth along the depth of a single pillar zircaloy-4 sample. The error bars indicate the standard deviation of uncertainty associated with the d-spacing measurements.

The averaged measured d-spacing for plane (102) as a function of dpa for zircaloy-4 is presented in Figure 6-31. The comparison of the d-spacing between the unirradiated sample and irradiated sample to 5, 20, 50 and 100 dpa reveals an increase of the interplanar distance associated with a 1%, 1.5%, 3% and 4% strain, correspondingly.

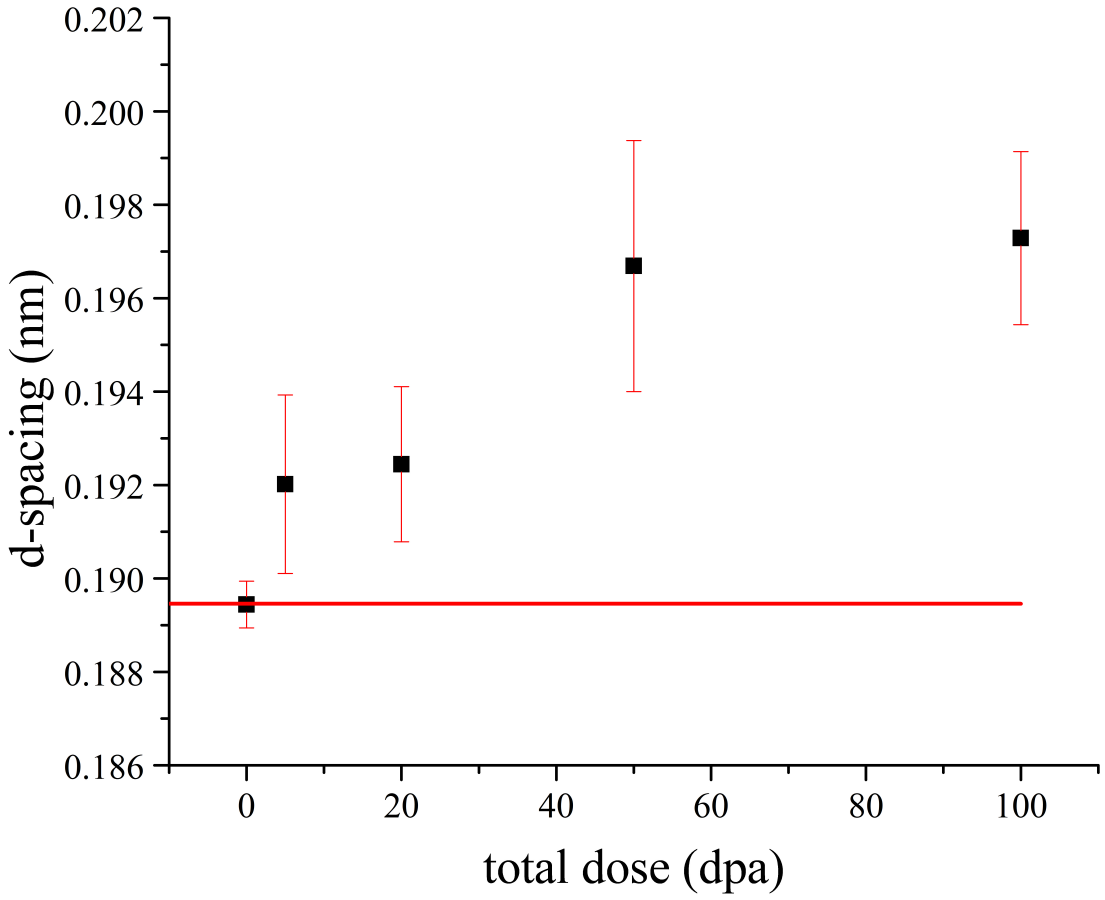

Figure 6-31: Interplanar distance (plane (002)) as a function of dpa for zircaloy-4 sample. The red line represents the literature value for 0 dpa. The error bars indicate the standard deviation of uncertainty associated with the d-spacing measurements.

7 Conclusions and Future Work

7.1 Conclusions

A novel nanostructured sensor, *LightGauge* sensor, based on photonic crystal design was nanomachined onto nuclear fuel cladding materials, specifically steel- and zirconium-alloys, tested using a charged particle accelerator and characterized via ion and electron beam microscopy. The results of the presented experiments provide valuable understanding of the ion-induced damage mechanism of the *LightGauge* sensors and its potential for use in the in-pile sensor technology. These results, and all future work on this project, will contribute to the development and optimization of a deployable in-pile sensor to replace the old fashioned "cook and look" method.

From the grain size and interplanar distance measurements obtained from the TEM imaging, radiation damage of the microstructure was confirmed. Also, it is possible to draw a number of conclusions regarding changes of the structure on atomic level. However, the nature of the defects present in the structures were not explicitly approached in the course of this work. The analysis show that the *LightGauge* sensors survive moderate neutron fluence and very high ion beam fluence and resultant extreme radiation damage to the microstructure.

7.2 Future Work

The goal of the *LightGauge* sensors studied in this thesis is for the sensors to be implemented in future nuclear reactors; however the radiation damage was induced by a charged particle accelerator rather than a research reactor, to provide for accelerated testing.

A nuclear reactor environment is described in section 2.2 of chapter 2. It is characterized by a blend of high temperatures, high neutron and gamma fluxes, radiation damage, mechanical stresses and chemical reactions that all cause changes in the microstructure of the fuel and cladding that are very difficult to predict in a systematic fashion. In order to fully evaluate the nuclear reactor environment resistance of the *LightGauge* sensors as an in-core implemented sensor, all of the above mentioned physical characteristics should be addressed. For instance, the work presented in this thesis should be accompanied by a neutron-induced radiation damage of the sensors. Further, temperature effects should be introduced and studied, followed by mechanical stress. Since the *LightGauge* sensors are designed to reflect the light of a single wavelength, every change that occurs in the photonic crystal is associated with a change in the designated wavelength and could be monitored by means of measuring the wavelength output. It is very important to perform preliminary experiments related to one physical characteristic, to understand the nature of the deformation in the sensors. This will help differentiate between the damage mechanisms, once the sensors are subjected to irradiation in a nuclear environment.

7.3 Project Significance

The research presented in this dissertation has the potential to provide a measurement system that can increase the precision of in-core fuel performance measurements with little or no impact on the reactor neutron economy. Since the photonic crystal sensors (*LightGauge* sensors) utilized in this experimental work are directly written (nano-machined) onto nuclear fuel cladding materials (steel- and zirconium-based alloys), they are capable of continuous operation throughout the entire reactor operating cycle.

The experimental results presented in this thesis show that the novel sensors can withstand a reactor radiation environment. Future work involving a completed monitoring system that includes optical equipment could provide real-time measurements of thermal and mechanical deformation to nuclear fuel cladding materials. This will eliminate the requirement of sample removal for analysis ("cook and look" method) as well as the use of electronics in high radiation fields.

8 Bibliography

[1] V. P. Kryuchkov, A. M. Voloshchenko, Y. V. Konobeev, and others, "About the use of units displacement per atom and fluence for definition of the damage exposure in reactor materials," in *Proceedings of the International Conference on the New Frontiers of Nuclear Technology: Reactor Physics, Safety and High-Performance Computing*, 2002, pp. 7–10.

[2] R.S. Averback and T. Diaz de la Rubia, "Displacement Damage in Irradiated Metals and Semiconductors." .

[3] OECD/NEA, "Primary Radiation Damage in Materials," NEA/NSC/DOC(2015)9.

[4] E10 Committee, "Practice for Neutron Radiation Damage Simulation by Charged-Particle Irradiation," ASTM International, 2009.

[5] IAEA, "Technical and economic limits to fuel burnup extension." Jul-2002.

[6] J. L. Rempe, D. L. Knudson, J. E. Daw, T. C. Unruh, B. M. Chase, K. L. Davis, A. J. Palmer, and R. S. Schley, "Advanced in-pile instrumentation for material and test reactors," in *Advancements in Nuclear Instrumentation Measurement Methods and their Applications (ANIMMA), 2013 3rd International Conference on*, 2013, pp. 1–11.

[7] J. Rempe, H. MacLean, R. Schley, D. Hurley, J. Daw, S. Taylor, J. Smith, J. Svoboda, D. Kotter, D. Knudson, and others, "New In-Pile Instrumentation to Support Fuel Cycle Research and Development," *Ida. Natl. Lab. Fuel Cycle Res. Dev. Adv. Fuels Campaign INLEXT-10-19149 FCRD-FUEL-2011-000033*, 2011.

[8] Joy L. Rempe, Darrell L. Knudson, Joshua E. Daw, Troy Unruh, Benjamin M. Chase, Joe Palmer, Keith G. Condie, and Kurt L. Davis, "Enhanced In-pile Instrumentation at the Advanced Test Reactor," *IEEE*, 2011.

[9] Dotson, Archuleta, Lee, Grider, and Redondo, "Los Alamos National Laboratory Associate Directorate for Theory, Simulation, and Computation." LA-UR 13-20839, 2013.

[10] IAEA, "Fuel behaviour and modelling under severe transient and loss of coolant accident (LOCA) conditions." 2013.

[11] J. R. Lamarsh and A. J. Baratta, *Introduction to Nuclear Engineering*. Prentice Hall, 2001.

[12] B. R. T. Frost, *Nuclear Fuel Elements: Design, Fabrication and Performance*. Elsevier, 2013.

[13] J. T. A. Roberts, *Structural Materials in Nuclear Power Systems*. Springer Science & Business Media, 2013.

[14] N. E. Todreas and M. S. Kazimi, *Nuclear Systems Volume I: Thermal Hydraulic Fundamentals, Second Edition*. CRC Press, 2011.

[15] K. L. Murty and I. Charit, *An Introduction to Nuclear Materials: Fundamentals and Applications*. John Wiley & Sons, 2013.

[16] *U Uranium: Behavior of Uranium Fuels in Nuclear Reactors. Reprocessing of Spent Nuclear Fuels*. Springer Science & Business Media, 2013.

[17] *Comprehensive Nuclear Materials: Five volume Set*. Newnes, 2011.

[18] Massoud T. Simnad, "Nuclear Reactor Materials and Fuels." University of California, San Diego.

[19] "Fuel production, integrated expertise from A to Z - AREVA." [Online]. Available: http://www.areva.com/EN/operations-807/fuel-production-integrated-expertise-from-a-to-z.html. [Accessed: 02-Jul-2015].

[20] H. W. R. De and Y. Nivas, "Sintering uranium oxide in the reaction products of hydrogen-carbon dioxide mixtures," US3872022 A, 18-Mar-1975.

[21] "Nuclear Fuel," *Argonne National Laboratory*. [Online]. Available: http://www.ne.anl.gov/pdfs/nuclear/nuclear_fuel_yacout.pdf. [Accessed: 03-Jun-2015].

[22] Dr. Ghatu Subhash, "Development of Innovative High Thermal Conductivity UO2 Ceramic Composites Fuel Pellets with Carbon Nano-Tubes Using Spark Plasma Sintering," Idaho National Laboratory.

[23] D. G. Cacuci, *Handbook of Nuclear Engineering: Vol. 1: Nuclear Engineering Fundamentals; Vol. 2: Reactor Design; Vol. 3: Reactor Analysis; Vol. 4: Reactors of Generations III and IV; Vol. 5: Fuel Cycles, Decommissioning, Waste Disposal and Safeguards*. Springer Science & Business Media, 2010.

[24] "NRC: Glossary -- Cladding." [Online]. Available: http://www.nrc.gov/reading-rm/basic-ref/glossary/cladding.html. [Accessed: 04-Jul-2015].

[25] "AREVA Cladding Tubes." [Online]. Available: http://us.areva.com/mediatheque/liblocal/images/mediatheque%5Cdiaporamas%5Cactivites%5Camont%5Ccombustible%5Cdia-combustible/combustible-72950.jpg. [Accessed: 24-Jun-2015].

[26] “Nuclear power industry explores accident-resistant fuel - Electric Light & Power.” [Online]. Available: http://www.elp.com/articles/2014/06/nuclear-power-industry-explores-accident-resistant-fuel.html. [Accessed: 24-Jun-2015].

[27] E. S. D. Jones, “DOE FUNDAMENTALS HANDBOOK.”

[28] “Neutron Scattering Lengths and cross sections.” [Online]. Available: https://www.ncnr.nist.gov/resources/n-lengths/elements/zr.html. [Accessed: 24-Jun-2015].

[29] M. Billone, Y. Yan, T. Burtseva, R. Daum, and others, “Cladding embrittlement during postulated loss-of-coolant accidents.,” Argonne National Laboratory (ANL), 2008.

[30] M. Pukari and J. Wallenius, “Cladding materials and radiation damage,” *Dep. React. Phys. K. Tek. Hogskolan*, 2010.

[31] International Atomic Energy Agency, *Computational analysis of the behaviour of nuclear fuel under steady state, transient and accident conditions.* Vienna, Austria: International Atomic Energy Agency, 2007.

[32] V.G. Zborovskii, T.N. Aliev, I.A Evdokimov, A.A. Sorokin, and V.V Likhanskii, “Simulation of Fuel Microstructure Changes and Fission Gas Release for Transient Conditions in the Risø3 Experiments Using the RTOP Code.” .

[33] Bala Radhakrishan and Gorti Sarma, “Mesoscale Simulations of Microstructure Evolution in a Temperature Gradient.” Oak Ridge National Laboratory.

[34] Dr. Brian Wirth, “Microstructure and Property Evolution in Advanced Cladding and Duct Materials Under Long-Term and Elevated Temperature Irradiation: Modeling and Experimental Investigation,” U.S. Department of Energy, Final 10-888.

[35] NEA, “Pellet-clad Interaction in Water Reactor Fuels,” presented at the CEA Cadarache/DEN/DEC, 2005.

[36] “NRC: Backgrounder on the Three Mile Island Accident.” [Online]. Available: http://www.nrc.gov/reading-rm/doc-collections/fact-sheets/3mile-isle.html. [Accessed: 04-Jul-2015].

[37] J. Schwantes, C. Orton, and R. Clark, “Analysis of a Nuclear Accident: Fission and Activation Product Release from the Fukushima Daiichi Nuclear Facility as Remote Indicators of Source Identification, Extent of Release, and State of Damaged Spent Nuclear Fuel,” Pacific Northwest National Laboratory (PNNL), Richland, WA (US), Jan. 2012.

[38] "The Westinghouse Pressurized Water Reactor - Nuclear Power Plant." Westinghouse Electric Corporation, Water Reactor Divisions, 1984.

[39] D.R. Olander, "Radiation Damage," in *Fundamental Aspects of Nuclear Reactor Elements*, 1975.

[40] J. Koutský and J. Kocík, *Radiation Damage of Structural Materials*. Elsevier, 2013.

[41] O. K. Chopra and A. S. Rao, "A review of irradiation effects on LWR core internal materials – IASCC susceptibility and crack growth rates of austenitic stainless steels," *J. Nucl. Mater.*, vol. 409, no. 3, pp. 235–256, Feb. 2011.

[42] P. D. Edmondson, Y. Zhang, S. Moll, F. Namavar, and W. J. Weber, "Irradiation effects on microstructure change in nanocrystalline ceria – Phase, lattice stress, grain size and boundaries," *Acta Mater.*, vol. 60, no. 15, pp. 5408–5416, Sep. 2012.

[43] A. Bement, Ed., *Irradiation Effects on Structural Alloys for Nuclear Reactor Applications*. 100 Barr Harbor Drive, PO Box C700, West Conshohocken, PA 19428-2959: ASTM International, 1970.

[44] G. S. Was, *Fundamentals of radiation materials science: metals and alloys*. Berlin ; New York: Springer, 2007.

[45] G. S. Was, J. T. Busby, T. Allen, E. A. Kenik, A. Jensson, S. M. Bruemmer, J. Gan, A. D. Edwards, P. M. Scott, and P. L. Andreson, "Emulation of neutron irradiation effects with protons: validation of principle," *J. Nucl. Mater.*, vol. 300, no. 2, pp. 198–216, 2002.

[46] C. J. Baroch, *Properties of Reactor Structural Alloys After Neutron Or Particle Irradiation*. ASTM International, 1975.

[47] J. T. Busby and B. D. Hanson, Eds., *Presented at the ASTM 24th Symposium on Effects of Radiation on Nuclear Materials and the Nuclear Fuel Cycle*. 100 Barr Harbor Drive, PO Box C700, West Conshohocken, PA 19428-2959: ASTM International, 2010.

[48] S. A. Maloy, M. R. James, W. R. Johnson, T. S. Byun, K. Farrell, and M. B. Toloczko, "Comparison of fission neutron and proton/spallation neutron irradiation effects on the tensile behavior of type 316 and 304 stainless steel," *J. Nucl. Mater.*, vol. 318, pp. 283–291, May 2003.

[49] T.S. Duh, J.J. Kai, and F.R. Chen, "Effects of grain boundary misorientation on solute segregation in thermally sensitized and proton-irradiated 304 stainless steel," *Elsevier*, 2000.

[50] R.D. Carter, D.L. Damcott, M. Atzmon, G.S. Was, and E.A. Kenik, "Effects of proton irradiation on the microstructure and microchemistry of type 304L stainless steel," *Journal of Nuclear Materials*, 1993.

[51] C. Yan, R. Wang, Y. Wang, X. Wang, and G. Bai, "Effects of ion irradiation on microstructure and properties of zirconium alloys—A review," *Nucl. Eng. Technol.*, vol. 47, no. 3, pp. 323–331, Apr. 2015.

[52] A. Ruzin, G. Casse, M. Glaser, A. Zanet, F. Lemeilleur, and S. Watts, "Comparison of radiation damage in silicon induced by proton and neutron irradiation," *Nucl. Sci. IEEE Trans. On*, vol. 46, no. 5, pp. 1310–1313, 1999.

[53] G. F. Knoll, *Radiation Detection and Measurement*. Wiley, 2000.

[54] S. A. El-Hakim and M. A. Morsy, "Simultaneous γ (Co60)-quanta irradiation and isothermal annealing-induced insulator–metal transition in a-As4Se4Te2 chalcogenide composition," *Radiat. Eff. Defects Solids*, vol. 169, no. 4, pp. 313–324, 2014.

[55] J. Ziegler, J. Biersack, and M. Ziegler, *SRIM - The Stopping and Range of Ions in Matter*. James Ziegler, 2008.

[56] "Types of radiation - Ionizing radiation - Wikipedia, the free encyclopedia." [Online]. Available: https://en.wikipedia.org/wiki/Ionizing_radiation#/media/File:Types_of_radiation.svg. [Accessed: 05-Jul-2015].

[57] J. E. Turner, *Atoms, Radiation and Radiation Protection*. McGraw-Hill, 1991.

[58] H. Bichsel and U. of S. C. D. of Physics, *Passage of charged particles through matter*. Dept. of Physics, University of Southern California, 1969.

[59] T. F. D. Laney and H. M. Kooy, *Proton and Charged Particle Radiotherapy*. Lippincott Williams & Wilkins, 2008.

[60] F. M. Khan, *The Physics of Radiation Therapy*. Lippincott Williams & Wilkins, 2012.

[61] H. Cember and T. Johnson, *Introduction to Health Physics: Fourth Edition*. McGraw Hill Professional, 2008.

[62] R. J. Woods and A. K. Pikaev, *Applied Radiation Chemistry: Radiation Processing*. John Wiley & Sons, 1994.

[63] A. R. Foster and R. L. Wright, *Basic nuclear engineering*. Allyn and Bacon, 1977.

[64] V. V. Balashov, *Interaction of Particles and Radiation with Matter*. Springer Berlin Heidelberg, 2011.

[65] J. J. Duderstadt and L. J. Hamilton, *Nuclear Reactor Analysis*. Wiley, 1976.

[66] C. E. Iliffe, *An Introduction to Nuclear Reactor Theory*. Manchester University Press, 1984.

[67] "Interaction des neutrons avec les atomes | Réactions maîtrisées basées sur la fission." [Online]. Available: http://www.je-comprends-enfin.fr/index.php?/Reactions-maitrisees-basees-sur-la-fission/interaction-des-neutrons-avec-les-atomes/id-menu-65.html. [Accessed: 05-Jul-2015].

[68] W. D. Callister, *(WCS)Materials Science and Engineering: An Introduction, 7th Edition Binder Ready Version*. John Wiley & Sons Canada, Limited, 2007.

[69] D. R. Olander and U. S. E. R. and D. A. D. of R. D. and Demonstration, *Fundamental aspects of nuclear reactor fuel elements: prepared for the Division of Reactor Development and Demonstration, Energy Research and Development Administration*. Technical Information Center, Office of Public Affairs, Energy Research and Development Administration, 1976.

[70] R. A. Johnson and A. N. Orlov, *Physics of Radiation Effects in Crystals*. Elsevier, 2012.

[71] J. Friedel, *Dislocations: International Series of Monographs on Solid State Physics*. Elsevier, 2013.

[72] H.-G. KIM, I.-H. KIM, J.-Y. PARK, and Y.-H. KOO, "INFLUENCE OF ALLOY COMPOSITION ON WORK HARDENING BEHAVIOR OF ZIRCONIUM-BASED ALLOYS," *Nucl. Eng. Technol.*, vol. 45, no. 4, pp. 505–512, Aug. 2013.

[73] J. Weertman and J. R. Weertman, *Elementary dislocation theory*. Macmillan, 1964.

[74] P. J. McNally, "Techniques: 3D imaging of crystal defects," *Nature*, vol. 496, no. 7443, pp. 37–38, Apr. 2013.

[75] Y.-M. Chiang, D. P. Birnie, and W. D. Kingery, *Physical Ceramics: Principles for Ceramic Science and Engineering*. Wiley, 1996.

[76] W. T. R. Jr, *DISLOCATIONS IN CRYSTALS*. 1953.

[77] R. E. Smallman and R. J. Bishop, *Modern Physical Metallurgy and Materials Engineering: Science, Process, Applications*. Butterworth-Heinemann, 1999.

[78] “Edge dislocation in a cubic crystal. : Techniques: 3D imaging of crystal defects : Nature : Nature Publishing Group.” [Online]. Available: http://www.nature.com/nature/journal/v496/n7443/fig_tab/nature12089_F1.html. [Accessed: 06-Jul-2015].

[79] “Surface Defects Grain Boundaries.” [Online]. Available: http://www.engineeringarchives.com/les_matsci_surfacedefects.html. [Accessed: 06-Jul-2015].

[80] IAEA, “Development of Radiation Resistant Reactor Core Structural Materials.” .

[81] L. E. Steele, *Radiation Embrittlement of Nuclear Reactor Pressure Vessel Steels: An International Review*. ASTM International, 1993.

[82] T. R. Mager, W. E. C. N. T. Division, and E. P. R. Institute, *Steady-state radiation embrittlement of reactor vessels*. Electric Power Research Institute, 1985.

[83] K. E. Sickafus, E. A. Kotomin, and B. P. Uberuaga, *Radiation Effects in Solids*. Springer Science & Business Media, 2007.

[84] J. T. Busby, R. K. Nanstad, R. E. Stoller, Z. Feng, and D. J. Naus, “Materials degradation in light water reactors: life after 60,” *ORNL Rep. ORNLTM-2008170*, 2008.

[85] J. A. L. Robertson, A. M. Ross, M. J. F. Notley, and J. R. MacEwan, “Temperature distribution in UO2 fuel elements,” *J. Nucl. Mater.*, vol. 7, no. 3, pp. 225–262, Dec. 1962.

[86] D. Carpenter, “Comparison of Pellet-Cladding Mechanical Interaction for Zircaloy and Silicon Carbide Clad Fuel Rods in Pressurized Water Reactors.”

[87] “Thermal Conductivity of Zirconium.” [Online]. Available: https://upload.wikimedia.org/wikipedia/commons/0/0f/ZrUthermalcond.png. [Accessed: 06-Jul-2015].

[88] Y.-H. Koo, B.-H. Lee, J.-Y. Oh, and K.-W. Song, “Conservative Width of High-Burnup Structure in Light Water Reactor UO 2 Fuel as a Function of Pellet Average Burnup,” *Nucl. Technol.*, vol. 164, no. 3, pp. 337–347, 2008.

[89] K. Yanagisawa, “Fuel densification and swelling: Relationship between burn-up induced axial and radial fuel dimensional changes,” *Nucl. Eng. Des.*, vol. 96, no. 1, pp. 11–20, Sep. 1986.

[90] Nuclear Energy Agency (NEA), “Nuclear Fuel Behaviour in Loss-of-coolant Accident (LOCA) Conditions,” OECD, 6846, 2009.

[91] L. A. Walton and D. L. Husser, “Fuel pellet fracture and relocation,” in *Proc. IAEA Specialist’s Meeting on Water Reactor Fuel Element Performance Computer Modelling. Applied Science, Preston, UK*, 1983, pp. 115–135.

[92] International Atomic Energy Agency, Ed., *Fuel failure in water reactors: causes and mitigation : proceedings of a Technical Committee meeting held in Bratislava, Slovakia, 17-21June 2002*. Vienna, Austria: International Atomic Energy Agency, 2003.

[93] G. B. Carpenter, *Principles of crystal structure determination*. W. A. Benjamin, 1969.

[94] John D. Joannopoulos, Steven G. Johnson, Joshua N. Winn, and Robert D. Meade, *Photonic Crystals: Molding the Flow of Light*, 2nd edition. Princeton University Press, 2008.

[95] C. M. Soukoulis, *Photonic Band Gap Materials*. Springer Science & Business Media, 2012.

[96] E. Yablonovitch, T. J. Gmitter, and K. M. Leung, “Photonic band structure: The face-centered-cubic case employing nonspherical atoms,” *Phys. Rev. Lett.*, vol. 67, no. 17, pp. 2295–2298, Oct. 1991.

[97] S. John, “Strong localization of photons in certain disordered dielectric superlattices,” *Phys. Rev. Lett.*, vol. 58, no. 23, p. 2486, 1987.

[98] K. Dholakia and T. Čižmár, “Shaping the future of manipulation,” *Nat. Photonics*, vol. 5, no. 6, pp. 335–342, Jun. 2011.

[99] K. Hirose, Y. Liang, Y. Kurosaka, A. Watanabe, T. Sugiyama, and S. Noda, “Watt-class high-power, high-beam-quality photonic-crystal lasers,” *Nat. Photonics*, vol. 8, no. 5, pp. 406–411, May 2014.

[100] X. Ren, L. Feng, Z. Lin, Z. Zhou, and X. Deng, “Analysis of optical coupling between air-holes photonic crystal and tapered dielectric waveguides,” *Opt. - Int. J. Light Electron Opt.*, vol. 124, no. 24, pp. 6606–6610, Dec. 2013.

[101] K. Nozaki, S. Matsuo, K. Takeda, T. Sato, E. Kuramochi, and M. Notomi, “InGaAs nano-photodetectors based on photonic crystal waveguide including ultracompact buried heterostructure,” *Opt. Express*, vol. 21, no. 16, pp. 19022–19028, Aug. 2013.

[102] H. Li, J. Wu, and Z. M. Wang, *Silicon-based Nanomaterials*. Springer Science & Business Media, 2013.

[103] W. R. Frei, *Optimization of Photonic Crystal Structures*. ProQuest, 2007.

[104] S. Kinoshita and S. Yoshioka, “Structural Colors in Nature: The Role of Regularity and Irregularity in the Structure,” *ChemPhysChem*, vol. 6, no. 8, pp. 1442–1459, Aug. 2005.

[105] J. Sun, B. Bhushan, and J. Tong, “Structural coloration in nature,” *RSC Adv.*, vol. 3, no. 35, p. 14862, 2013.

[106] “Butterflies | Causes of Color.” [Online]. Available: http://www.webexhibits.org/causesofcolor/15A.html. [Accessed: 07-Jul-2015].

[107] P. Ragesh, V. Anand Ganesh, S. V. Nair, and A. S. Nair, “A review on ‘self-cleaning and multifunctional materials,’” *J. Mater. Chem. A*, vol. 2, no. 36, p. 14773, Jun. 2014.

[108] J. Zi, X. Yu, Y. Li, X. Hu, C. Xu, X. Wang, X. Liu, and R. Fu, “Coloration strategies in peacock feathers,” *Proc. Natl. Acad. Sci.*, vol. 100, no. 22, pp. 12576–12578, 2003.

[109] “Image of an Opal gemstone.” [Online]. Available: http://www.swissgemshop.ch/contents/media/l_white-opal-2201a.jpg. [Accessed: 07-Jul-2015].

[110] D. J. Norris, E. G. Arlinghaus, L. Meng, R. Heiny, and L. E. Scriven, “Opaline photonic crystals: how does self-assembly work?,” *Adv. Mater.*, vol. 16, no. 16, pp. 1393–1399, 2004.

[111] N. Karasawa and K. Tada, “PHOTONIC CRYSTALS–,” 2012.

[112] E. Hecht and A. Zajac, *Optics*. Addison-Wesley, 1987.

[113] L. R. S. R.S, “XXVI. On the remarkable phenomenon of crystalline reflexion described by Prof. Stokes,” *Philos. Mag. Ser. 5*, vol. 26, no. 160, pp. 256–265, Sep. 1888.

[114] A. M. R. Pinto and M. Lopez-Amo, “Photonic Crystal Fibers for Sensing Applications,” *J. Sens.*, vol. 2012, pp. 1–21, 2012.

[115] S. John, “Localization of light,” *Phys Today*, vol. 44, no. 5, pp. 32–40, 1991.

[116] S.-H. Chung and J.-Y. Yang, “Optical properties of three-dimensional woodpile photonic crystals composed of circular cylinders with planar defect structures,” *Appl. Opt.*, vol. 50, no. 36, pp. 6657–6666, 2011.

[117] K. O. Hill and G. Meltz, “Fiber Bragg grating technology fundamentals and overview,” *J. Light. Technol.*, vol. 15, no. 8, pp. 1263–1276, Aug. 1997.

[118] S. J. Mihailov, “Fiber Bragg Grating Sensors for Harsh Environments,” *Sensors*, vol. 12, no. 2, pp. 1898–1918, Feb. 2012.

[119] M. D. Todd, J. M. Nichols, S. T. Trickey, M. Seaver, C. J. Nichols, and L. N. Virgin, "Bragg grating-based fibre optic sensors in structural health monitoring," *Philos. Trans. R. Soc. Lond. Math. Phys. Eng. Sci.*, vol. 365, no. 1851, pp. 317–343, Feb. 2007.

[120] N. Tsoulfanidis, *Nuclear Energy: Selected Entries from the Encyclopedia of Sustainability Science and Technology*. Springer Science & Business Media, 2012.

[121] J. A. Lane, "SYMPOSIUM ON ZIRCONIUM COSTS, SPONSORED BY THE COLUMBIA NATIONAL CORPORATION FEBRUARY 13, 1958," Oak Ridge National Lab., Tenn., 1958.

[122] P. G. Shewmon, "Radiation-induced swelling of stainless steel," *Science*, vol. 173, no. 4001, pp. 987–991, Sep. 1971.

[123] R. Viswanathan, *Damage Mechanisms and Life Assessment of High Temperature Components*. ASM International, 1989.

[124] J. M. Gray, *Processing and Properties of Low Carbon Steel*. Metallurgical Society of AIME, 1973.

[125] "Carbon Steel Table." [Online]. Available: http://www.learneasy.info/MDME/MEMmods/MEM30007A/steel/steel_files/carbonsteeltable.jpg. [Accessed: 10-Jul-2015].

[126] "AISI 1018 MIld/Low Carbon Steel," *AZO Materials*. [Online]. Available: http://www.azom.com/article.aspx?ArticleID=6115. [Accessed: 16-Jun-2015].

[127] "ASTM A36 Mild/Low Carbon Steel," *AZO Materials*. [Online]. Available: http://www.azom.com/article.aspx?ArticleID=6117. [Accessed: 16-Jun-2015].

[128] "Iron-carbon Phase Diagram." [Online]. Available: http://i.stack.imgur.com/gn8MR.png. [Accessed: 10-Jul-2015].

[129] "12.2: The Arrangement of Atoms in Crystalline Solids - Chemwiki." [Online]. Available: http://chemwiki.ucdavis.edu/Wikitexts/UC_Davis/UCD_Chem_2B/UCD_Chem_2B%3A_Larsen/Unit_II%3A_States_of_Matter/Solids/12.2%3A_The_Arrangement_of_Atoms_in_Crystalline_Solids. [Accessed: 10-Jul-2015].

[130] W. Hoffelner, *Materials for Nuclear Plants*. London: Springer London, 2013.

[131] A. V. Flores, A. G. Gomez, and G. A. Juarez, "Typical zirconium alloys microstructures in nuclear components," 2014.

[132] Stevens, "The structure of solids, chapter S." .

[133] C. M. Eucken, *Zirconium in the Nuclear Industry: Ninth International Symposium*. ASTM International, 1991.

[134] "Zircaloy-4(Alloy Zr4) (UNS R60804)," *AZO Materials*. [Online]. Available: http://www.azom.com/article.aspx?ArticleID=7644. [Accessed: 16-Jun-2015].

[135] S. G. Johnson and A. I. P. Group, "MIT Photonic Bands," *MIT*. [Online]. Available: http://ab-initio.mit.edu/wiki/index.php/MIT_Photonic_Bands. [Accessed: 02-Jun-2015].

[136] John Joannopoulos, "The Joannopoulos Research Group at MIT," *MIT*. [Online]. Available: http://ab-initio.mit.edu/. [Accessed: 02-Jun-2015].

[137] NEC, "Pelletron Systems," *NEC National Electrostatic Corp., The World Leader in Megavolt Accelerator Technology*, 2015. [Online]. Available: http://www.pelletron.com.

[138] "Kurt J. Lesker Company | Wobble Stick - Linear & Rotary Motion with Gripper or Pincer Options | Vacuum Science Is Our Business." [Online]. Available: https://www.lesker.com/newweb/sample_manipulation/sample_transfer/wobble_sticks/pincer.cfm. [Accessed: 14-Jul-2015].

[139] J. Ziegler, "SRIM Software." [Online]. Available: http://www.srim.org. [Accessed: 14-Oct-2014].

[140] M. I. Bratchenko, V. V. Bryk, S. V. Dyuldya, A. S. Kalchenko, N. P. Lazarev, and V. N. Voyevodin, "Comments on DPA calculation methods for ion beam driven simulation irradiations," *VANT Rep. Ser.*, no. 2, p. 84, 2013.

[141] M. J. Norgett, M. T. Robinson, and I. M. Torrens, "A proposed method of calculating displacement dose rates," *Nucl. Eng. Des.*, vol. 33, no. 1, pp. 50–54, Aug. 1975.

[142] G. H. Kinchin and R. S. Pease, "The Displacement of Atoms in Solids by Radiation," *Rep. Prog. Phys.*, vol. 18, no. 1, p. 1, Jan. 1955.

[143] J. Avison, *The World of Physics*. Nelson Thornes, 2014.

[144] University of Maryland, College Park, MD, "UMCP, Safety Analysis Report." 2000.

[145] M. Herman, A. L. Nichols, and International Atomic Energy Agency, Eds., *Update of X ray and gamma ray decay data standards for detector calibration and other applications*. Vienna, Austria: International Atomic Energy Agency, 2007.

[146] International Bureau of Weights and Measures and International Organization for Standardization, Eds., *Guide to the expression of uncertainty in measurement*, 1st ed. 1993. Genève, Switzerland: International Organization for Standardization, 1993.

[147] "U.S.NRC Glossary: Neutron Flux," *United States Nuclear Regulatory Commission*, 20-Mar-2015. [Online]. Available: http://www.nrc.gov/reading-rm/basic-ref/glossary/neutron-flux.html.

[148] R. M. Langford, "Focused ion beams techniques for nanomaterials characterization," *Microsc. Res. Tech.*, vol. 69, no. 7, pp. 538–549, Jul. 2006.

[149] "Introduction: Focused Ion Beam Systems," *Fibics Inc.* [Online]. Available: http://www.fibics.com/fib/tutorials/introduction-focused-ion-beam-systems/4/. [Accessed: 19-May-2015].

[150] C. A. Volkert and A. M. Minor, "Focused ion beam microscopy and micromachining," *MRS Bull.*, vol. 32, no. 05, pp. 389–399, 2007.

[151] M. Feldman, *Nanolithography: The Art of Fabricating Nanoelectronic and Nanophotonic Devices and Systems*. Woodhead Publishing, 2014.

[152] P. J. Blau, *Wear of Materials*. Elsevier, 2003.

[153] L. A. Giannuzzi and F. A. Stevie, "A review of focused ion beam milling techniques for TEM specimen preparation," *Micron*, vol. 30, no. 3, pp. 197–204, 1999.

[154] L. A. Giannuzzi and F. A. Stevie, Eds., *Introduction to focused ion beams: instrumentation, theory, techniques, and practice*. New York: Springer, 2005.

[155] M. L. Jenkins and M. A. Kirk, *Characterisation of Radiation Damage by Transmission Electron Microscopy*. CRC Press, 2000.

[156] M. Spencer, *Fundamentals of Light Microscopy*. CUP Archive, 1982.

[157] "White LEDs Printed on Paper—A Doctoral Thesis--Part V | EDN." [Online]. Available: http://www.edn.com/design/led/4396478/2/White-LEDs-Printed-on-Paper-A-Doctoral-Thesis-Part-V. [Accessed: 09-Jul-2015].

[158] "NISP-03: JEM 2100 LaB6 TEM | AIMLab | Maryland NanoCenter." [Online]. Available: https://www.nanocenter.umd.edu/aimlab/equipment/detail.php?id=sc146f00fb44fdae. [Accessed: 02-Sep-2015].

[159] J. Goldstein, *Practical Scanning Electron Microscopy: Electron and Ion Microprobe Analysis*. Springer Science & Business Media, 2012.

[160] “Comparison between a light microscope and a scanning electron microscope.” [Online]. Available: http://www.ammrf.org.au/myscope/images/sem/sem-ve-lm.png. [Accessed: 17-Jun-2015].

[161] P. Heitjans and J. Kärger, *Diffusion in Condensed Matter: Methods, Materials, Models*. Springer Science & Business Media, 2006.

[162] T. Maitland and S. Sitzman, *Electron backscatter diffraction (EBSD) technique and materials characterization examples*, vol. 14. Springer Berlin, 2007.

[163] “EBSD: Electron BackScatter Diffraction,” *Quantenmechanisch geführtes Design neuer Eisenbasis-Werkstoffe*. [Online]. Available: http://abinitio.iehk.rwth-aachen.de/glossar/?text_id=159&division=Array&scale=Array. [Accessed: 28-May-2015].

[164] “EBSD pattern of ferrite steel.” [Online]. Available: https://edaxblog.files.wordpress.com/2014/05/8_ebsd-pattern-ferrite-600c.jpg?w=620. [Accessed: 09-Jul-2015].

[165] C. A. Schneider, W. S. Rasband, and K. W. Eliceiri, “NIH Image to ImageJ: 25 years of image analysis,” *Nat. Methods*, vol. 9, no. 7, pp. 671–675, Jul. 2012.

[166] “AIMLab | NanoCenter.” [Online]. Available: https://www.nanocenter.umd.edu/aimlab/. [Accessed: 26-Oct-2015].

[167] “Basic principle of transmission electron microscope,” *Physics World*, 2015. [Online]. Available: http://www.hk-phy.org/atomic_world/tem/tem02_e.html.

[168] W. Hume-Rothery and G. V. Raynor, *The structure of metals and alloys*. Institute of Metals, 1962.

[169] D. B. Williams and C. B. Carter, *Transmission electron microscopy: a textbook for materials science*, 2nd ed. New York: Springer, 2008.

[170] K.-L. Lin, “Phase Identification Using Series of Selected Area Diffraction Patterns and Energy Dispersive Spectrometry within TEM,” *Microsc. Res.*, vol. 02, no. 04, pp. 57–66, 2014.

[171] “Gatan Microscopy Suite Software | Gatan, Inc.” [Online]. Available: http://www.gatan.com/products/tem-analysis/gatan-microscopy-suite-software. [Accessed: 26-Oct-2015].

[172] J. F. Shackelford, *Introduction to Materials Science for Engineers*. Prentice Hall, 2009.

[173] V. Pecharsky and P. Zavalij, *Fundamentals of Powder Diffraction and Structural Characterization of Materials*. Springer Science & Business Media, 2003.

[174] J. Goldak, L. T. Lloyd, and C. S. Barrett, “Lattice Parameters, Thermal Expansions, and Gr"uneisen Coefficients of Zirconium, 4.2 to 1130\ifmmode^\circ\else\textdegree\fi{}K,” *Phys. Rev.*, vol. 144, no. 2, pp. 478–484, Apr. 1966.